Large Eddy Simulation Of A Controlled Auto-Ignition Engine Using A Multi-dimensional Tabulated Chemistry Approach

Vom Fachbereich Maschinenbau
an der Technischen Universität Darmstadt
zur
Erlangung des Grades eines Doktor-Ingenieurs (Dr.-Ing.)
genehmigte

D i s s e r t a t i o n

vorgelegt von

Dipl.-Ing. Esra Yildar

aus Ankara

Berichterstatter:	Prof. Dr.-Ing. J. Janicka
Mitberichterstatter:	Prof. Dr.-Ing. C. Hasse
Tag der Einreichung:	23. Januar 2017
Tag der mündlichen Prüfung:	15. März 2017

Darmstadt 2017

D17

Preface

This thesis is the result of my time as doctoral candidate at the Institute for Energy and Power Plant Technology (EKT) at the Technical University Darmstadt.

I am very grateful to the head of the institute, Prof. Dr.-Ing. Johannes Janicka for this opportunity and his trust in me.

My appreciation goes to Prof. Dr.-Ing. Christian Hasse the head of the Institute for Numerical Thermo-Fluid Dynamics at the Technical University Freiberg, for his willingness to report on my work.

I appreciate the great atmosphere at EKT due to numerous nice colleagues. However some of them I would like to thank here explicitly. Firstly, my very special thanks go to Dr.-Ing. Guido Kuenne. There are not enough words to describe my gratitude to him. He has been a great supervisor and a friend to me. This work would not be existing in its current form without his supervision and help. I have learned lots of things related to my work from his incredibly immense theoretical and practical background. More important than that, he has showed to me and surely to many other colleagues how a real scientist should be: Honest, clever, hard working and grounded. I am a very lucky person that I had the opportunity to work with such a valuable scientist. Secondly, I would like to thank my dear friend Dr.-Ing. Thorsten Meier for his endless support during my time in EKT. Sharing the same office four years with him was inestimable. Further I would like to thank Dr.-Ing. Chao He, for the enjoyable teamwork and for being such a good friend to me. My gratitude goes to M.Sc. Robert Knappstein who is an extremely talented and successful engineer, for his help and support during my time at EKT and most importantly for his friendship. Finally, I want to thank another very important person to me from EKT, M.Sc. Florian Rieß. Beside his precious friendship, he is an incredibly inspiring engineer from whom I have learned too much.

I would like to thank Dr.-Ing. Robert Schießl and Dr.-Ing. Marc-Sebastian Benzinger, both from the Institute of Technical Thermodynamics (ITT), Karlsruhe Institute of Technology for the cooperation work during my thesis. Especially, I would like to thank Dr. -Ing. Robert Schießl for the very valuable discussions which helped me to carry my thesis forward.

My main gratitude goes to my family Selma Yildar, Yavuz Yildar, Merve Yildar Basyigit, Cahit Yalcin and Asli Yalcin for their endless love and support.

Esra Yildar Darmstadt, 23. January 2017

Hiermit erkläre ich an Eides statt, dass ich die vorliegende Dissertation selbstständig verfasst und keine anderen als die von mir angegebenen Hilfsmittel verwendet habe. Ich erkläre außerdem, dass ich bisher noch keinen Promotionsversuch unternommen habe.

Esra Yildar

Darmstadt, den 23. Januar 2017

To my dear nephew Demir Arslan Basyigit ...

Contents

Chapter 1

Introduction

1.1 Motivation

More than 80% of the world's primary energy consumption is based on combustion of fossil fuels like oil, gas and coal [46]. The renewable energy on the other hand covers only almost 10% of the primary energy consumption [46, 17]. In their yearly issued report the International Energy Agency states the global primary energy demand to increase by 53% and fossil fuels will remain the main energy source for a long time [47]. Furthermore the IEA estimates a rise in consumption of energy of about 60% until 2030 in comparison to 2002 [47]. According to the reports published by BP [17] most of the fossil fuel resources are located in the middle east. Considering the world population rises from 7.3 billion in 2015 to 9.2 billion in 2040, with India overtaking China in the early 2020s as the most populous country [46], these limitedness of the resources will further lead to political conflicts and a shortening on the global markets.

On the other hand from the combustion of fossil fuels obtained reaction products have negative impacts on human health and environment. With regard to the well-known green-house effect, in 1992, in Rio de Janeiro the United Nations Framework Convention on Climate Change (UNFCCC or FCCC) negotiated the subject: "stabilize greenhouse gas concentrations in the atmosphere at a level that would prevent dangerous anthropogenic interference with the climate system" [2]. This negotiation was adopted on 11 December 1997 in Kyoto, Japan, and entered into force on 16 February 2005 and called "Kyoto Protocol". Accordingly, 37 industrialized countries [2] and the European Community [3] commit themselves to limit or reduce their emissions of four greenhouse gases being: Carbon dioxide (CO_2), Methane (CH_4), Nitrous oxide (N_2O), Sulphur hexafluoride (SF_6).

European union limited in 1984 emission formations with the regulations called: Euro-emissions standards. These limitations depends on the vehicle category (e.g., passenger car, truck, bus etc.), the fuel type (i.e., gasoline- or diesel engine) and mixture preparation (i.e., premixed or direct injection). The Euro limitations are updated each 4-5 years and become stricter. As an example, in Table 1.1 the last three emission limits being Euro 4, Euro 5 and Euro 6 for passenger cars with conventional diesel- and gasoline engines are presented. From the table one can see that for diesel engines the allowed emission rates of oxides of nitrogen NO_x and combination of hydrocarbons (THC + NO_x) were decreased by 68% and 170% from Euro 4 to Euro 6 respectively. The upcoming Euro 7 will be even

stricter. The experts are expecting that for heavy-duty diesel engines Euro 7 will not only reduce CO_2 emission but also a further reduction of NO_x, almost half of Euro 6 [114].

Table 1.1: Euro 4, 5, 6 emission limits for passenger cars both with diesel- and gasoline (petrol) engines [1]. *If the fuel is injected directly.

Euro Regulations	Euro 4		Euro 5		Euro 6	
Date	January 2005		September 2009		September 2014	
Limited components (mg/km)	Gasoline	Diesel	Gasoline	Diesel	Gasoline	Diesel
Carbon monoxide (CO)	1000	500	1000	500	1000	500
Total hydrocarbons (THC)	100	-	100	-	100	-
Non-methane hydrocarbons MTHC	-	-	68	-	68	-
Oxides of nitrogen (NO_x)	80	250	60	180	60	80
Combination of hydrocarbons (THC + NO_x)	-	300	-	230	-	170
Particulate matter PM	-	2.5	5.0*	5.0	5.0*	5.0

Considering these strict limitations of pollutant emissions and limited fossil fuel resources the demand for fuel-efficient and environment friendly Internal Combustion Engines (ICE) increases. Here at this point the Homogeneous Charge Compression Ignition (HCCI) engine is a promising technology as it combines advantages of both, the diesel- and spark ignition engine [26, 126, 35, 23]. In HCCI engines NO_x formation is prevented since they operate with highly diluted charges, leading to low flame temperatures [7, 23, 26, 126, 35]. Furthermore, since the charge is well-mixed, soot formation is avoided [7, 26]. On the other hand, due to their high compression ratios, the efficiencies of HCCI engines are comparable with conventional diesel compression ignition (CI) engines [23, 26, 126, 35]. However, since in high-load HCCI engines, high pressure peak and high heat release occur, resulting in engine knock, HCCI technology is applied for a limited range of loads [26, 13]. In order to extend the operating range of HCCI engines, Controlled Auto Ignition (CAI) concept is developed [35, 126]. The CAI concept involves several strategies mainly aim to alter mixture reactivity or increase ignition delay [13]. Several controlling strategies exist in order to control HCCI combustion. For instance, a CAI engine configuration is so-called Partially premixed combustion (PCC), also known as PCCI, engine couples both strategies Exhaust Gas Recirculation (EGR) and early fuel injection [90]. In general PCCI engines operates with high amounts of EGR and fuel is injected sufficiently early so that injection timing and ignition start is separated from each other [66]. The EGR is either achieved by trapping hot exhaust gas in-cylinder with the Negative Valve Overlap (NVO) concept or burnt gas load during intake, so called Burnt Gas Re-Breathing (BGRB)[126, 23]. Using direct injection technique, higher controllability of the combustion is achieved [62, 73] and the EGR employment dilutes the fresh air−fuel mixture thereby decreasing the peak pressure and delaying auto-ignition [31, 35, 49].

For further systematic optimization, these concepts demand a profound understanding of the underlying physical and chemical phenomena. In academic field and industry Computational Fluid Dynamics (CFD) has been very important tool for this purpose. Using CFD, the ability to predict auto-ignition process highly depends on capturing the instabilities of flow field and the accurate description of chemical mechanism. The latter one is the subject of this work.

1.2 State of the art

The combustion timing of CAI is controlled by the chemical kinetics and highly depends on the properties of the mixture field [126, 63, 64, 7, 13, 31, 43]. Inhomogeneities in the mixture and temperature field designate the combustion characteristics of CAI [126, 63]. Thus, the prediction of the auto-ignition process requires an accurate description of the chemistry within the whole range of thermodynamic conditions given by thermal and composition inhomogeneities. In order to accurately predict the complex reaction chemistry of the auto-ignition process, detailed reaction mechanisms have been developed [11, 12].

There are several works existing based on coupling detailed chemistry with one dimensional (1d) engine codes which simulate auto-ignition processes in HCCI engine-like configuration. In [125] the chemistry solver CHEMKIN (single zone detailed chemical kinetics model) code is coupled with WAVE to study HCCI engine operating conditions and their effects. In [74, 75] CHEMKIN and Lotus Engine Simulation are coupled where in the both works influence of variable valve timings on the gas exchange process in a controlled auto-ignition engine are studied. In [82] different from previous works, instead of a single zone-model a multi-zone combustion model is coupled with 1d engine simulator where again a HCCI-engine like configuration is studied. In [77, 28, 29] CHEMKIN GT-Power and stochastic reactor model (SRM) are coupled. These listed works however do not correspond to complex CAI configurations. These are not accounting for inhomogeneities and they are only valid for HCCI configuration. Furthermore, they are not capable to show cycle-to cycle variations of in-cylinder flow. However, they contribute to the understanding of the auto-ignition processes and the developing auto-ignition mechanisms, therefore are very important.

Coupling detailed reaction kinetics directly with a three dimensional (3d) CFD code with full spatial and temporal resolution is, in principle, also possible. However, such detailed chemistry simulations are computationally extremely expensive, rendering them infeasible as simulation tools for practical systems of technical scale. One way is to use strongly reduced kinetic schemes which consider only the most important species and their reactions. Methods such as Computational Singular Perturbation (CSP) [59] and the intrinsically low dimensional manifold (ILDM) [19] perform the reduction automatically based on a mathematical analysis that considers the time scales of the underlying chemical kinetics.

Simplified models for combustion implicitly take the coupling of chemical kinetics and molecular transport into account, like the flamelet model [91]. For the prediction of finite rate chemistry effects, flamelet models have been extended with a progress variable approach [96, 94], variants are the Flamelet Generated Manifolds (FGM) [84], the Flamelet Prolongation of ILDM (FPI) [36], and the Reaction Diffusion Manifold (REDIM) method [19]. For cases where the chemical reaction occurs without a strong coupling to diffusive processes, for instance, auto-ignition in mixtures with weak scalar gradients, other models have been developed [16].

In industrial applications due to their convenient computational costs Reynolds-Averaged Navier Stokes (RANS) models are used for simulation of turbulent flows. Therefore, there are several work exist where RANS based CFD codes are coupled either to a detailed chemistry solver directly or to a pre-tabulated detailed chemistry approach. In [109, 115, 56] the code is coupled with CHEMKIN. In [115] the effects of inhomogeneous distributed EGR gas inside cylinder are invested. In [64] the CFD code from CD adapco employing the RNG turbulence model is coupled with CHEMKIN and a reduced chemical kinetics including 42 chemical species and 58 elementary reactions is used. In [102] the CFD calculations have been performed with AVL-Fire code using k$-\epsilon$ turbulence model. An extended coherent flame model (ECFM-3Z) is used for the simulation of the diesel HCCI combustion in perfectly or partially mixed conditions and also it accounts for unmixed portion. In [79] a reduced mechanism for HCCI combustion from [51] used with Ansys CFX for different RANS models. In [34] the KIVA-4mpi code is coupled with another detailed chemistry solver, the CANTERA code. Each cell is considered a constant volume reactor without walls, mass exchange or any work exert on them during the kinetics calculation. Each one of this group of reactors is part of the simulation domain. The reactor remains isolated during Cantera calculations. Then KIVA-4mpi couples the reactor with the fluid via diffusion transport. The role of Cantera in the particular work is to isolate the time scales of the kinetic reaction from the scales of the fluid phase. In [119] which is continuous work of [54, 55], the code IFP-C3D (based on RNG k-epsilon model) is coupled with pre-tabulated detailed chemistry where the Senkin code is used for pre-tabulation of detailed chemistry. A detailed mechanism containing 1992 reactions and 416 species is used for constant pressure, homogeneous adiabatic reactors. A total of 68,400 complex chemistry simulations are performed with different thermodynamic conditions. The look up table with a wide range of input variables is then coupled with the code IFP-C3D. In [22] a new version of dynamic adaptive method (TDAC) is presented. TDAC couples a tabulation method with a mechanism reduction method. In the work, the new TDAC method is applied to HCCI case for simplified and also for detailed cases. A simple approach is to map pre-computed information about the chemical dynamics in detailed homogeneous reaction systems onto a reduced model, whose source term is then tabulated and used in CFD simulations [57].

As listed above several RANS based works exist to simulate HCCI or CAI. However, RANS models solve the temporal mean value of the relevant quantities of the system. With regard to a more accurate prediction of situations that intrinsically depend on temporal and spatial variations associated with turbulence, the Large Eddy Simulation(LES) has

been established as a turbulence model. Within LES the large scale motions are explicitly resolved to accurately predict the conditions prior to ignition. Particular those are the mixing of the injected fuel with the air, the EGR distribution within in the cylinder and the thermal conditions associated with them.

LES has been applied to HCCI in several works. In [129, 130, 131] a detailed reaction mechanism is coupled with the LES code using a progress variable approach. Within these consecutive works the authors investigated the sensitivity of the HCCI combustion with respect to an initially imposes turbulence level and temperature inhomogeneity. In [122, 133] the knock phenomena in HCCI engine is studied with detailed chemical kinetics coupled to LES codes. A model called Ignition to Propagation Reduced Scheme (IPRS) is introduced in [76] to predict abnormal combustions in IC engines in the context of LES. This model uses a single reduced chemical scheme (with two reactions) to describe both auto-ignition (AI) and propagation.

1.3 Aim and scope of this work

This work aims to contribute to the understanding of combustion phenomena in CAI engines and therefore to the development of them. More particularly, the aims of this work are

1. Introduce a multi-dimensional tabulation approach to cover all inhomogeneities in mixture and temperature fields that occur the particular CAI engine.
2. Coupling tabulated chemistry approach to the LES-CFD code
3. Demonstrate the application of the multi-dimensional chemistry table to a real engine
4. Characterize the thermal and mixture inhomogeneities to explain the occurrence of ignition kernels
5. Provide an understanding of the combustion process and the interaction between cycles (cycle-to-cycle variations)

1.4 Structure of this work

Following the introduction, chapter two presents basic background of the internal combustion engines. In chapter three the fundamental relations in the fluid flow, a basic knowledge of turbulent flows and their numerical treatments are outlined. In chapter four the employed combustion model being, the tabulated chemistry approach and its coupling to the CFD code are introduced. In chapter five the numerical scheme and general solution procedure of the CFD code are given. Chapter six is devoted to the verification of the ignition model and its coupling to the CFD code, where the results from homogeneous reaction simulations and 1 dimensional engine simulation are compared with the detailed chemistry. In chapter seven experimental

setup and configuration of the simulated CAI engine, the computational domain of the engine and the results from CAI simulations are presented. Finally, in chapter eight the results are summarized and concluded. The coupling/verification of the ignition model and analysis of results follow the presentation of [128] and [127], respectively.

Chapter 2

Background of internal combustion engines

Internal combustion engines (ICE) mainly differ from each other according to:

- The operation cycles: Two-stroke or four stroke
- The mixture preparation: Premixed or direct injection
- The combustion art: Spark ignition or auto-ignition
- The fuel used: Diesel, gasoline etc.

In this work a four stroke engine is of interest. Therefore in this section general basic knowledge of four-stroke ICEs will be outlined. The details about the investigated engine will be given in section 7.1.

2.1 Geometric parameters

In Figure 2.1 basic geometric parameters of a single cylinder engine are schematically plotted. Following the denotations of the geometric parameters are listed:

- B: The bore diameter
- s: The stroke length
- L: Connecting rod length
- r: The crank radius
- ϕ: Crank angle
- ω: Angular speed
- V_c: Clearance volume
- V_h: Displaced or swept volume

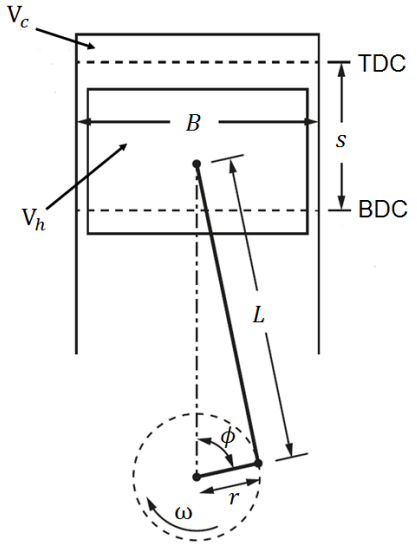

Figure 2.1: Schematic representation of basic parameters of an single cylinder engine [40].

Using these geometric parameters other important information of an engine are obtained:

Mean piston speed $\bar{v_p}$:

$$\bar{c_p} = 2hn \tag{2.1}$$

where $h = 2r$ and n is the rotational speed (rpm).

Piston position at given crank angle $z_p(\phi)$:

$$z_p(\phi) = r\left[1cos\phi + \frac{L}{r}\left(1 - \sqrt{1 - \left(\frac{r}{L}\right)^2 sin^2\phi}\right)\right] \tag{2.2}$$

Instantaneous piston velocity v_p:

$$v_p = \frac{z_p}{dt} = r\omega\left(sin\phi + \frac{r}{2l}\frac{sin2\phi}{\sqrt{1 - \left(\frac{r}{L}\right)^2 sin^2\phi}}\right) \quad \text{with} \quad \omega = \frac{d\phi}{dt} \tag{2.3}$$

Compression ratio of an engine ϵ_{comp}:

$$\epsilon_{comp} = \frac{V_t}{V_c} \tag{2.4}$$

Where V_t is the total cylinder volume with $V_t = V_c + V_h$.

2.2 Thermodynamics of internal combustion engines

Internal combustion engines convert chemical energy in mechanical energy. First, chemical energy of a fuel is converted into thermal energy, Q_{in} and then this thermal energy is converted into mechanical energy (work). Since not the whole thermal energy is converted to mechanical energy (heat losses, friction etc.) a certain amount of thermal energy is wasted. To judge on the energy conservation performance of an engine, a dimensionless quantity, the thermal efficiency η_{th} is generally defined as:

$$\eta_{th} = \frac{Q_{in} - Q_{out}}{Q_{in}} \tag{2.5}$$

where Q_{out} is the dissipated heat for instance due to heat losses and friction, therefore $\eta_{th} < 1$.

Another important and useful engine performance indicator is the mean effective pressure (IMEP) p_i. IMEP describes an averaged pressure acting on piston during the whole cycle (over 720 cad (=crank angle degree)) and it is independent from engine size.

$$p_i = \frac{W_i}{V_h} \tag{2.6}$$

In Eq.(2.6) W_i is the indicated work. W_i is obtained by integrating pressure - volume (p-V) diagram of an engine cycle $W_i = \oint pdV$. An exemplary $p - V$ diagram of a four stroke Otto engine is plotted in Figure 2.2. A four stroke operation cycle involves intake, compression, ignition and exhaust steps which progress during two crankshaft rotations per working cycle of engine. *Intake stroke:* Intake phase starts while the piston is at the Top Dead Center (TDC) and the piston goes down and the fresh charge flows in the cylinder (7-1). *Compression stroke:* Piston compresses the air-charge to a small volume through the TDC while both valves are closed. During this stroke in cylinder, pressure and temperature rise rapidly due to initiation of combustion (1-2). *Power/Expansion stroke:* Starts from TDC and high pressure caused by combustion, pushes the piston back down to Bottom Dead Center (BDC) (3-4). *Exhaust stroke:* As the piston reaches to BDC, the exhaust valves open and the burnt gas leaves the cylinder. As the piston reaches TDC the inlet valves open and intake stroke starts again (4-7) [40].

The thermal efficiency η_{th} can be calculated under using thermodynamic relations under assumptions of ideal gas and isentropic expansion. The following relations are given for an ideal Otto engine. Further information about thermodynamics can be found in [40]. Applying the first law of thermodynamics to an Otto engine process, the compression work (1-2) W_C is

$$W_C = \int_{T_1}^{T_2} mc_v dT \tag{2.7}$$

Where c_v is the specific heat constant at constant volume. The net heat of combustion (2-3) at roughly constant volume is

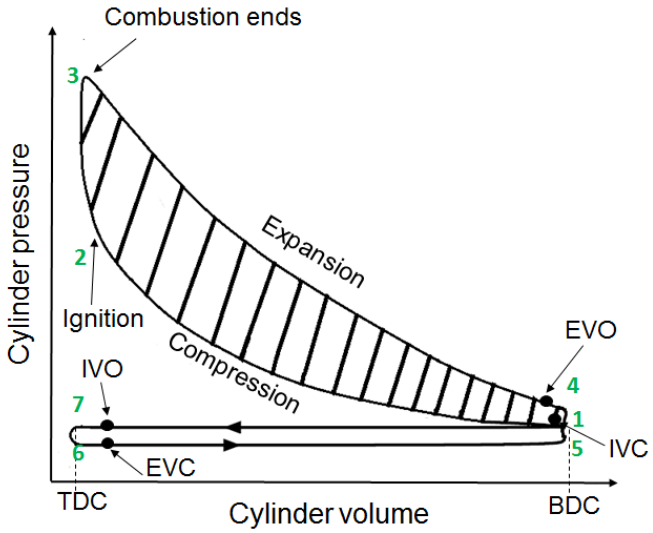

Figure 2.2: Examplary diagram of $p-V$ of a non-ideal Otto engine. IVO: Inlet valve open, IVC: Inlet valve close, EVO:Exhaust valve open, EVC:Exhaust valve closed.

$$Q_{in} = \int_{T_2}^{T_3} mc_v dT \tag{2.8}$$

and the expansion work (3-4) W_E is

$$W_E = \int_{T_3}^{T_4} mc_v dT \tag{2.9}$$

Now using Eq.s (2.7), (2.8) and (2.9), η_{th} can be rewritten as follows

$$\eta_{th} \approx \frac{(T_3 - T_4) - (T_2 - T_1)}{(T_3 - T_2)} = 1 - \frac{T_4 - T_1}{T_3 - T_2} \tag{2.10}$$

Since 1-2 and 3-4 are assumed to be isentropic under same volumes, the relation between unburnt temperature (T_1) and burnt temperature (T_4) can be expressed as a function of compression ratio ϵ_{comp}:

$$\frac{T_2}{T_1} = \left(\frac{V_1}{V_2}\right)^{\gamma-1} = \left(\frac{V_4}{V_3}\right)^{\gamma-1} = \frac{T_3}{T_4} = \epsilon_{comp}^{\gamma-1} \tag{2.11}$$

where $\gamma = c_p/c_v$ with c_p the specific heat constant at constant pressure.

With the help of this brief thermodynamic analysis of an Otto engine cycle, one can show that overall efficiency η_{th} increases if the compression ratio increases:

$$\eta_{th} \approx 1 - \frac{1}{\epsilon_{comp}^{\gamma-1}} \tag{2.12}$$

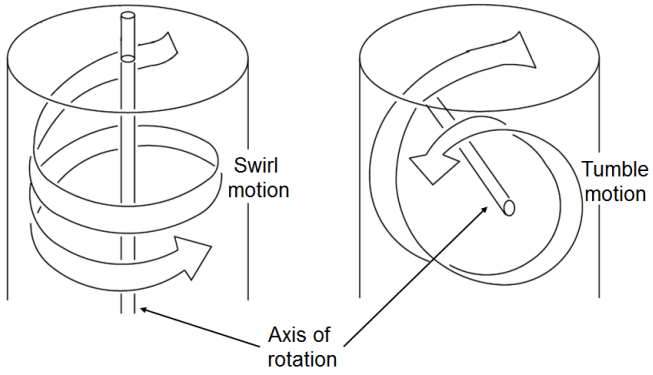

Figure 2.3: Swirl and tumble motion of engine flow from [61].

2.3 Flow motion characteristics

Engine flows are turbulent. The turbulent behaviour of the flow is first initiated by inflow process. During the intake process at valve openings flow charge has the highest velocity and enters into the cylinder as a conical jet. As jet separates from valves, shear layers with high velocity gradients are produced and therefore the flow becomes turbulent [40].

Both the bulk gas motion and turbulent characteristics of the flow have an immense influence on engine combustion and heat transfer. The more turbulence is generated the better mixing process, heat transfer and more stable combustion are [61]. The turbulence resulting from inlet jet decays rather fast, and not much is left for ignition. In order to encapsulate some of the momentum of the inlet valve jet, organized large motions are generated in engine cylinder, which are less dissipative than turbulence (due to their large scales) and therefore retain energy longer [67]. These organized motions are the so-called *"swirl"* and *"tumble"* motions.

In Figure 2.3 swirl and tumble motions are represented schematically respectively. In case of swirl motion the flow rotates around the longitudinal axis of cylinder and for tumble motion the rotation axis is perpendicular to the cylinder axis. Swirl is used in diesel engines and is controlled by piston bowl geometries, intake port design, swirl control rings etc. Tumble motion is used in Otto engines, more complex and difficult to control. It can be evoked by using e.g. tumble flaps or intake runners.

2.4 Combustion in ICE

Internal combustion engines are mainly named after their combustion characteristics and the fuel with which they are operated. In ICE principally there are two types of combustion namely spark ignition (SI) and compression ignition (CI).

In conventional SI engines fuel is mixed with the air in intake port. The air-fuel mixture is compressed and usually between 10 and 40 crank angle degrees before TDC

Table 2.1: RON of some selected fuels [65]

Fuel	RON
Propane (C_3H_8)	112
n-Octane (C_8H_{18})	-20
iso-Octane (C_8H_{18})	100
n-Heptane (C_7H_{16})	0
Toluene (C_7H_8)	120

an electrical discharge originating from spark plug ignites the mixture. A turbulent flame starts to propagate and it extinguishes at the cylinder wall. Typically, in SI engines the combustion duration is between 40 to 60 crank angles [40].

In conventional CI engines, the air alone is induced into the cylinder. The fuel is directly injected into the combustion chamber as the piston almost reaches to TDC. The air has high temperature as piston reaches to TDC due to the compression and as a result, the fuel auto-ignites as it is injected.

The decision of the fuel to be used in an internal combustion engine depends on how combustion takes place in the engine. In conventional SI and CI engines combustion is controlled by spark and fuel injection respectively. During SI engine combustion two abnormal combustion phenomena can occur namely, *pre-ignition* and *engine knock*. The pre-ignition is defined as ignition prior to spark timing and caused for instance, by temperature inhomogeneities (hot spots). The engine knock is defined as spontaneous combustion of the last remaining unburnt gas in cylinder *end gas*. Therefore, to prevent these phenomena in SI engines, fuels with high ignition resistance are used, whereas in CI engines fuels with low resistance are preferred. To compare ignition resistance of fuels the *cooperative fuel research committee* (CFR) defined a scale so called octane number (ON or RON) in 1930 [124]. According to this definition of CFR, RON values of n-Heptane (C_7H_{16}) and iso-octane (C_8H_{18}) are exactly 0 (high tendency to ignite) and 100 (low tendency to ignite) respectively. In table 2.1 RON numbers of some selected fuels are given. Accordingly, the most common types of ICEs used in the transportation sector are gasoline (RON of 100-90) fuelled SI and diesel fuelled (RON of 15-12) CI engines. The RON ratings of these commercial fuels varies by mixture preparation of the fuel.

Nowadays the SI engines are typically operated with stoichiometric ($\lambda = 1$) mixtures where the charge load control is only possible by controlling air flow in-cylinder with a throttle [126]. The throttle used gives however rise to pumping loses and reduces the efficiency. Additionally, due to knock problems, SI engines have limited compression ratios ($\epsilon_{comp} = 8-12$). As a result, SI engines have a major disadvantage of low efficiency. Diesel engines on the other hand, have much higher compression ratios (typically lies between $\epsilon_{comp} = 12 - 24$) than SI engines and as a result they have higher efficiency

Table 2.2: Comparison of SI, CI, HCCI, PCCI and RCCI from [5]

.

	SI	CI	HCCI	PCCI	RCCI
Ignition type	Spark	Compression	Compression	Compression	Compression
Fuel type	High octane	Low octane	Blend of fuels	Blend of fuels	PFI of highoctane, DI of low octane
Power output control	Air-flow control (throttle) and stoich. λ	Fuel flow control with lean λ	Fuel flow control with lean λ or charge dilution	Fuel flow control with lean λ and EGR	Fuel reactvity stratification
Combustion controlling	Flame propagation speed	Injection time, fuel vaporization, and mixing	Chemical kinetics	Chemical kinetics and injection timing	Chemical kinetics and fuel reactivity
Emission characteristics	High CO_2	Higher PM and NO_x lower CO_2	Higher UHC and CO and lower PM, NO_x and CO_2	Higher UHC and CO and lower PM, NO_x and CO_2	Very high UHC and CO and ultra-low PM, NO_x and CO_2

($\eta_{th} \approx 1 - 1/\epsilon_{comp}^{\gamma-1}$). However, in diesel engines, the spray combustion is complex which depends on the droplet evaporation, collision etc. [126]. In regions with high fuel concentrations formation of soot is strong and this rich mixture burns out in a high temperature ($\sim 2700K$) diffusion flame where large amounts of NO_x are formatted [26, 24, 126]. Using advanced systems such as exhaust gas (EGR) recirculation, modifying engine geometries, increased injection pressure, improved air flow (e.g. swirl) emission formation of diesel engines are reduced. However still in future emission due to more strict regulations of emissions using fairly expensive after treatment systems for diesel engines seem unlikely [26].

In order to reduce the emission formation for high efficiency CI engines, engine researchers are interested in alternatives of CI combustion. At this point homogeneous charge compression ignition (HCCI) engines are of technological interest. In HCCI engine fuel and air is premixed and ignition occurs due to compression of the mixture. HCCI works with very dilute mixtures that high local peak temperatures are avoided, thus reducing the NO_x formation. Furthermore, since the charge is well-mixed, soot formation is prevented [27, 26, 23, 126, 35]. Additionally, thermal efficiencies of HCCI engines are typically comparable to those of a diesel engine [132]. However, since high peak pressures and heat releases occur at high loads, the HCCI technology is applied for a limited range of load. To overcome this issue, strategies are developed to control HCCI combustion which refers to the Controlled Auto Ignition (CAI) concept [126, 35].

Several CAI strategies exist such as early direct injection [113], multiple fuel injections [112], variable inlet temperature [121] and internal or external Exhaust Gas Recirculation (EGR) [126] etc. Engine researchers focused lately on two CAI engines types so called Partially premixed compression ignition (PCCI) [126, 66, 35, 106, 105] and reactivity-controlled compression ignition engines (RCCI) [103]. PCCI mode combines early injection with EGR [5]. Injecting fuel early decouples combustion and fuel injection, where it helps to reduce soot formation. EGR acts as a dilutant of the fresh fuel-air mixture and is one of the strategies used for controlling HCCI combustion [26, 126, 35]. The EGR is either achieved by trapping hot exhaust gas in-cylinder with the Negative Valve Overlap (NVO) concept or burnt gas load during intake, so called Burnt Gas Re-Breathing (BGRB)[126]. RCCI method is introduced by Inagaki [53] for controlling

PCCI by means of varying fuel reactivity [5].

In table 2.2 the key characteristics of the SI, CI, HCCI and PCCI engines are summarized. In this work the engine configuration has PCCI-like operation characteristics. After combustion hot exhaust gas is trapped in-cylinder and the fuel is injected into cylinder early before intake valves open (IVO). The details on the studied CAI engine will be given in sections 7.1 and 7.3.1 respectively.

Chapter 3

Description and modeling of turbulent flows

This chapter is divided in four parts. In the first part, the basic equations to compute flow motion are outlined. The second part is devoted to a succinct background of internal combustion engines with regards to geometric properties, flow characteristics and thermodynamics. The third part presents the turbulence phenomena and the fourth part is devoted to numerical modeling strategies of turbulent flows.

3.1 Basic Equations

The fluid motion can be described by a set of coupled, non-linear, partial differential equations. These equations consist of conservation of mass, momentum and energy. In case of reacting systems additional equations for the species partial densities have to be considered. In this work the basic equations describe a two-phase system with a gas and liquid phase, respectively, where the latter corresponds to spray.

The three dimensional, unsteady and compressible transport equations are formalized in a common notation used for Cartesian tensors as it is used in [33], where Einstein summation convention is applied for indices i, j, k. For further information of derivation of transport equations and notation the reader is refereed to [33] and [107].

Mass can neither be created nor be destroyed. Hence, the mass is conserved. The conservation of mass in Eq. (3.1) describes the local change of density ρ in time.

$$\frac{\partial \rho}{\partial t} + \frac{\partial (\rho u_j)}{\partial x_j} = \dot{\rho}^s \tag{3.1}$$

where $\dot{\rho}^s$ corresponds to the increase in mass after evaporation of droplets originating from spray. According to Newton's law velocity of a given fluid particle does not change unless an external force acts on it. Hence, likewise mass, the momentum is conserved. The equation of momentum conservation is given in Eq. (3.2).

$$\frac{\partial (\rho u_i)}{\partial t} + \frac{\partial (\rho u_i u_j)}{\partial x_j} = \frac{\partial}{\partial x_j}\tau_{ij} - \frac{\partial p}{\partial x_i} + \rho f_i^s + \rho g_i \tag{3.2}$$

where τ_{ij}, p, f_i^s and g_i are the stress tensor, the pressure, the rate of momentum gain per unit volume due to interaction with liquid phase, and the gravity respectively. Since

in this work only Newtonian fluids [110] are considered, τ_{ij} expressed as

$$\tau_{ij} = \mu \left(\frac{\partial u_i}{\partial x_j} + \frac{\partial u_j}{\partial x_i} \right) - \frac{2}{3} \frac{\partial u_k}{\partial x_k} \delta_{ij} \tag{3.3}$$

with μ being dynamic viscosity and δ_{ij} is Kronecker delta.

$$\delta_{ij} = \begin{cases} 1 & \text{for } i = j \\ 0 & \text{for } i \neq j \end{cases} \tag{3.4}$$

In systems with chemical reactions and spray, the total gas phase mass changes only due to spray evaporation as given in Eq. (3.1). However in such multi-component systems species concentration changes temporally and spatially not only due to spray but also chemical reactions. Hence, additional equations for partial densities are needed. In the case of a chemically reactive fluid consisting of n_s separate fluid species the partial density ρ_m of each species m has the relation with total density ρ as defined in Eq. (3.5).

$$\rho = \sum_{m=1}^{n_s} \rho_m \tag{3.5}$$

The balance equation of ρ_m with time is written as follows

$$\frac{\partial(\rho_m)}{\partial t} + \frac{\partial(\rho_m u_j)}{\partial x_j} = \frac{\partial}{\partial x_j} \left(\rho D_m \frac{\partial}{\partial x_j} \left(\frac{\rho_m}{\rho} \right) \right) + \dot{\rho}_m^{\text{chem}} + \dot{\rho}_m^{s}. \tag{3.6}$$

with D_m of the species m is given by Fick's Law of diffusion

$$D_m = \frac{\nu}{Sc_m} \tag{3.7}$$

where ν is kinematic viscosity $\nu = \mu/\rho$ and Sc_m is the Schmidt number of the specie m. During chemical reaction one species may be converted into one or more others. This change due to chemical reaction is represented by the source term $\dot{\rho}^m_{\text{chem}}$ in Eq. (3.6). The second source term $\dot{\rho}^m_s$ in Eq. (3.6) arises from injection of species m into the fluid, referred to as a spray. Now for such a system mass consistency must be fulfilled:

$$\sum_{m=1}^{n_s} \left(\frac{\rho_m}{\rho} \right) = 1 \tag{3.8}$$

Mass fraction of species m is

$$Y_m = \frac{\rho_m}{\rho} \tag{3.9}$$

Inserting Y_m in Eq. (3.6), one obtains a general form for scalar transport equation with source term ω_m. The source term corresponds to the sink or source term for species m due to chemical reaction.

$$\frac{\partial(\rho Y_m)}{\partial t} + \frac{\partial(\rho Y_m u_j)}{\partial x_j} = \frac{\partial}{\partial x_j} \left(\rho D_m \frac{\partial Y_m}{\partial x_j} \right) + \dot{\omega}_{\text{m}} \tag{3.10}$$

For the description of an engine system which is reactive, compressible and non-adiabatic, an energy equation is to be solved to calculate temperature T. The specific internal energy e is solved as

$$\begin{aligned}\frac{\partial(\rho e)}{\partial t}+\frac{\partial(\rho e u_j)}{\partial x_j}=-p\frac{\partial u_j}{\partial x_j}+\tau_{ij}\frac{\partial u_i}{\partial x_j}+\frac{\partial}{\partial x_j}\left(\lambda\frac{\partial T}{\partial x_j}\right)+\\ \frac{\partial}{\partial x_j}\left[\rho D_{th}\sum_m h_m\frac{\partial}{\partial x_j}\left(\frac{\rho_m}{\rho}\right)\right]+\dot{\omega}_{\text{heat}}+\dot{\omega}^s\end{aligned} \tag{3.11}$$

where Pr is Prandtl-Number and $D_{th}=\frac{\nu}{Pr}$. The third term on the right hand of Eq. (3.11) $\left(\lambda\frac{\partial T}{\partial x_j}\right)$ accounts for thermal diffusion and the fourth term on right hand of Eq. (3.11) $\left[\rho D_{th}\sum_m h_m\frac{\partial}{\partial x_j}\left(\frac{\rho_m}{\rho}\right)\right]$ accounts for enthalpy transport by species. Finally, $\dot{\omega}_{\text{heat}}$ and $\dot{\omega}^s$ correspond to heat source terms resulting from heat released during chemical reactions and heat source or sink due to spray interactions respectively.

Finally, to complete description of the system additional to equations above two state relations are needed, namely these are the thermodynamic equation of state, which is the ideal gas law in this work and the calorific equation of state given in Eq. (3.12) and (3.14) respectively.

$$p=\rho\bar{R}T \tag{3.12}$$

$\bar{R}=\frac{R}{\bar{W}}$ is averaged gas constant and R is universal gas constant and $\bar{W}$ is averaged molecular weight

$$\bar{W}=\left(\sum_{m=1}^{N_S}\frac{Y_m}{W_m}\right)^{-1}. \tag{3.13}$$

$$e=\int_{T_0}^{T}c_v\,\mathrm{dT}-\bar{R}T_0\,. \tag{3.14}$$

T_0 is the reference temperature and c_v is the specific heat capacity at constant volume

$$c_v=\sum_{m=1}^{n_s}c_{v,m}\left(\frac{\rho_m}{\rho}\right) \tag{3.15}$$

To finalize this section the governing equations for chemically reacting fluid flow in three-dimensions are summarized below:

Conversation of mass:

$$\frac{\partial\rho}{\partial t}+\frac{\partial(\rho u_j)}{\partial x_j}=\dot{\rho}^s \tag{3.16}$$

Conservation of momentum:

$$\frac{\partial(\rho u_i)}{\partial t}+\frac{\partial(\rho u_i u_j)}{\partial x_j}=\frac{\partial}{\partial x_j}\tau_{ij}-\frac{\partial p}{\partial x_i}+\rho f_i^s+\rho g_i \tag{3.17}$$

Conservation of energy:

$$\frac{\partial(\rho e)}{\partial t} + \frac{\partial(\rho e u_j)}{\partial x_j} = -p\frac{\partial u_j}{\partial x_j} + \tau_{ij}\frac{\partial u_i}{\partial x_j} + \frac{\partial}{\partial x_j}\left(\lambda\frac{\partial T}{\partial x_j}\right) + \frac{\partial}{\partial x_j}\left[\rho D_{th}\sum_m h_m \frac{\partial}{\partial x_j}\left(\frac{\rho_m}{\rho}\right)\right] + \dot{\omega}_{\text{heat}} + \dot{\omega}^s \tag{3.18}$$

Equations of state:

$$p = \rho\bar{R}T \tag{3.19}$$

$$e = \int_{T_0}^{T} c_v \mathrm{dT} - \bar{R}T_0. \tag{3.20}$$

Conservation of mass for chemical species m

$$\frac{\partial(\rho_m)}{\partial t} + \frac{\partial(\rho_m u_j)}{\partial x_j} = \frac{\partial}{\partial x_j}\left(\rho D_m \frac{\partial}{\partial x_j}\left(\frac{\rho_m}{\rho}\right)\right) + \dot{\rho}_m^{\text{chem}} + \dot{\rho}_m^s. \tag{3.21}$$

Mass consistency:

$$\sum_{m=1}^{n_s}\left(\frac{\rho_m}{\rho}\right) = 1 \tag{3.22}$$

3.2 Turbulence

Flow behaviour in a system depends mainly on the characteristics of the fluid (viscosity and density), the velocity of the flow and the geometric properties of the system. Reynold Number Re constitutes the relation between these factors.

$$Re = \frac{\rho\mathcal{U}\mathcal{L}}{\mu} \tag{3.23}$$

where $\mathcal{U}$ is the characteristic velocity and $\mathcal{L}$ is the characteristic length of the given system. Reynolds number represents the ratio of inertial forces to viscous forces. In case of low Reynolds numbers viscous forces damps the perturbations in flow caused by the inertial forces and the flow is laminar. On the contrary turbulent flows occur in high Reynolds numbers, where the flow is dominated with the inertial forces and acts chaotic. Hence, the magnitude of Reynolds number is decisive for whether a flow is laminar or turbulent.

In most of technical applications flow is turbulent. Turbulence is a three dimensional, transient, random and highly irregular in space and time. Due to random and transient nature of turbulence, statistical moments are used for its definition. Accordingly, an arbitrary quantity having this random and transient nature $\Phi(x_i, t)$ can be expressed as the sum of its time averaged $\bar{\Phi}(x_i)$ and fluctuating part $\Phi'(x_i, t)$ (Reynolds decomposition).

$$\Phi(x_i,t) = \bar{\Phi}(x_i) + \Phi'(x_i,t) \tag{3.24}$$

The quantity Φ is averaged over time τ as follows

$$\bar{\Phi}(x_i) = \lim_{\tau\to\infty} \frac{1}{\tau} \int_{t_0}^{t_0+\tau} \Phi(x_i,t)dt \tag{3.25}$$

and the standard deviation

$$\Phi(x_i,t)_{\text{rms}} = \lim_{\tau\to\infty} \left[\frac{1}{\tau} \int_{t_0}^{t+\tau} \Phi'(x_i,t)^2 dt\right]^{1/2} \tag{3.26}$$

where rms stands for root mean square.

For engine applications similar to Reynolds time-averaging a phase-averaging approach is used. For that purpose the flow property $\Phi(x_i,t)$ is defined as a function of crank angle (ϕ) instead of time t:

$$\Phi(x_i,t) \to \Phi_j(x_i,\phi) \tag{3.27}$$

where j denotes the corresponding cycle and the averaged value of $\Phi_j(x_i,\phi)$ is calculated by phase averaging over N number of cycles

$$\langle\Phi(x_i,\phi)\rangle = \frac{1}{N}\sum_{j=1}^{N} \Phi_j(x_i,\phi) \tag{3.28}$$

Accordingly, Eq. (3.24) and (3.26) can be rewritten for engine applications as follows

$$\Phi_j(x_i,\phi) = \langle\Phi(x_i,\phi)\rangle + \Phi'_j(x_i,\phi) \tag{3.29}$$

$$\Phi(x_i)_{rms} = \left[\frac{1}{N}\sum_{j=1}^{N} \Phi'_j\langle x_i,\phi\rangle^2\right]^{1/2} \tag{3.30}$$

Time averaging of u_i in Eq. (3.2) using Eq. (3.25) and (3.24) gives a rise to a very important quantity $\overline{u'_i u'_j}$ so called *Reynolds Stress Tensor*. By adding up diagonal terms of this tensor the kinetic energy caused by the fluctuations, turbulent kinetic energy k is yielded

$$k = \frac{1}{2}\overline{u'_i u'_i} \tag{3.31}$$

The turbulent flows consist of eddies with different length (ℓ) and time scales ($t(\ell)$). The length of the large eddies (l_0) are related with the characteristic length of the system ($\mathcal{L}$) and their characteristic velocity u_0 is on order of $u_{rms} \equiv \left(\frac{2}{3}k\right)^{1/2}$ comparable to $\mathcal{U}$. Accordingly, the energy and time scale of large eddies are u_0^2 and $\tau_0 = l_0/u_0$ respectively. Knowing these terms, the production of energy $\mathcal{P}$ can be formulated as given in Eq. (3.32).

$$\mathcal{P} = u_0^2/\tau_0 = u_0^3/l_0 \tag{3.32}$$

With the assumption of steady and homogeneous turbulence [98], the production $\mathcal{P}$ is equal to ϵ the rate of turbulent kinetic energy dissipation. ϵ is a function of

$$\epsilon = 2\nu\overline{S'_{ij}S'_{ij}} \tag{3.33}$$

where S'_{ij} is the symmetric part of the fluctuating velocity gradient tensor:

$$S'_{ij} = \frac{1}{2}\left(\frac{\partial u'_i}{\partial x_j} + \frac{\partial u'_j}{\partial x_i}\right) \tag{3.34}$$

The large eddies involve high energies and they break up to smaller eddies until they are dissipated to heat by viscous forces. This phenomena corresponds to the *energy cascade*[1] concept. On the left side of Figure 3.1 turbulent scales are illustrated schematically where η is the smallest eddy size. On the right side of the Figure 3.1 the distribution of turbulent kinetic energy onto different sized eddies is illustrated schematically where energy spectrum function $E(\kappa)$ is plotted against wave-number $\kappa = 2\pi/\ell$. From this plot one can see that the large eddies have most of energy. The turbulent energy reduction in inertial sub-range is proportional to $E(\kappa)^{-5/3}$. Above the wave-number $\kappa = 2\pi/\ell_{ID}$ the turbulent kinetic energy is dissipated to heat. Kolmogorov formalized the smallest length scale η with his similarity hypothesis as a function of kinematic viscosity ν and dissipation rate of turbulent kinetic energy ϵ

$$\eta = \left(\frac{\nu^3}{\epsilon}\right)^{1/4} \tag{3.35}$$

Accordingly for velocity and time Kolomogorov scales are defined in Eq. (3.36) and Eq.(3.37) respectively.

$$u_\eta = (\epsilon\nu)^{1/4} \tag{3.36}$$

$$\tau_\eta = (\nu/\epsilon)^{1/2} \tag{3.37}$$

In case of engine applications the eddies responsible for most of the energy production are the large eddies created by conical intake jet flow. Their size is roughly equal to the jet thickness [40]. This scale is called the integral length ℓ_l and it corresponds to the largest structure in flow. The time scale τ_l is measure of the time a large eddy to pass a point. In order to find out these magnitudes first normalized autocorrelation of u' is calculated:

$$R_{ij}(x_k, t, \Delta x_k, \Delta t) = u'_i(x_k, t)u'_j(x_k + \Delta x_k, t + \Delta t) \tag{3.38}$$

where Δx and Δt are spatial and temporal distances respectively. The normalized form of autocorrelation, $R_{n_{ij}}$ is

$$R_{n_{ij}}(x_k, t, \Delta x_k, \Delta t) = \frac{\overline{u'_i(x_k, t)u'_j(x_k + \Delta x_k, t + \tau)}}{\sqrt{\overline{u'^2_i(x_k, t)}\,\overline{u'^2_j(x_k + \Delta x_k, t + \Delta t)}}} \tag{3.39}$$

[1]The first idea of energy cascade is introduced by Richardson [104]. Further information can be found in [98]

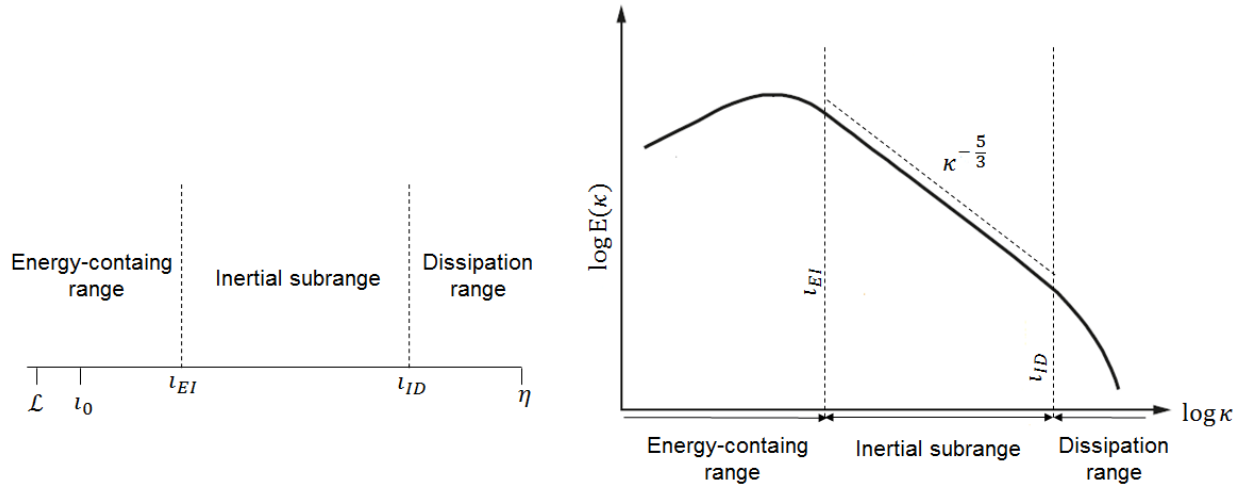

Figure 3.1: Schematic representation of Eddy length scales ℓ (Left) and energy spectrum for fully developed, locally homogeneous, isotropic turbulent flow (Right) from [98].

Integrating (3.39) over time t and the distance x the integral time and length scales are observed respectively:

$$t_{I,ij} = \int_0^\infty R_{n_{ij}}(x_k, t, \Delta t)\ \mathrm{d}(\Delta \mathrm{t}) \quad \text{and} \quad \ell_{I,ij} = \int_0^\infty R_{n_{ij}}(x_k, \Delta x_k, t)\ \mathrm{d}(\Delta \mathrm{x}_k)\ . \tag{3.40}$$

Knowing these scales turbulent Reynolds number Re_t can be defined as follows

$$Re_t = \frac{u_{rms}\ell_I}{\nu} \tag{3.41}$$

The relation between largest scales and Kolmogorov scales are

$$\eta/\ell_0 \sim Re_t^{-3/4} \tag{3.42}$$

$$u_\eta/u_0 \sim Re_t^{-1/4} \tag{3.43}$$

$$\tau_\eta/\tau_0 \sim Re_t^{-1/2} \tag{3.44}$$

3.3 Numerical treatment of turbulent flows

In most of technical applications flow is turbulent. In section 3.1 the equations describe the flow motion and they are also valid for turbulent applications. However for turbulent reacting flows within complex and moving geometries such as engine, these governing equations notoriously difficult and there is no simple analytic solution. Hence, with the specification of initial and boundary conditions these equations are solved numerically. For that purpose the physical domain of interest is mapped onto computational domain with the number of control volumes determine by the grid size $\Delta x_{i,j,k}$ and by solving discretized governing equations (see chapter 5). For each control volume the unknown quantities

are calculated and the flow is computed. For the simulation of turbulent flows basically three methods are established. These approaches are *Direct Numerical Simulation* (DNS), *Reynolds-averaged Navier Stokes* (RANS), *Large Eddy Simulation*(LES). In this section DNS and RANS methods will be outlined briefly while LES will be discussed in more detail since in this work LES technique is applied.

3.3.1 Direct Numerical Simulation (DNS)

In DNS approach the governing equations given in section 3.1 are solved without any model assumption for given initial and boundary conditions. Using these approach all length and time scales are resolved. Accordingly, the grid size of DNS must be fine enough to resolve smallest structures which correspond to Kolmogorov scales defined in Eqs. 3.35 and 3.37. A physical domain with characteristic length $\mathcal{L}$ is discretized in each direction with cells of grid size based on smallest scales. Then the number of control volumes would be $\frac{\mathcal{L}}{\eta} \times \frac{\mathcal{L}}{\eta} \times \frac{\mathcal{L}}{\eta}$. According to the relation between Kolmogorov scales and integral scales in Eq. (3.42), one can see clearly that number of control volume is proportional to $Re_t^{9/4}$. Assuming that temporal discretization is proportional to spatial discretization the total computational cost increases as Re_t^3. This shows that DNS has very high computational costs for industrial applications. Hence, it is only applicable to fundamental research areas with small domains.

3.3.2 Reynolds Averaged Formulation (RANS)

RANS approach delivers the mean flow field information. This information is obtained by applying time-averaging given in Eq. (3.25) to the flow field. In industrial applications RANS is a widely used approach, because with RANS computational costs are relatively low and the averaged flow field information is often sufficient for design of the system. For example, for engine design RANS is used as a practical CFD tool to investigate the tendencies of emission formations due to geometric modifications and accordingly, whether its worthy or not to apply these modifications of engine modification.

Applying time-averaging Eq. (3.25) to momentum Eq. (3.2) an unclosed term arises so-called *Reynolds stress tensor* $\overline{u_i' u_j'}$:

$$\overline{u_i' u_j'} = \overline{u_i u_j} - \overline{u}_i \overline{u}_j \tag{3.45}$$

This unclosed term −Reynolds stress tensor− is determined by a turbulence model. Several turbulence models exist which are either based on turbulent viscosity hypothesis or solving model transport equations for individual Reynolds stresses −Reynolds-Stress Model. The models based on turbulent viscosity hypothesis are mainly algebraic models, one-equation models and two equation models. The algebraic models describe the unknown terms directly (mixing length model). One equation models solve transport equation for turbulent kinetic energy and two equation models consist of the model transport equations for turbulent kinetic energy k and dissipation rate ϵ. From the models based on turbulent viscosity hypothesis, one of the most widely employed model is $k-\epsilon$ model which is based on turbulent viscosity hypothesis so-called Boussinesq-approximation and

it belongs to two-equation models. More details about the Boussinesq-approximation will be given section 3.3.3.

3.3.3 Large Eddy Simulation (LES)

In context of Large Eddy Simulation the low frequency structures corresponding to the large scales are temporally and spatially resolved and the high frequency small scale structures are modeled. The aim of LES approach is to compute unsteady turbulent flows within affordable computational costs. Considering the computational expense and accuracy, LES lies between DNS and RANS. DNS computes the flow field without any modeling approach and most of the computational effort of DNS arises from resolution of time and length scale of small structures (dissipative motions). The computational grid of DNS is scaled with Re_t^3 as illustrated in section 3.3.1. As a result DNS can be currently only used for small applications and the Re numbers are limited. However in LES, by modeling the small structures which requires very high resolution in time and space, the computational costs are affordable and LES can be applied to industrial applications. Also since within LES unsteady large scales structures are resolved it is more accurate and reliable than RANS.

3.3.3.1 Filtering

Low-pass filter for LES

In LES a low-pass filtering operation G is performed to achieve the separation between large and small scales. The general filtering operation was introduced by Leonard (1974) [4] and defined as follows

$$\bar{\Phi}(x_i,t) = \int_V G(x_i - x_i')\Phi(x_i',t)dx_i' \tag{3.46}$$

where integration is over the whole flow domain and the operation function satisfies the normalization condition to fullfill the conservation properties of the governing equations:

$$\int_V G(x_i - x_i')dx_i' = 1 \tag{3.47}$$

After filtering, analogous to the Reynolds decomposition (see Eq. (3.24)) the decomposition of $\Phi(x_i,t)$ is expressed as follows

$$\Phi(x_i,t) = \bar{\Phi}(x_i,t) + \Phi'(x_i,t) \tag{3.48}$$

where $\bar{\Phi}(x_i,t)$ and $\Phi'(x_i,t)$ correspond to fully resolved large scales and sub-filter scales to be modeled respectively. The filtering can be done in spectral space as well as physical space. In Figure 3.2 the filter operation in both physical space and spectral space (Fourier space) is schematically plotted. In this work, the filtering operation is performed in physical space. There are several filter functions such as, box filter, Gaussian filter, sharp spectral filter etc. The further information and details about different filter functions can

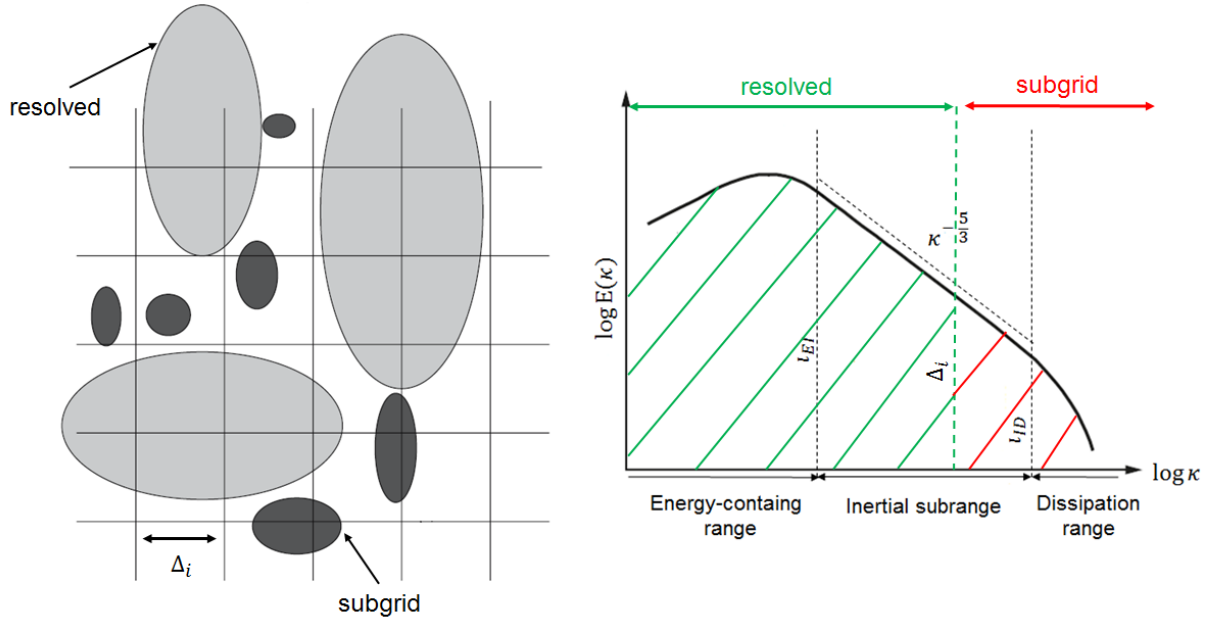

Figure 3.2: Schematic illustration of a simple filtering operation in both physical (left) from [86] and spectral space.

be found in [98]. One of the most widely used filter functions is the top-hat filter which has filter width of Δ_i and its function is defined in Eq. (3.49).

$$G(x_i) = \begin{cases} \prod_{i=1}^{3} \frac{1}{\Delta_i} & \text{if } |x_i'| \leq \frac{\Delta_i}{2} \\ 0 & \text{else} \end{cases} \tag{3.49}$$

LES filters can be applied implicitly or explicitly. The LES filtered governing equations (see section 3.3.3.2) are solved on a computational grid where a discretization operator is applied to these equations. By applying LES filtering and discretization operators on governing equations the turbulent flow is divided into resolved, subfilter and subgrid scales. In case of implicit filtering the cell is assumed to be the LES low-pass filter and no filter function is used for subfilter scales. In contrast by explicit filtering, filter function is defined explicitly and it calculates the contribution of subfilter scales [48]. In this work, LES filtering is performed implicitly in physical space using top-hat filter function. For detailed information about explicit and implicit filtering the reader is referred to [86, 30].

Favre filter

In engine density varies strongly due to compression of the medium and combustion. In such cases where density varies, in the filtered transport equations additional unclosed terms occur such as $\overline{\rho u_i' u_j'}$ which require further modelling. To avoid this, density weighted averaging so-called Favre-averaging [32] is applied. The Favre filtering is expressed for an arbitrary flow property as follows:

$$\widetilde{\Phi} = \frac{\overline{\rho \Phi}}{\bar{\rho}} \tag{3.50}$$

Now, the flow property is separated into a filtered term $\widetilde{\Phi}(x_i,t)$ and a subgrid term $\Phi''(x_i,t)$:

$$\Phi(x_i,t) = \widetilde{\Phi}(x_i,t) + \Phi''(x_i,t) \tag{3.51}$$

Accordingly, in context of LES the following assumptions are adopted:

$$\widetilde{\frac{\partial\widetilde{\Phi}}{\partial x_i}} = \frac{\partial\widetilde{\Phi}}{\partial x_i} \quad \text{and} \quad \widetilde{\mu\frac{\partial\widetilde{\Phi}}{\partial x_i}} = \bar{\mu}\frac{\partial\widetilde{\Phi}}{\partial x_i} \tag{3.52}$$

3.3.3.2 Filtered governing equations

Applying filtering Eq. (3.49) and Favre-averaging Eq. (3.50) to the governing equations one obtains

Conversation of mass:

$$\frac{\partial\bar{\rho}}{\partial t} + \frac{\partial(\bar{\rho}\widetilde{u}_j)}{\partial x_j} = \overline{\dot{\rho}^s} \tag{3.53}$$

Conversation of momentum:

$$\frac{\partial(\bar{\rho}\widetilde{u}_i)}{\partial t} + \frac{\partial(\bar{\rho}\widetilde{u_i u_j})}{\partial x_j} = -\frac{\partial\bar{p}}{\partial x_i} + \frac{\partial\overline{\tau}_{ij}}{\partial x_j} + \bar{\rho}g_i + \bar{\rho}f_i^s \tag{3.54}$$

where the filtered viscous stress tensor $\overline{\tau}_{ij}$ is given as follows:

$$\overline{\tau}_{ij} = \bar{\mu}\left(\frac{\partial\widetilde{u}_i}{\partial x_j} + \frac{\partial\widetilde{u}_j}{\partial x_i}\right) - \frac{2}{3}\bar{\mu}\frac{\partial\widetilde{u}_k}{\partial x_k}\delta_{ij} \tag{3.55}$$

Conversation of energy:

$$\frac{\partial(\overline{\rho}\widetilde{e})}{\partial t} + \frac{\partial(\overline{\rho}\widetilde{eu_j})}{\partial x_j} = -\widetilde{p\frac{\partial u_j}{\partial x_j}} + \widetilde{\tau_{ij}\frac{\partial u_i}{\partial x_j}} + \frac{\partial}{\partial x_j}\left[\frac{c_p\bar{\mu}}{Pr}\frac{\partial\widetilde{T}}{\partial x_j}\right] + \bar{\dot{\omega}}_{\text{heat}} + \bar{\dot{\omega}}^{\text{s}} \tag{3.56}$$

Species transport:

$$\frac{\partial}{\partial t}\left(\bar{\rho}\widetilde{Y_m}\right) + \frac{\partial}{\partial x_j}\left(\bar{\rho}\widetilde{Y_m u_j}\right) = \frac{\partial}{\partial x_j}\left[\frac{\bar{\mu}}{Sc}\frac{\partial\widetilde{Y_m}}{\partial x_j}\right] + \bar{\dot{\omega}}_{\text{m}} \tag{3.57}$$

Equation of state:

$$\bar{p} = \frac{\bar{\rho}R\widetilde{T}}{W} \tag{3.58}$$

3.3.3.3 Modeling of the subgrid scale

In above given filtered equations Eq. (3.53)-(3.57) closure problems occur. First of all, in the filtered energy equation (see Eq. (3.56)) there are two nonlinear unclosed terms being $-\widetilde{p\frac{\partial u_j}{\partial x_j}}$ and $\widetilde{\tau_{ij}\frac{\partial u_i}{\partial x_j}}$. In [87] and [95] it was pointed out that at low-Mach-numbers the contributions of pressure dilatation and the subgrid viscous distribution to the subgrid thermal flux are negligible. Accordingly in this work, these terms are simplified as follows:

$$-\widetilde{p\frac{\partial u_j}{\partial x_j}} = \widetilde{p}\frac{\partial \widetilde{u}_j}{\partial x_j} \quad \text{and} \quad \widetilde{\tau_{ij}\frac{\partial u_i}{\partial x_j}} = \overline{\tau}_{ij}\frac{\partial \widetilde{u}_i}{\partial x_j} \tag{3.59}$$

However in filtered momentum equation (Eq. (3.54)), energy transport equation (Eq. (3.56)) and species equations (Eq. (3.57)) there are other unclosed terms being $\widetilde{u_i u_j}$, $\widetilde{eu_j}$, $\widetilde{Y_m u_j}$. These terms can be separated into a resolved term and subgrid term

$$\begin{aligned} \widetilde{u_i u_j} &= \widetilde{u}_i\widetilde{u}_j + \tau_{ij}^{sgs} \\ \widetilde{eu_j} &= \widetilde{e}\widetilde{u}_j + \tau_{e}^{sgs} \\ \widetilde{Y_m u_j} &= \widetilde{Y}_m\widetilde{u}_j + \tau_{Y_m}^{sgs} \end{aligned} \tag{3.60}$$

In LES context, the subgrid term τ_{ij}^{sgs} is modelled, since it cannot be resolved. Accordingly, in this work, the modelling method of τ_{ij}^{sgs} is based on Boussinesq's assumption:

$$\tau_{ij}^{sgs} - \frac{1}{3}\tau_{kk}^{sgs}\delta_{ij} = -2\nu_t\left(\widetilde{S}_{ij} - \frac{1}{3}\widetilde{S}_{kk}\delta_{ij}\right) \tag{3.61}$$

where $\tilde{S}$ is the filtered rate of strain tensor:

$$\widetilde{S}_{ij} = \frac{1}{2}\left(\frac{\partial \widetilde{u}_i}{\partial x_j} + \frac{\partial \widetilde{u}_j}{\partial x_i}\right) \tag{3.62}$$

In Eq. (3.61) ν_t is so-called kinematic turbulent viscosity or eddy viscosity. It can be formulated as a dynamic turbulent viscosity as $\mu_t = \rho\nu_t$.

The other unclosed terms, $\widetilde{eu_j}$ and $\widetilde{Y_m u_j}$ are modelled using a simple gradient based assumption:

$$\begin{aligned} \tau_{e}^{sgs} &= -\frac{\nu_t}{Pr_t}\frac{\partial \widetilde{e}}{\partial x_j} \\ \tau_{Y_m}^{sgs} &= -\frac{\nu_t}{Sc_t}\frac{\partial \widetilde{Y_m}}{\partial x_j} \end{aligned} \tag{3.63}$$

where Sc_t and Pr_t are the turbulent Schmidt and Prandtl numbers. In this work they are considered as follows: $Sc = Sc_t = Pr = Pr_t = 0.7$

Setting the equations (3.60) (3.61) and (3.63) in the corresponding filtered equations above (Eqs. (3.54), (3.56) and (3.57)) the following equations for LES modelling are obtained:

$$\frac{\partial\left(\bar{\rho}\widetilde{u}_i\right)}{\partial t}+\frac{\partial\left(\bar{\rho}\widetilde{u}_i\widetilde{u}_j\right)}{\partial x_j}=-\frac{\partial\bar{P}}{\partial x_i}+\frac{\partial}{\partial x_j}\left[\left(\bar{\mu}+\mu_t\right)\left(\frac{\partial\widetilde{u}_i}{\partial\widetilde{x}_j}+\frac{\partial\widetilde{u}_j}{\partial\widetilde{x}_i}-\frac{2}{3}\frac{\partial\widetilde{u}_k}{\partial\widetilde{x}_k}\delta_{ij}\right)\right]+\bar{\rho}g_i+\bar{\rho}f_i^s \quad (3.64)$$

where pressure term $\bar{P}$ involves unknown term arises from momentum flux, namely the isotropic subgrid stress tensor $\bar{P}=\bar{p}+\frac{1}{3}\tau_{kk}^{sgs}$. The isotropic part τ_{kk}^{sgs} is still unknown and it is kept in $\bar{P}$ as a general rule. For energy and species transport equations Eqs. (3.65) and (3.66) in following it is assumed that $\bar{P}\approx\bar{p}$ and instead of $\bar{P}$, $\bar{p}$ arises in these equations.

$$\frac{\partial(\overline{\rho}\widetilde{e})}{\partial t}+\frac{\partial(\overline{\rho}\widetilde{e}\widetilde{u}_j)}{\partial x_j}=-\overline{p}\frac{\partial\widetilde{u}_j}{\partial x_j}+\bar{\tau}_{ij}\frac{\partial\widetilde{u}_i}{\partial x_j}+\frac{\partial}{\partial x_j}\left[\frac{\left(\bar{\mu}+\frac{c_v}{c_p}\mu_t\right)c_p}{Pr}\frac{\partial\widetilde{T}}{\partial x_j}\right]+\bar{\dot{\omega}}_{\mathrm{heat}}+\bar{\dot{\omega}}^{\mathrm{s}} \quad (3.65)$$

$$\frac{\partial}{\partial t}\left(\bar{\rho}\widetilde{Y_m}\right)+\frac{\partial}{\partial x_j}\left(\bar{\rho}\widetilde{u}_j\widetilde{Y_m}\right)=\frac{\partial}{\partial x_j}\left[\frac{(\bar{\mu}+\mu_t)}{Sc}\frac{\partial\widetilde{Y_m}}{\partial x_j}\right]+\bar{\dot{\omega}}_{\mathrm{m}} \quad (3.66)$$

The finally the turbulent viscosity μ_t is to be determined. In this work for that purpose, the simplest but most of the time quite accurate eddy viscosity model, Smagorinsky model [108] is used.

Smagorinsky model

This model is a widely used turbulence model where the turbulence viscosity is defined as follows:

$$\mu_t=\bar{\rho}\left(C_s\Delta\right)^2\left|\widetilde{S}_{ij}\right| \quad (3.67)$$

where C_s is the Smagorinsky constant which can vary for different configurations. In this work Smagorinsky constant is taken as $C_s=0.1$. Δ is the filter width which is obtained by the grid volume V_{volume} as follows:

$$\Delta=V_{volume}^{\frac{1}{3}} \quad (3.68)$$

Within this model, the eddy viscosity μ_t is modelled by analogy to the mixing-length hypothesis where the eddy viscosity is proportional to a characteristic length scale ℓ_m. More information about mixing-length hypothesis is to be found in [98]. The filter width Δ and the Smagorinsky C_s constant in Eq. (3.68) can be considered as the characteristic mixing length scale. In the Eq. (3.67) the term $\left|\widetilde{S}_{ij}\right|$ is defined as:

$$\left|\widetilde{S}_{ij}\right|=\sqrt{2\widetilde{S}_{ij}\widetilde{S}_{ij}} \quad (3.69)$$

where $\widetilde{S}_{ij}$ is the resolved strain rate tensor as defined already in Eq. (3.62).

Chapter 4

Numerical modeling of auto-ignition in a CAI

This chapter is divided in five sections. The first and second section provide a basic knowledge about thermodynamics of combustion processes and chemical kinetics, respectively. The third section is devoted to general description of ignition processes. In the fourth section, auto-ignition model employed in this work is presented in details. Finally in the fifth section the coupling of combustion model and the CFD code is explained. In this chapter results from the auto-ignition model and detailed chemistry are presented. These results are delivered by Dr. -Ing. Marc-Sebastian Benzinger and Dr. -Ing. Robert Schießl from the Institute of Technical Thermodynamics (ITT), Karlsruhe Institute of Technology.

4.1 Thermodynamics of combustion processes

According to first law of thermodynamics, the change of internal energy (dE) of a system is equal to the sum of the heat Q transferred and the work W done to the system. Considering heat transfer only, for the chemical processes take place at constant volume the change in internal energy is

$$dE = \delta Q \text{ for } V = \text{ constant} \tag{4.1}$$

For chemical processes take place at constant pressure, enthalpy H is used instead of internal energy and the change of enthalpy equals to the heat transfer to the system.

$$\mathrm{d}H = \delta Q \text{ for } p = \text{ constant} \tag{4.2}$$

A chemical reaction is the exchange and/or rearrangement of molecules. Combustion is an exothermic reaction which converts fuel and oxidizer into reaction products and provides heat. The heat provided by combustion is the change in internal energy or enthalpy depending on if the combustion takes place at constant volume or pressure. Based on the general description of a chemical reaction given in Eq. (4.3) the change of the reaction internal energy and enthalpy is given in Eq. (4.4)

$$\nu_A A + \nu_B B \ldots \rightarrow \nu_C C + \nu_D D \ldots \tag{4.3}$$

where $\nu_i (i = A, B..)$ are the stoichiometric coefficients.

$$\Delta_R E = \sum \nu_i E_i \text{ and } \Delta_R H = \sum \nu_i H_i \tag{4.4}$$

Since absolute values of E and U cannot be determined as given in Eq. (4.4), the reference enthalpies of each compound used, the so called *standard enthalpy of formation* which are available from measurements [124]. At every temperature the enthalpy is $H_T = H_{298} + \int_{298}^{T} C_p dT$. Analogously, the internal energy at every temperature can be determined. Hence, the enthalpy change for the reaction in Eq. 4.3 is described as $\Delta_R H = \sum \nu_i \Delta H_i$ which involves the reference formation enthalpies.

A thermodynamic process is called reversible if the process can go back to its initial state itself. For such processes the local equilibrium state is defined. On the contrary a system called irreversible (for example combustion), if it can only return to its initial conditions by changing its surroundings (e.g. adding work or heat). If a system is reversible (denoted as "rev.") or irreversible (denoted as "irrev.") can be defined with the second laws of thermodynamics using entropy S as given in Eq. (4.5). More information about entropy and its description can be found in [124] and [52].

$$\mathrm{d}S = \frac{\delta Q_{rev.}}{T} \text{ and } \mathrm{d}S \geq \frac{\delta Q_{irrev.}}{T} \tag{4.5}$$

Accordingly, change in entropy during a reversible process is

$$S_1 - S_2 = \int_2^1 \frac{\delta Q_{rev.}}{T}. \tag{4.6}$$

According to the third law of thermodynamics for ideal crystals of pure compounds, it follows $\lim_{T \to 0} S = 0$. Using this information, the entropy of a reaction is defined as enthalpy of a reaction with measured standard entropies S^0. In case of reversible process where volume is constant, the change in entropy of system $\mathrm{d}S = \frac{C_V}{T}\mathrm{d}T = S_{298} + \int_{298K}^{T} \frac{C_v}{T} dT$ and in case of constant pressure $\mathrm{d}S = \frac{C_p}{T}\mathrm{d}T = S_{298} + \int_{298K}^{T} \frac{C_p}{T} dT$.

Using the relations obtained from laws of thermodynamics, an important criterion, the so-called "*equilibrium criterion*" can be defined. If the first and second law of thermodynamics are combined one gets the equilibrium condition:

$$\mathrm{d}(E - TS + pV) + V\mathrm{d}p + S\mathrm{d}T = 0 \tag{4.7}$$

where $G = H - TS$ is the free enthalpy (or Gibbs function) which is a formulation for chemical equilibrium $(\mathrm{d}G)_{p,T} = 0$. At this point, partial molar free enthalpy is defined as the *chemical potential* μ_i of a compound i in Eq. (4.8).

$$\mu_i = \left(\frac{\partial G}{\partial n_i}\right)_{p,T,n_j} \tag{4.8}$$

where n_j is the mole number. For a reacting ideal gas mixture in equilibrium combining Eq. (4.7) with (4.8) one obtains:

$$\sum_i \nu_i \mu_i^0 + RT \ln \prod_i \left(\frac{p_i}{p^0}\right)^{\nu_i} = 0 \tag{4.9}$$

From which equilibrium constants K_p and K_c are defined as

$$K_p = \prod_i \left(\frac{p_i}{p^0}\right)^{\nu_i} \quad \text{and} \quad K_c = \prod_i \left(\frac{c_i}{c^0}\right)^{\nu_i} \tag{4.10}$$

where c_i is the concentration of the specie i. These equilibrium constants can also be calculated from tabulated thermodyamical data (e.g. Janaf Table) as follows

$$K_p = \exp\left(\frac{-\Delta_R \bar{G}^0}{RT}\right) \quad K_c = \exp\left(\frac{-\Delta_R \bar{A}^0}{RT}\right) \tag{4.11}$$

where $\bar{G}^0$ and $\bar{A}^0$ are the standard molar free enthalpy and free energy ($A = G - pV$) respectively.

4.2 Chemical kinetics

Considering the general description of chemical reactions given in Eq. (4.3), the reaction rate r can be expressed as consumption of specie A

$$r_f = \frac{\mathrm{d}c_A}{\mathrm{d}t} = -k_f c_A^a c_B^b \ldots \tag{4.12}$$

Here $a, b, \ldots$ are reaction orders with respect to species A, B, ... They might be for some cases equal to the stoichiometric coefficients $\nu_i (i = A, B..)$ given in Eq. (4.3). However most of the time it is not the case and they are experimentally decided. c_A and c_B stand for the concentration of the molecules A and B. Here k_f is the rate coefficient of the forward reaction. For the reverse reaction of Eq.(4.3) one obtains:

$$r_r = \frac{\mathrm{d}c_A}{\mathrm{d}t} = k_r c_D^d c_E^e \ldots \tag{4.13}$$

where c_D and c_E are the concentration of the molecules D and E. In Eq. (4.13) k_r is the rate coefficient of the backward reaction. At chemical equilibrium the forward and backward reactions have same rate on microscopic level, i.e. and on macroscopic level reaction cannot be observed.

$$\begin{gathered} k_f c_A^a c_B^b \ldots = k_r c_D^d c_E^e \ldots \\ \frac{k_f}{k_r} = \frac{c_A^a c_B^b \cdots}{c_D^d c_E^e \ldots} \end{gathered} \tag{4.14}$$

From the relation given in Eq. (4.11) the relation between reaction rates of backward and forward reactions can be deduced from thermodynamic data using the following relation

$$K_c = \frac{k_f}{k_r} = \exp\left(\frac{-\Delta_R \bar{A}^0}{RT}\right) \tag{4.15}$$

The temperature dependency of reaction rate coefficients $k_{f,r}$ is strongly nonlinear. According to Arrhenius law this dependency is formulated as given in Eq. (4.16)

$$k_{f,r} = A_e T^b \exp\left(-\frac{E_a}{RT}\right) \tag{4.16}$$

where E_a is the energy to overcome so called *activation energy* and $A_e T^b$ is the pre-exponential term which has different physical meaning for uni-, bi- and trimolecular reactions. For further information reader is referred to [124, 52].

An *elementary reaction* occurs on a molecular level exactly in a way which is described by the reaction equation [124]. Considering iso-octane oxidation given in Eq. (4.17), this is a global reaction and it is not an elementary reaction.

$$\mathrm{C_8H_{18}} + \frac{25}{2}\mathrm{O_2} \rightarrow 8\mathrm{CO_2} + 9\mathrm{H_2O} \tag{4.17}$$

The whole oxidation of iso-octane is an ensemble of numerous elementary reactions. Several molecules occur, rearrange and they broke into smaller molecules, single atoms and radicals. These elementary reactions are to be considered for realistic description of reaction kinetics. Example elementary reactions during the oxidation of iso-octane are given in Eq. (4.18) from [50].

$$\begin{gathered} \mathrm{OOC_8H_{16}OOH} \rightarrow \mathrm{OC_8H_{15}OOH} + \mathrm{OH} \\ \mathrm{C_8H_{18}} + \mathrm{OH} \rightarrow \mathrm{C_8H_{17}} + \mathrm{H_2O} \\ \mathrm{C_2H_3} + \mathrm{HCO} \rightarrow \mathrm{C_2H_4} + \mathrm{CO} \end{gathered} \tag{4.18}$$

One can see from Eq. (4.18) that additional species occur during the oxidation of iso-octane such as carbon monoxide (CO). For example, this knowledge is important to understand the emission formation during iso-octane combustion and could not be explained only with the global reaction definition as given in Eq. (4.17).

For a reaction mechanism consisting of N_r elementary reactions and N_s species, a more general form for a reaction equation can be written

$$\sum_{k=1}^{N_s} \nu_{k,j}^f \mathcal{X}_k \rightleftharpoons \sum_{k=1}^{N_s} \nu_{k,j}^b \mathcal{X}_k \text{ with } j = 1, \ldots, N_r \tag{4.19}$$

where $\nu_{k,j}^f$, $\nu_{k,j}^b$ and $\mathcal{X}_k$ denote the stoichiometric coefficients of the reactants and products and symbol of the species k respectively. Accordingly the reaction rate r_j can be generalized as in Eq. (4.20).

$$r_j = k_{f,j} \prod_{k=1}^{N_s} c_k^{\nu_{k,j}^f} - k_{f,j} \prod_{k=1}^{N_s} c_k^{\nu_{k,j}^b} \text{ with } j = 1, \ldots, N_r \tag{4.20}$$

Note that in Eq. (4.20) the reaction rate is expressed with the molar concentration c_k of species k and c_k defined as follows:

$$c_k = \frac{\rho Y_m}{W_m} \tag{4.21}$$

Accordingly, the source term of the species transport $\dot{\omega}_\mathrm{m}$ in Eq. (3.10) can be obtained by summing up the contributions from the elementary reactions

$$\dot{\omega}_\mathrm{m} = W_m \sum_{j=1}^{N_r} \left(\nu_{k,j}^f - \nu_{k,j}^b \right) r_j \tag{4.22}$$

Radical chain reactions

Considering auto-ignition concept within HCCI, PCCI and RCCI engines (see section 2.4), radical chain reactions have an immense importance during early stages of the combustion processes in CAI engines. For better understanding and description of ignition physics knowledge of the radical chain reactions is the key. Therefore, the concept of radical chain reactions will be outlined very briefly.

The radical chain reactions form the basis of combustion process and have three main steps [124]. These steps are chain initiation step, chain branching (or propagating) step and chain termination step. First, within the chain initiation step, radicals are formed from stable species. In chain branching (or propagation) step, these radicals react with other species stable forming new radicals. In the last step chain termination step the radicals are quenched by reaction pathways (e.g. vessel surface) that do not generate new radicals and/or they react to stable species.

4.3 Ignition process

Ignition is time-dependent process of starting with reactants and evolving in time until a steadily burning flame is developed or the system is totally burnt [124]. If fuel and oxidizer mix in a hot vessel, an explosion is observed after a certain time, so called *ignition delay time*. The ignition delay depends on the conditions of the system: Temperature, pressure and composition. Hence, for sake of safety in engine applications it is very important to know at which conditions and how the ignition would proceed.

The ignition limits are illustrated with *p-T explosion diagrams*. In [120] one can find ignition limits in hydrogen-oxygen system and for hydrocarbons more complicated $p - T$ explosion diagram is illustrated in [123]. This $p - T$ explosion diagram (ignition limits) for hydrocarbons is shown in Figure 4.1. Accordingly, at low temperatures and pressures no ignition is observed because radicals, which are formed in the gas phase by chemical

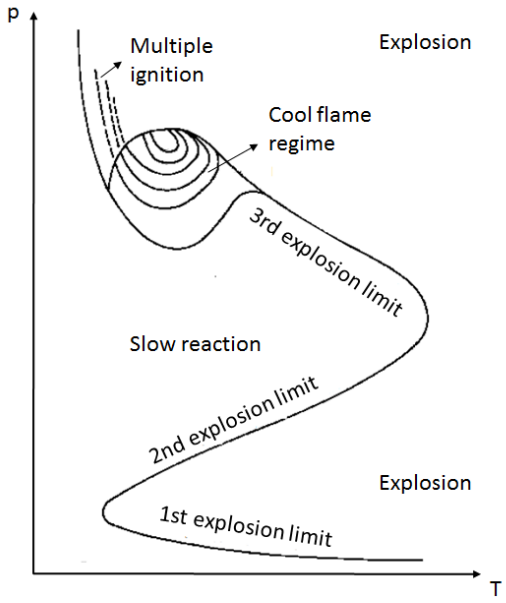

Figure 4.1: Schematic illustration of $p-T$ explosion diagram (ignition limits) for hydrocarbons [124, 123].

reactions, diffuse to the vessel wall where they recombine to stable species (radical chain termination). At low pressures the diffusion is very fast and as a result ignition does not take place. If the pressure is increased above *first ignition limit*, the diffusion rate of radicals to the wall is less than radical production rate in the gas phase, which leads to a spontaneous ignition. Increasing the pressure above *second ignition limit* again an ignition is observed. The second explosion limit is governed by the competition of chain branching and chain termination. At even higher pressures explosion limit exist and this limit is governed by the competition of heat relase from the reactions and heat losses through the vessel wall. The heat production per volume increases with increasing pressure that the mixture must explode (transition to explosion range)[124, 123]. From this studies and explanations one can see that ignition is a strongly nonlinear and complicated process. Within radical branch reactions it is decided how the ignition would proceed further.

4.4 Modeling auto-ignition in CAI engines

In CAI engines the combustion timing is controlled by the chemical kinetics (auto-ignition) and highly depends on the properties of the mixture field [126, 63, 64, 7, 13, 31, 43] (see also section 2.4). Inhomogeneities in the mixture and temperature field designate the combustion characteristics of CAI [126, 63].

With regard to a more accurate prediction of situations that intrinsically depend on temporal and spatial variations associated with turbulence, realistic simulations of CAI requires LES where the large scale motions are explicitly resolved to accurately predict the conditions prior to ignition. In particular those are the mixing of the injected fuel with the air, the *EGR* distribution within in the cylinder and the thermal conditions associated with them.

The previous section 4.3 lays emphasis on the fact that even in simple configurations (hot vessel, shock tubes) ignition mechanism is strongly nonlinear and complicated. Its prediction requires a detailed description of the reaction mechanism. Thus, for simulation of very complex applications such as, CAI engines, the prediction of auto-ignition process requires beside LES an accurate description of the chemistry within the whole range of thermodynamic conditions given by thermal and composition inhomogeneities.

Ideally, detailed chemistry could be used for the LES of CAI engines. This is possible, however it is computationally extremely expensive. The mathematical model for gas-phase chemical reaction systems consists of a set of partial differential equations, namely the conservation equations, which describe the time-dependent development of all the properties that determine the state of the system (pressure, enthalpy, species mass fractions). Many elementary reactions involved in a given chemical reaction system have greatly different time scales and this has severe consequences for the numerical solution of this differential equations system. This has led many researchers to develop reduction techniques for the chemistry. Some of these techniques which are relevant for this work can be summarized as follows:

- Quasi steady-state approximation (QSSA): If the consumption rate of a chemical specie is approximately equal to its rate of formation, one can assume that the concentration of this specie remains constant with time and therefore this specie can be neglected (removed from the mechanism). Using this assumption, QSSA reduces the full mechanism on the basis of certain rapidly equilibrating species [124, 78].

- Partial equilibrium assumption (PEA): This approach reduces the full mechanism on the basis of reactions. In a given mechanism forward and backward reactions of some certain elementary reactions are so fast that one obtains partial equilibria. These reactions in partial equilibria can be eliminated from the mechanism which leads to a decrease in the amount of differential equations to be solved [124, 78].

- Computational singular perturbation (CSP): This method is an iterative method to reduce the dimensionality of systems of ordinary differential equations (ODE) with multiple time scales and it is based on the eigenvalue analysis of the given chemical reaction system. The eigenvalues of the Jacobians of a the ODE-system reflect the time scales (i.e. reaction rates). For instance, the negative eigenvalue with the largest magnitude corresponds to the rate at which quasi-steady-state or partial equilibrium is achieved and the ratio between the largest and smallest (magnitude) negative eigenvalues of Jacobian describes the *degree of stiffness* of a reaction mechanism [124]. Using CSP approach the stiffness of the given ODE-system is reduced and the ODE system can be solved with larger time steps [124, 59, 60, 6].

- Intrinsic low-dimensional manifold (ILDM): This method is also based on the eigenvalue analysis of the Jacobians of a given ODE-system. Basically, the method decouples fast chemical processes from the slow ones and thus globally reduces the dimension of the composition space of the chemical system [72, 70].

- Flame prolongation of ILDM (FPI): The ILDM is not an appropriate approach to describe the low-temperature domain, since the dimension and therefore the complexity of the databases increase tremendously in this zone. Therefore the ILDM method is extended by Giquel et al in [36] to solve the problem at low temperatures. The extended version of ILDM is so-called flame prolongation of ILDM (FPI).

- Flamelet generated manifold (FGM): This method is based on the flamelet approach which covers a regime in turbulent combustion where chemistry is sufficiently fast such that it occurs in one-dimensional laminar flame structures - flamelets - embedded within the turbulent flow field [91, 93]. The FGM method tabulates thermochemical variables originating from these flamelets which is a combination of classic flamelet- and manifold methods. [91, 93, 84, 83]. This method is very similar to FPI method. CSP and ILDM are based on the idea that if all transport processes are neglected, a time-scale analysis can be performed and the fastest time scales are assumed to be in steady-state. The advantage of FGM and FPI against CSP and ILDM is that they take transport effects into account [85]

- Reaction-diffusion manifold (REDIM): This approach is the extension of ILDM by including diffusion terms but with a pre-defined spatial gradient [19, 20, 69].

- Progress-variable model (PVM) : The method uses detailed chemistry mechanism to create reaction trajectories. The dynamic of these reaction trajectories are then extracted with a progress variable [44, 58, 15]. This approach is the reduced model which is employed in this work. The details of the model and its application to the investigated CAI engine will be presented in following sections.

In this work *Progress Variable Approach* is employed which uses detailed reaction mechanism [12] for oxidation of Toluene Reference Fuel (TRF). This mechanism accounts for 137 species and 633 reactions. In following sections firstly, simplified model will be outlined. Secondly, details on the expansion of the simplified model for a CAI engine relevant conditions (high inhomogeneities in composition and temperature field, high amount of EGR) will be given. Finally, the tabulation approach and its coupling to the LES code will be outlined. Simple test cases to verify the coupling of tabulated chemistry approach with the LES Code are presented later in chapter 6.

4.4.1 Model structure

The employed model is based on the detailed chemistry simulations of homogeneous, adiabatic, isobaric reaction systems and it extracts the information on dynamics of these reactions. For a given fuel (in our case *TRF*)/oxidizer combination, by varying mixture fraction (Z), specific enthalpy (h) and pressure (p) these homogeneous reactor simulations represent a set of trajectories. Each trajectory is a function of Z, h and p and has its own ignition process/history. For relevant ranges of Z, h and p created trajectories are then combined to a manifold in space state. This approach namely, *Trajectory Generated Low-Dimensional Manifold (TGLDM)* was introduced in 1993 by

Pope and Maas in [99].

In case of flame propagation combustion, e.g., in SI engines, the reaction system is strongly coupled with the transport process due to strong gradients between burnt and unburnt gas. For such cases the flamelet concept [92, 91, 93] is appropriate and in engine applications Flamelet Generated Manifolds (FGM) (similar fashion to (TGLDM)) [83] can be employed as in the work of He et al. [39].

On the other hand, although in a CAI engine considerable scalar *fluctuations* can be present before ignition, still auto-ignition is dominated with the reaction kinetics. Because typically the gradients at this phase of the engine cycle are not strong enough to create a notable coupling of reaction and transport. This phenomenon will be presented and discussed later in section 4.5.1 with an engine relevant test case for systems with diffusion.

However the model is valid until ignition. After ignition where flame starts to propagate, a strong coupling of reaction and transport processes exist. Therefore, after ignition depending on the engine configuration (speed, air-fuel ratio), a flamelet-type model affords a more appropriate description of the system.

This work focuses only on auto-ignition process in a CAI engine and therefore a simple manifold based on reaction without coupling to transport (diffusive and convective) is employed.

4.4.2 Trajectory generation

One can define the thermo-chemical state of a system with specific enthalpy (h), pressure (p) and species mass fraction Y_i assembled in a vector as follows:

$$\mathbf{\Psi} = (h, p, Y_1, ..Y_{N_s}) \tag{4.23}$$

where N_s refers to the number of species. The temporal change of the thermo-chemical state of a reaction system is defined generally with a conservation equation as follows:

$$\frac{\partial \mathbf{\Psi}}{\partial t} = \frac{1}{\rho}\nabla \cdot \left(D \frac{\partial \mathbf{\Psi}}{\partial \mathbf{x}} \right) - \mathbf{u}\frac{\partial \mathbf{\Psi}}{\partial \mathbf{x}} + \dot{\omega}_{\mathbf{\Psi}} \text{ with } \mathbf{u} = \begin{pmatrix} u_i \\ u_j \\ u_k \end{pmatrix} \text{ and } \mathbf{x} = \begin{pmatrix} x_i \\ x_j \\ x_k \end{pmatrix} \tag{4.24}$$

The first, second and third terms on the right hand of the Eq. (4.24) refer to the changes in a system due to diffusion, convection and chemical source term respectively. Considering a reaction occurs in a spatially homogeneous (no diffusion) reactor without any transport phenomena, the general form of Eq. (4.24) reduces to Eq. (4.25).

$$\frac{\partial \mathbf{\Psi}}{\partial t} = \dot{\omega}_{\Psi} \tag{4.25}$$

where, $\dot{\omega}_{\Psi}$ is the general denotation of the source term due to chemical reaction. Finally, the ordinary differential equations (ODEs) representing the temporal change of the

thermo-chemical state of the homogeneous, adiabatic, isobaric system are as given in Eqs. (4.26), (4.27)) and (4.28):

$$\frac{\mathrm{d}h}{\mathrm{d}t} = 0 \tag{4.26}$$

$$\frac{\mathrm{d}p}{\mathrm{d}t} = 0 \tag{4.27}$$

$$\frac{\mathrm{d}Y_i}{\mathrm{d}t} = \frac{W_i \dot{\omega}_i}{\rho} \tag{4.28}$$

where $\dot{\omega}_i$ is the molar formation rate of species i (cf. Eqs. (4.21) and (4.22)). These equations below are not LES-filtered, they are here given to describe the system. The relevant filtered equations for combustion modelling are given later in section 4.5.

Reaction trajectories of isenthalpic, isobaric reactors were computed using a detailed chemistry scheme according to a reaction mechanism for Toluene Reference Fuels (TRF)[12] (i.e. $N_s = 137$ in Eq. (4.23)). Each trajectory computation starts with an initial condition $\mathbf{\Psi}_0$, which is parameterized by unburnt temperature T_u instead of specific enthalpy, pressure p, mixture fraction Z and exhaust gas ratio EGR.

The definition used for EGR is given in Eq. (4.29). This is the same conventional EGR definition used during the experimental study of the investigated CAI engine.

$$EGR = \frac{m_\mathrm{exhaust}}{m_\mathrm{exhaust} + m_\mathrm{fresh}} \tag{4.29}$$

where m_exhaust and m_fresh are the masses of exhaust gas and fresh air-fuel mixture respectively.

The initial composition $(Y_{i,0})$, $i = 1, \ldots, N_s$ depends on Z and EGR as follows:

$$Y_{i,\mathrm{u}} = EGR\, Y_{i,\mathrm{exh.}} + (1 - EGR)\,(Z\, Y_{i,\mathrm{fuel}} + (1 - Z) Y_{i,\mathrm{air}}) \tag{4.30}$$

Here, $Y_{i,\mathrm{fuel}}$ and $Y_{i,\mathrm{air}}$ are the mass fraction vectors for pure fuel and air, respectively. $Y_{i,\mathrm{exh.}}$ is the mass fraction vector for exhaust gas, where the species' mass fractions are taken from chemical equilibrium (burnt) of a fresh gas mixture with a fixed Z at unburnt temperature (T_u) and pressure. The fixed Z of exhaust gas has a value of 0.0490 (or most commonly used by engine researchers $\lambda = 1.3$) for all reaction trajectories. This value is the averaged mixture fraction of the investigated CAI engine when the valves are closed and it is delivered by the experimentalists. More details about the experimental configuration of the particular CAI engine will be given in section 7.1. The unburnt temperature of the mixture from which the exhaust gas is obtained, has the same magnitude as, the unburnt temperature of the pure air and fuel. More details about the EGR concept employed in this work will be given in section 4.4.4.

Now knowing the initial thermo-chemical state vector $\mathbf{\Psi}_0 = (Z, T_\mathrm{u}, p, EGR)$ a reaction trajectory can be calculated by solving the system of ordinary differential equations (ODE) for isenthalpic $(\Delta h = 0)$, isobaric $(\Delta p = 0)$ homogeneous reactors as given in

Eqs. (4.26), (4.27) and (4.28). The numerical solution of these ODEs was performed by the code HOMREA [71, 14]. From these calculations one obtains reaction trajectories which are function of time and initial condition vector $\mathbf{\Psi}(t, \mathbf{\Psi}_0)$. By combining these trajectories with different initial conditions one obtains a manifold with five dimensions being Z, T_u, p, EGR and time t.

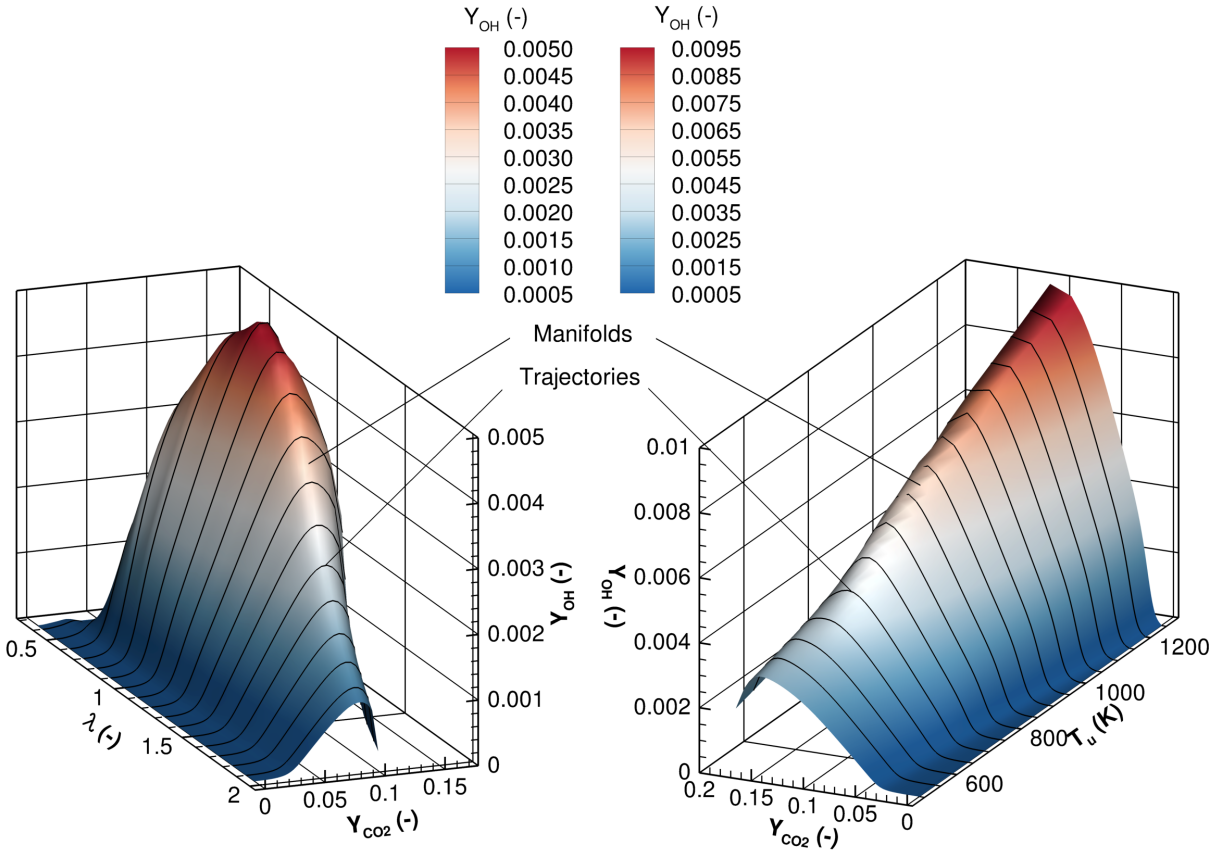

Figure 4.2: The manifold created by varying λ (left) and T_u (right) for fixed conditions: $T_\mathrm{u} = 730K$ (left) $\lambda = 1.04$ (Right) at $p = 15bar$, $0\%EGR$

The Figure 4.2 exemplary shows two manifolds created at different initial conditions. On the left side of the figure a two-dimensional cut-out from the five-dimensional manifold in state space for $T_\mathrm{u} = 730$ K, $p = 15$ bar, $EGR = 0\%$, with varying mixture fraction Z is plotted. Since engine researches use commonly λ to identify the mixing state, in all following figures of this work the mixing state will be presented with λ instead of mixture fraction Z. And on the right side of Figure 4.2 another two-dimensional cut-out is illustrated, this time by varying the independent variable T_u at $\lambda = 1.04$ $p = 15$ bar and EGR $= 0\%$. In both subfigures one can see the black lines which correspond to reaction trajectories and they are obtained by solving ODEs given in Eqs. (4.26), (4.27) and (4.28). Assembling these trajectories, one observes the manifold which is shown in Figure 4.2 with contour colours. In the figure, reaction trajectories (evolution of ignition) are presented as functions of carbon dioxide mass fraction Y_{CO_2} and hydroxide mass fraction Y_{OH}. One can see from these trajectories that they have their individual paths,

which depend on their initial conditions.

4.4.3 Choice of progress variable

As already mentioned above, solving the ODEs above (Eqs. (4.26), (4.27) and (4.28)) with a given initial state of a chemical reaction system $\mathbf{\Psi}_0 = \mathbf{\Psi}(t = 0)$, the temporal development of the thermo-chemical state of a homogeneous reactor $\mathbf{\Psi}(t, \mathbf{\Psi}_0)$ is computed, which represents reaction trajectories. Accordingly, the trajectory-generated manifold can be parametrized by $(\mathbf{\Psi}, t)$. However, for a reduced model it is better to use a variable that is related to the chemical state of the system for the parametrization of reaction progress.

A progress variable (PV) describes the position on a reaction trajectory and gives information about the state variables during the reaction. The trajectory-generated manifold can then be parametrized with a PV:

$$\mathbf{\Psi}(\mathbf{\Psi}, t) \rightarrow \mathbf{\Psi}(\mathbf{\Psi}, PV) \tag{4.31}$$

In general, the characteristics of an optimal progress variable can be listed as follows

- monotonically increasing values during the reaction
- positivity and boundedness so that the variable can be normalized ($PV = 0$ for unburnt mixture, $PV = 1$ for exhaust gas in chemical equilibrium)
- sensitivity to important stages of the chemical reaction such as pre-ignition reactions, ignition and combustion.

Studies on progress variable formulations have been performed in [45, 81, 101] which depend on the target combustion system as well as on initial and boundary conditions. Several progress variable definitions were tested to find out the most suitable progress variable for the auto-ignition process with the given detailed chemistry mechanism in [15]. Progress variables based on temperature or mass fractions of species such as $\mathrm{Y_{CO_2}}$, $\mathrm{Y_{CO}}$ and their linear combinations are not always monotonic if initial condition is changed. This will be illustrated later.

A straightforward progress variable definition is obtained by exploiting the second law of thermodynamics for a chemically reacting system. According to second law of thermodynamics during ignition and/or combustion process in a closed, adiabatic system entropy increases monotonically since the process is irreversible (see section 4.1). For ideal gases specific entropy is a reasonable and meaningful quantifier of main components, radicals and intermediate products which shows a good sensitivity to chemical activity of early phases of the ignition process. This guarantees that the entropy production (as it occurs by chemical reaction) is non-negative, and zero only at equilibrium. Hence, integrating the specific chemical entropy production rate $\dot{s}_{\mathrm{chem}}$ (i.e., the chemical source term of specific entropy, in J/(kg·K·s)) along a reaction trajectory will deliver a monotonic

variable.

During a chemical reaction produced specific entropy s_{chem} is derived from Gibbs equation for specific enthalpy h of a system (4.1):

$$\mathrm{d}h = T\mathrm{d}s + v\mathrm{d}p + \sum_{i=1}^{N} \frac{\mu_i}{M_i}\mathrm{d}Y_i \tag{4.32}$$

In Eq. (4.32) μ_i is the chemical potential of the species i. The chemical potential μ_i is defined in Eq. (4.33) where s_i^0 is specific entropy at standard pressure. More details to Gibbs equation and μ_i are already given in section 4.1.

$$\mu_i = M_i h_i - T\left(M_i s_i^0 - R\ln\frac{p_i}{p^0}\right) \tag{4.33}$$

The rate of entropy production $\dot{s}_{\text{chem}}$ can readily be computed from the chemical source term of the species mass fractions $\dot{Y}_{i,\text{chem}}$ as in [14]:

$$\dot{s}_{\text{chem}} = \sum_{i=1}^{n_s} \dot{Y}_{i,\text{chem}} s_i + \sum_{i=1}^{n_s} Y_i c_{p,i}\frac{\dot{T}}{T} - \sum_{i=1}^{n_s} \frac{Y_i \bar{R}}{M_i}\frac{\dot{p}_i}{p_i} \tag{4.34}$$

For illustration of the monotonic behaviour of specific entropy in Figure 4.3 (left) its temporal change $\dot{s}_{\text{chem}}$ for four different initial conditions $\mathbf{\Psi}_{0,1}$, $\mathbf{\Psi}_{0,2}$, $\mathbf{\Psi}_{0,3}$ and $\mathbf{\Psi}_{0,4}$ during homogeneous reactor are plotted. The initial conditions for these homogeneous reactor simulations are listed in Table 4.1. Here, the air/fuel ratio λ is used rather than mixture fraction Z, because λ is more commonly applied in engine research. The relation between Z and λ is given in Eq. (4.35).

$$Z = \frac{Z_{stoi}}{Z_{stoi} + \lambda\,(1 - Z_{stoi})} \tag{4.35}$$

where Z_{st} is the stoichiometric mixture fraction which has a value of $Z_{\text{st}} = 0.06289$ for TRF/air mixture [12].

Table 4.1: Initial conditions for homogeneous reactor simulations in Figure 4.3

$\mathbf{\Psi}_{0,i}$	λ	T_{u}(K)	p (bar)
$\mathbf{\Psi}_{0,1}$	0.995	833.3	12.59
$\mathbf{\Psi}_{0,2}$	0.995	909.1	19.95
$\mathbf{\Psi}_{0,3}$	1.799	930.0	22.4
$\mathbf{\Psi}_{0,4}$	1.599	1017.5	32.4

A normalized version of the produced entropy along a reaction trajectory can be computed by using Eq. (4.36) which can be employed as the actual progress variable. Diagram

on the right side of Figure 4.3 shows some examples for the temporal evolution of this progress variable.

$$PV(t) = \frac{\int_{t_0}^{t} \dot{s}_{\text{chem}}\left(\mathbf{\Psi}(t)\right) \mathrm{d}t}{\int_{t_0}^{t_\infty} \dot{s}_{\text{chem}}\left(\mathbf{\Psi}(t)\right) \mathrm{d}t} \tag{4.36}$$

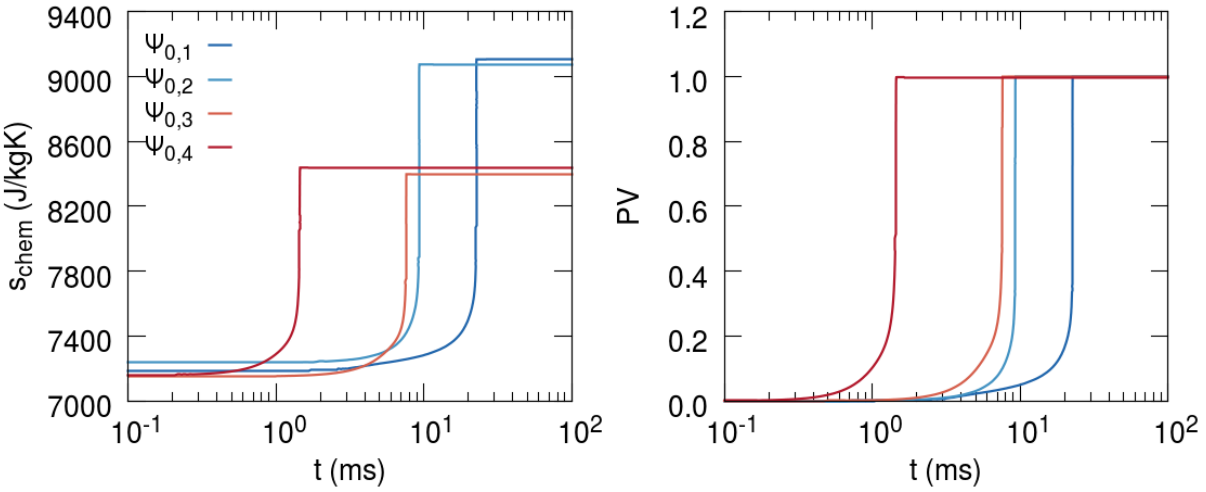

Figure 4.3: Temporal change of specific produced entropy (left) and normalized specific produced entropy (right) during auto-ignition in homogenous reactors for different initial conditions [128].

Benzinger [15] compared different PV definitions for homogeneous reactor simulation of a TRF/air mixture at $T_\text{u} = 750K, p = 10bar$ and $\lambda = 0.3$ in his work. To capture complex behaviour of auto-ignition process, in [15] also detailed mechanism of Andrea [12] is employed. In Figure 4.4 temporal development of different normalized progress variables are plotted namely, temperature (PV_T), CO_2 mass fraction (PV_{CO_2}), linear combination of CO_2 and CO mass fractions (PV_{CO_2+CO}) and specific entropy $PV_{s_{chem}}$. The figure shows that due to the low unburnt temperature and pressure condition, a two-stage ignition occurs and this phenomenon could be only represented accurately by temperature and specific entropy. Evaluating these results by means of monotonic behaviour, both temperature and CO_2 mass fraction show non-monotonous behaviour, while specific entropy and the linear combination of CO_2 and CO mass fractions increase monotonically. To sum up, only specific entropy represents the complex two-stage ignition behaviour of the TRF/air mixture at given conditions and at the same time shows a monotonic temporal progress.

In this work, specific entropy is employed in this work as the progress variable. In order to denote the normalized specific entropy in Eq. (4.36), simply PV will be used.

4.4.4 Tabulation

Beside the chemical source term of the progress variable $\dot{\omega}_\text{PV}$ and the rate of chemical "heat-release" $\dot{\omega}_\text{heat}$, as well as material properties like the mixture's heat capacity c_p,

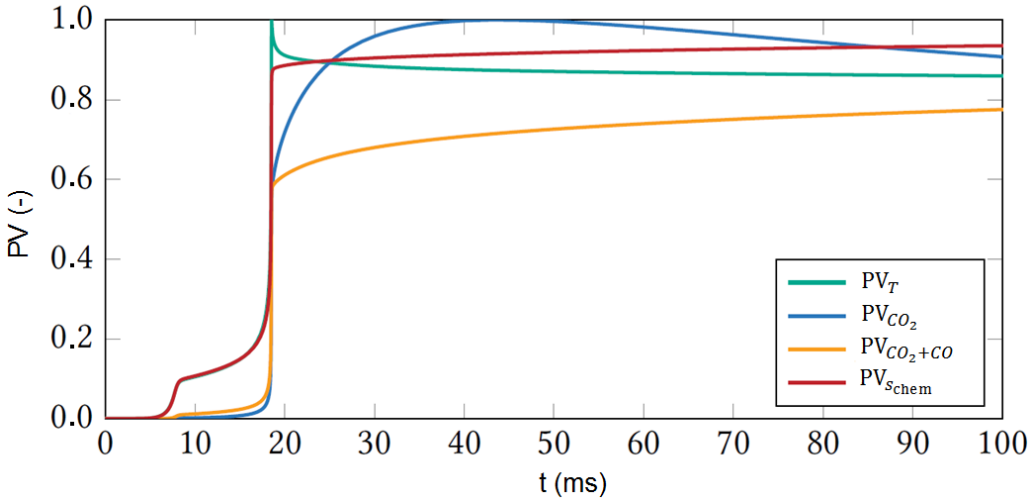

Figure 4.4: Comparison of different PV defintions during a homogenous reactor simulation of TRF/air mixture at $T_u = 750K, p = 10bar$ and $\lambda = 0.3$ [15].

viscosity μ and mean molar mass $\overline{W}$ are pre-tabulated in dependence of progress variable, mixture fraction, unburned temperature, pressure and EGR.

It is important to explain the necessity of the extension of look-up table with EGR. As already mentioned in section 2.4 CAI engines work commonly with high EGR rates which can reach to high amounts such as $65 - 70\%$ EGR. Without any doubt, such an amount of EGR has immense influence on the characteristics of auto-ignition processes. To show how EGR effects auto-ignition processes quantitatively, results from two homogeneous reactor simulations for $Z = 0.03595$, $p = 22.4$bar, $T_u = 930$K with different EGR 0% and 65% are compared in Figure 4.5. This comparison is done by means of temporal evolution of temperature T, progress variable PV and source terms for heat release $\dot{\omega}_{\text{heat}}$ and chemical reaction $\dot{\omega}_{\text{PV}}$.

From Figure 4.5 one can deduce that high EGR, can have an immense influence on auto-ignition characteristics by delaying auto-ignition and decreasing the source term of heat release $\dot{\omega}_{\text{heat}}$, resulting in significantly lower burned gas temperatures. From $0\%EGR$ to $65\%EGR$: The equilibrium temperature difference is 750K and the ignition delay increases almost by an factor 5. And the maximum values of $\dot{\omega}_{\text{heat}}$ and $\dot{\omega}_{\text{PV}}$ decrease with factors almost 480 and 263 respectively. This enormous effect of EGR on auto-ignition processes put an emphasis on the importance of including EGR as an additional independent variable in the tabulation; thus, the initial condition vector for the pre-tabulation homogeneous reactor calculations $\mathbf{\Psi}_0=(Z, p, T_u)$ was extended with EGR (%) $\mathbf{\Psi}_0=(Z, p, T_u, EGR)$.

The EGR concept used for the tabulation of the chemistry is represented schematically in Figure 4.6. Firstly, an engine relevant unburnt temperature T_u and pressure p_0 is chosen. After that, exhaust gas is prepared to be mixed with a fresh air/fuel mixture. The exhaust gas (burned gas) is obtained by homogeneous reactor simulations at given

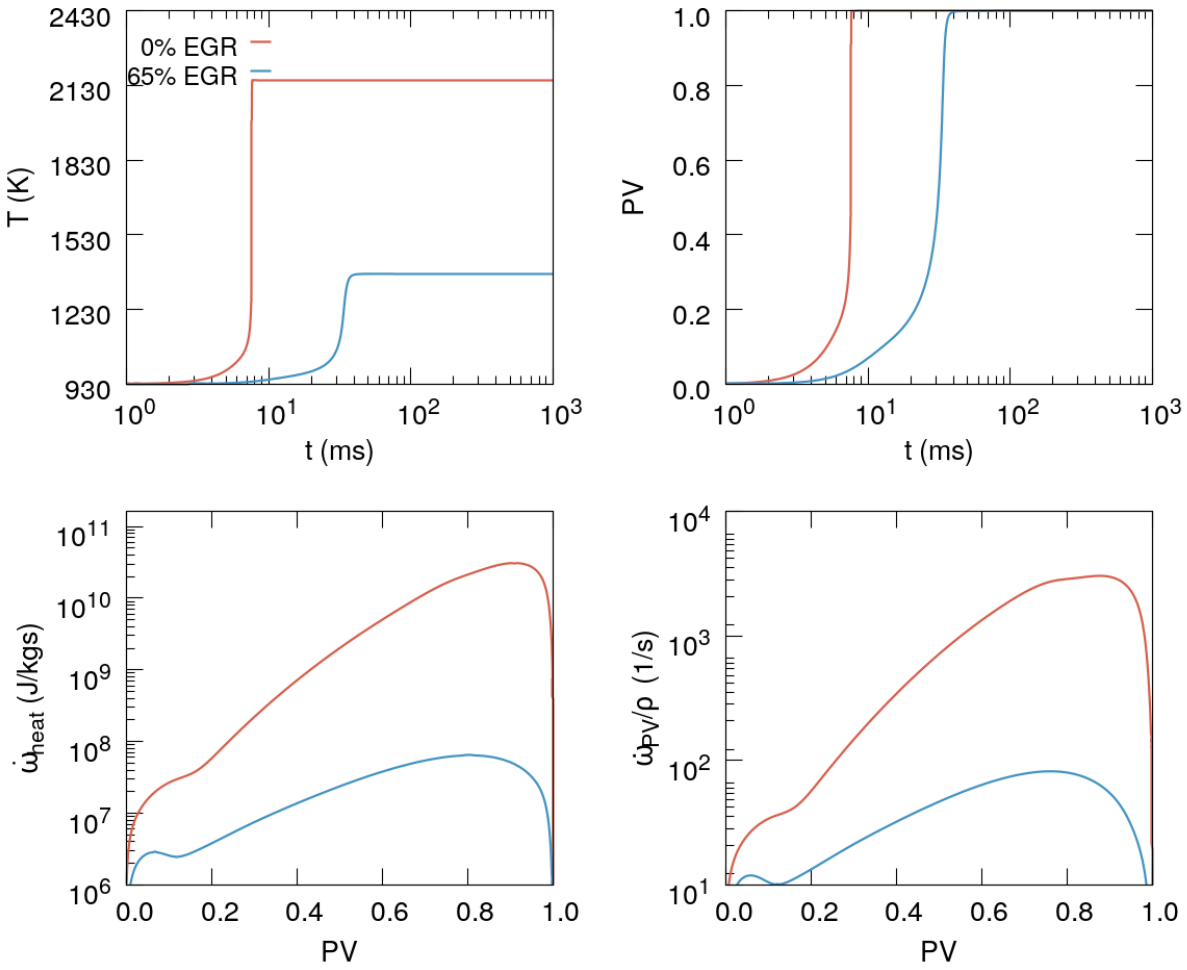

Figure 4.5: Comparison of $T, PV, \dot{\omega}_{\text{heat}}, \dot{\omega}_{\text{PV}}$ for different EGR rates with same Z =0.03595, p =22.4 bar, T_{u} =930 K. Note the logarithmic scaling of time axes on the two topmost diagrams [128].

unburnt temperatures and pressures with a fixed mixture fraction $Z = 0.0409$ which corresponds to $\lambda = 1.3$. To avoid any confusion, one can re-denote the unburnt temprature and pressure at which the exhaust gas is created as T_{u}^{EGR} and p_0^{EGR} respectively. Once the reaction reaches the chemical equilibrium for given initial condition, $T_{\text{u}}^{EGR}, \lambda = 1.3$ and p_0^{EGR}, the exhaust gas is ready to be mixed with the fresh air-fuel mixture. The fresh air fuel mixture has the unburnt temperature $T_{\text{u}}^{\text{FreshMix}}$ and pressure p_0^{FreshMix} which have the same values as T_{u}^{EGR} and p_0^{EGR} respectively. According to the desired amount of exhaust gas (e.g., $50\%EGR$ or $65\%EGR$) the fresh mixture and exhaust gas are mixed at $T_{\text{u}} (= T_{\text{u}}^{\text{FreshMix}} = T_{\text{u}}^{EGR})$ and $p (= p_0^{EGR} = p_0^{\text{FreshMix}})$ by varying the mixing state of the fresh air $\lambda^{\text{FreshMix}}$. The tabulation of λ excludes the material in the by-mixed exhaust gas and it refers only to the λ of fresh mixture, i.e., $\lambda = \lambda^{\text{FreshMix}}$. Here it is necessary to remind the reader that in this work mixture fraction Z is tabulated and the denotation of λ is used here because it is a more practical definition of mixing state for engine researchers.

In summary the tabulated independent variables are:

- T_{u} $(= T_{\mathrm{u}}^{EGR} = T_{\mathrm{u}}^{\mathrm{FreshMix}})$
- p $(= p_0^{EGR} = p_0^{\mathrm{FreshMix}})$
- λ $(= \lambda^{\mathrm{FreshMix}})$
- EGR

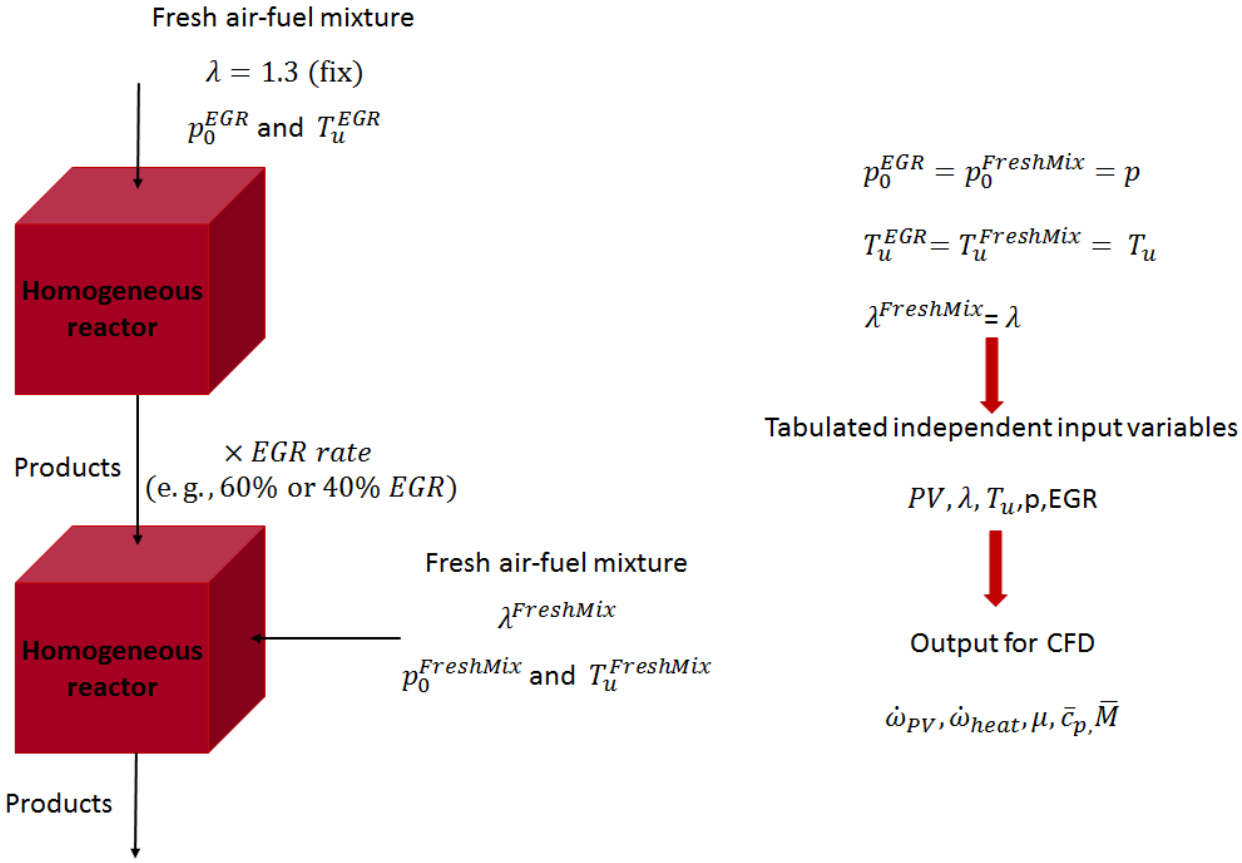

Figure 4.6: Schematic presentation of EGR extention in the chemistry table

For the simulation of CAI engines operated with spray and high amount of EGR (see section 7.1) a wide range of mixture fraction Z (λ), T_{u}, p and and EGR is to be covered by the manifold. The number of tabulation points in each dimension and the tabulation limits (expressed in original variables) are given in Table 4.2.

For these engine-relevant initial conditions, 34650 detailed chemistry calculations are performed and pre-tabulated for later use in CFD/LES simulations. For this, the tabulated data along each trajectory are interpolated onto an equidistant grid along the progress variable PV direction. These tabulated (dependent) variables (outputs) are $\dot{\omega}_{\mathrm{PV}}$, $\dot{\omega}_{\mathrm{heat}}$, $\bar{c_p}, \bar{\mu}$, $\overline{W}$ (specific heat capacity at constant pressure, viscosity, and mean

Table 4.2: Ranges of the five-dimensional table to be used in CFD calculations

Independent variable variable	Number of tabulation points	Tabulation limits
λ	14	0.3 to 2.0
T_{u}	25	500K to 1250K
EGR	11	0% - 100%
p	9	10 bar to 63bar

molar mass, respectively).

An equidistant, rectangular tabulation scheme in all independent variables $(Z, T_{\mathrm{u}}, p, \mathrm{EGR})$ can be employed. However this tabulation scheme can be impractical since, the dependent variables such as source terms for PV or heat release or $\bar{c}_p$ may depend on the tabulation variables in a non-linear fashion. For example, an equidistant grid points in λ with a spacing 0.2 would hardly change the magnitude of depending variables in high ranges of λ e.g., from $\lambda = 1.5$ to $\lambda = 1.7$. However for low ranges of λ (e.g., $0.5 \leq \lambda \leq 0.7$) there are big changes of depending variables. Or considering another independent variable p, spacing of 5 bar would be acceptable at pressures; for instance, between 40 bar and 45 bar where there is not a big differences between the dependent variables. On the other hand, the same tabulation spacing would be quite rough at lower pressures e.g., from 5 to 10 bar. Therefore, in this work independent variables are mapped to certain tabulation functions, and the values of these functions are then tabulated on an equidistant grid. The overall goal is the proper resolution of the variables. In this work employed tabulation functions are χ_Z, $\chi_{T_{\mathrm{u}}}$ and χ_p for Z , T_{u} and p respectively:

- $\chi_Z = Z_{\mathrm{st}}/(Z_{\mathrm{st}} + Z)$
- $\chi_{T_{\mathrm{u}}} = 1000/T_{\mathrm{u}}$
- $\chi_p = \log10(p)$

The EGR rate was tabulated directly, without employing an intermediate tabulation function, as defined in Eq. (4.29). By combining all trajectories, the full table is 5-dimensional and gets accessed with PV, Z, T_{u}, p and EGR.

The five-dimensional tabulation is illustrated in Figure 4.7 by varying the independent variables λ, T_{u}, p, EGR. In this figure, a typical condition as encountered in a compression engine, is chosen, namely λ=1.04, T_{u}=930K, $p = 25$bar, $EGR = 66\%$. On the y-axes of the subfigures (from 1 to 4), reaction progress is represented by PV. The figure shows how the chemical source term $\dot{\omega}_{\mathrm{PV}}$ changes for CAI engine-relevant ranges of λ (subfigure (1)), T_{u} (subfigure (2)), p (subfigure (3)) and EGR (subfigure (4)). For the same CAI engine relevant condition the evolution of source term for heat release $\dot{\omega}_{\mathrm{heat}}$ is plotted in Figure 4.8 for the same ranges of λ (subfigure (1)), T_{u} (subfigure (2)), p (subfigure (3))

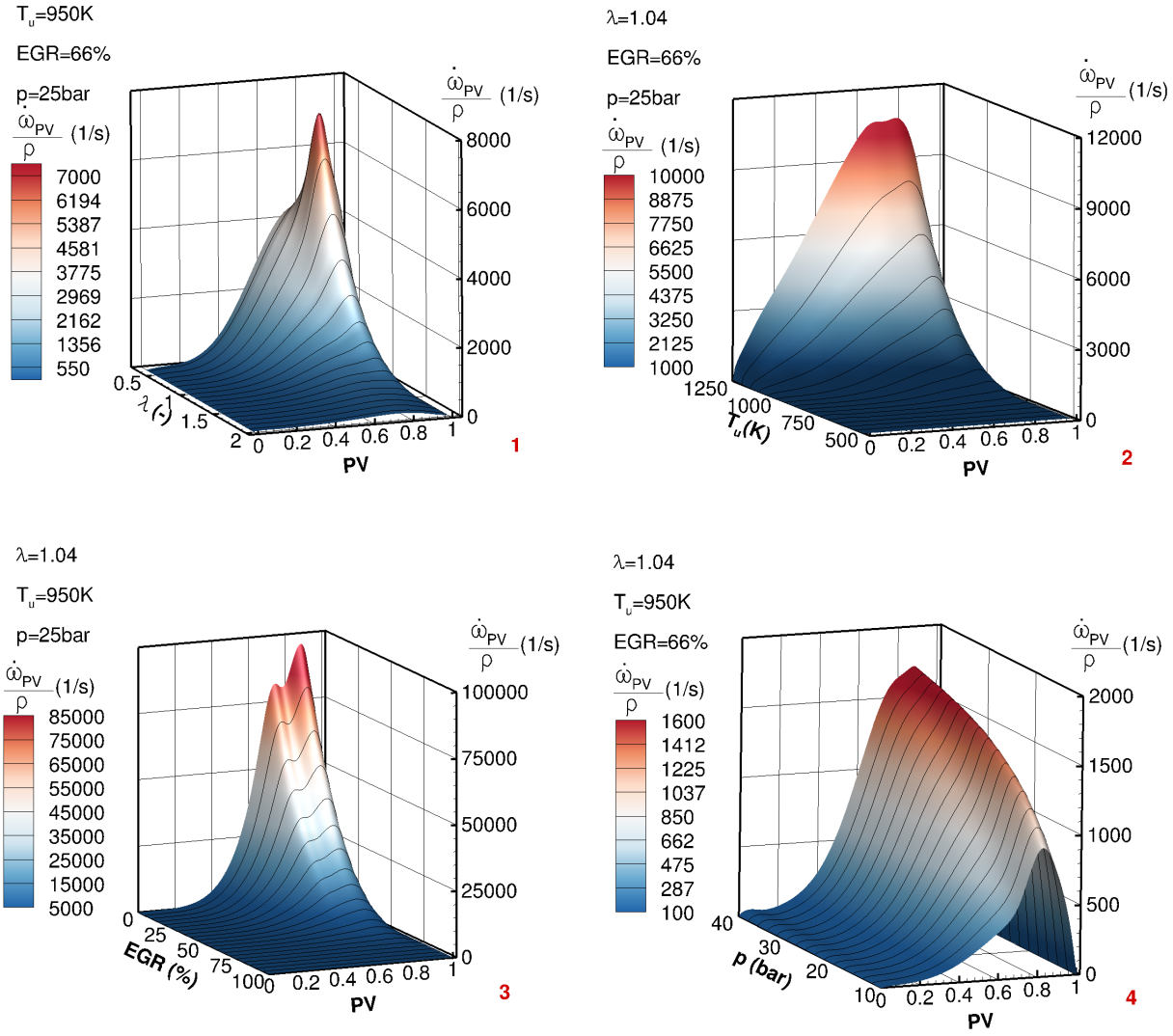

Figure 4.7: 3D plots from the chemistry table showing the evolution of $\dot{\omega}_{\mathrm{PV}}$ at λ=1.04, T_{u}=950K, $p = 25$bar, $EGR = 66\%$. In subfigures (1) to (4), the independent variables λ, T_{u}, p and EGR are varied, respectively.

and EGR (subfigure (4)) as in Figure 4.7.

In general, the Figures 4.7 and 4.8 show similar evolution forms for each independent variables $\lambda, T_{\mathrm{u}}, EGR, p$ and they illustrate that p has the weakest influence on both $\dot{\omega}_{\mathrm{PV}}$ and $\dot{\omega}_{\mathrm{heat}}$ compared to other independent variables λ, T_{u} and EGR. For instance in Figure 4.7, at $PV = 0.5$ where the reaction is halfway complete, changing λ from 0.8 to 1.4 (subfigure (1)) and p (subfigure (4)) from 40 bar to 30 bar, reduces $\dot{\omega}_{\mathrm{PV}}$ by factors of almost 3.5 and 1.1 respectively. A similar trend can be observed for heat release. In Figure 4.8 one can see that changing λ from 0.8 to 1.4 (subfigure (1)) and p (subfigure (4)) from 40 bar to 30 bar, reduce $\dot{\omega}_{\mathrm{heat}}$ by almost factors of 2 and 1.01 respectively.

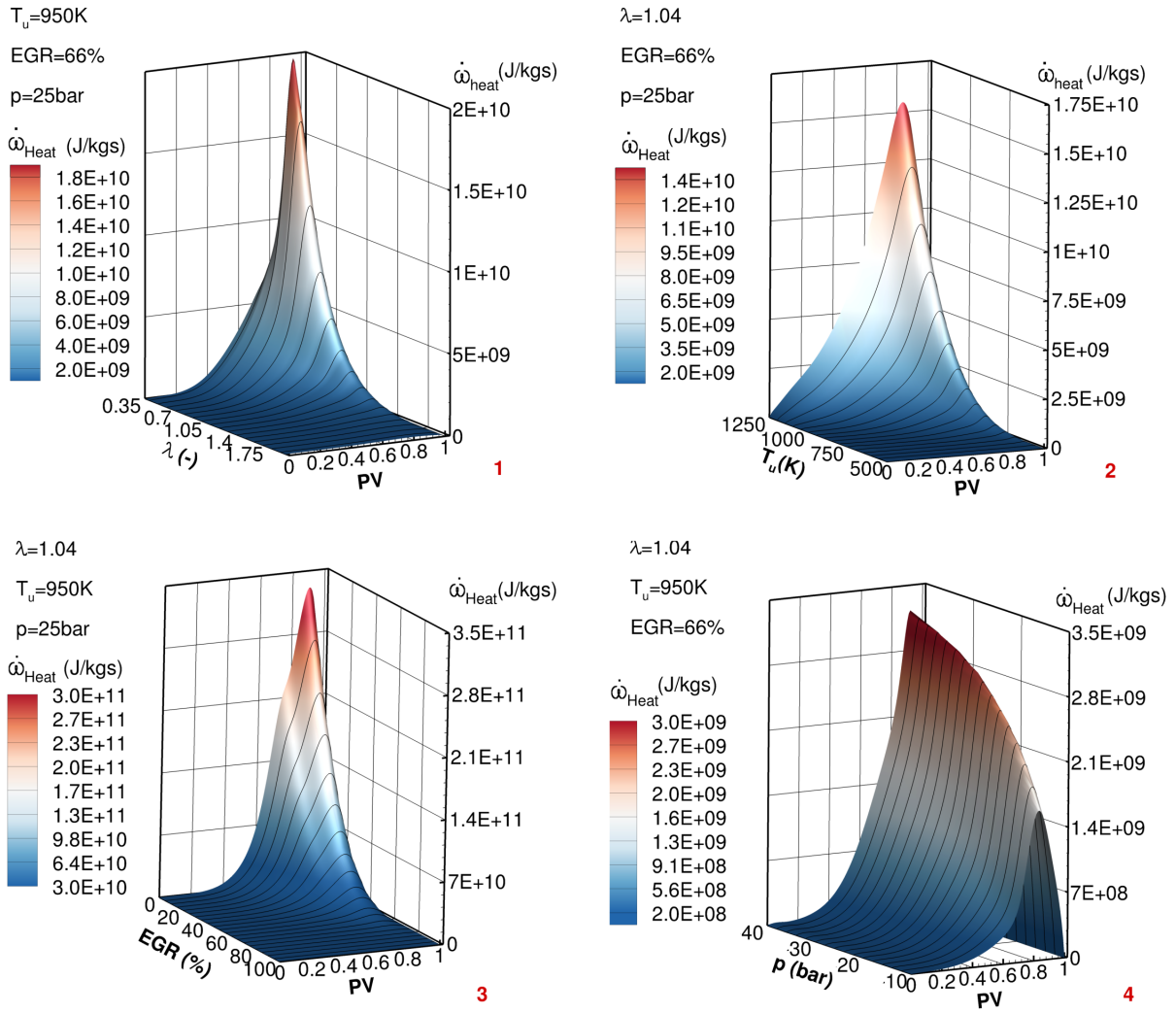

Figure 4.8: 3D Plots from chemistry table showing the evolution of $\dot{\omega}_{\text{heat}}$ at λ=1.04, T_{u}=950K, p = 25bar, EGR = 66%. In subfigures (1) to (4), the independent variables λ, T_{u}, p and EGR are varied, respectively.

In subfigure 3 of both figures 4.7 and 4.8 where influence of EGR is illustrated, one sees two humps in $\dot{\omega}_{\text{PV}}$ and $\dot{\omega}_{\text{heat}}$ fields respectively. This humps correspond to two-stage ignition. This two-stage ignition disappears for example if λ is set to 0.6 instead of 1.04. This change in ignition behaviour due to λ is illustrated in Figure 4.9. In the left and right sides of the Figure 4.9 $\dot{\omega}_{\text{PV}}$ fields are displayed as a function of EGR and PV at same T_{u}=930K and p = 25bar but different mixing state λ=1.04 and λ=0.6, respectively.

To show the EGR influence in more detail two dimensional slices are plotted for the same engine relevant condition namely T_{u} = 930 K, λ = 1.04 p = 25 bar in Figure 4.10. The upper and lower slices display $\dot{\omega}_{\text{PV}}$ and $\dot{\omega}_{\text{Heat}}$ fields against the progress variable PV respectively. From the upper slices one observes that increasing EGR from 0% EGR to 30% EGR and to 60% EGR the most favourable λ range for ignition shifts to a lower λ range. For 0% EGR, 30% EGR and 60% EGR these ranges are $0.82 \leq \lambda \leq 0.645$, $0.743 \leq \lambda \leq 0.552$ and $0.56 \leq \lambda \leq 0.47$ respectively as shown in the upper subfigures

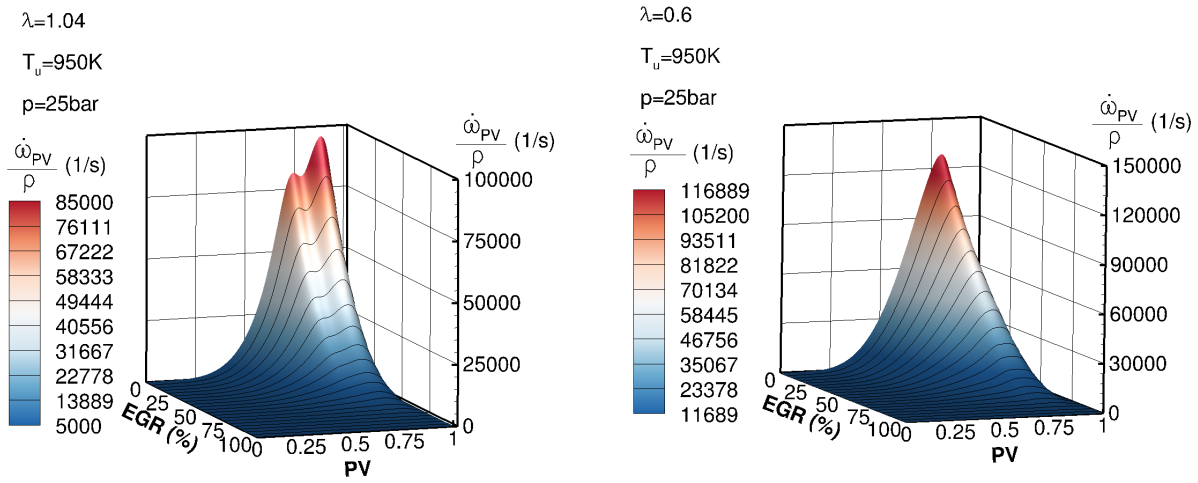

Figure 4.9: Evolution of $\dot{\omega}_{\mathrm{PV}}$ as a function of EGR and PV at same T_{u}=930K and p = 25bar but different mixing state λ=1.04 (left) and λ=0.6 (right).

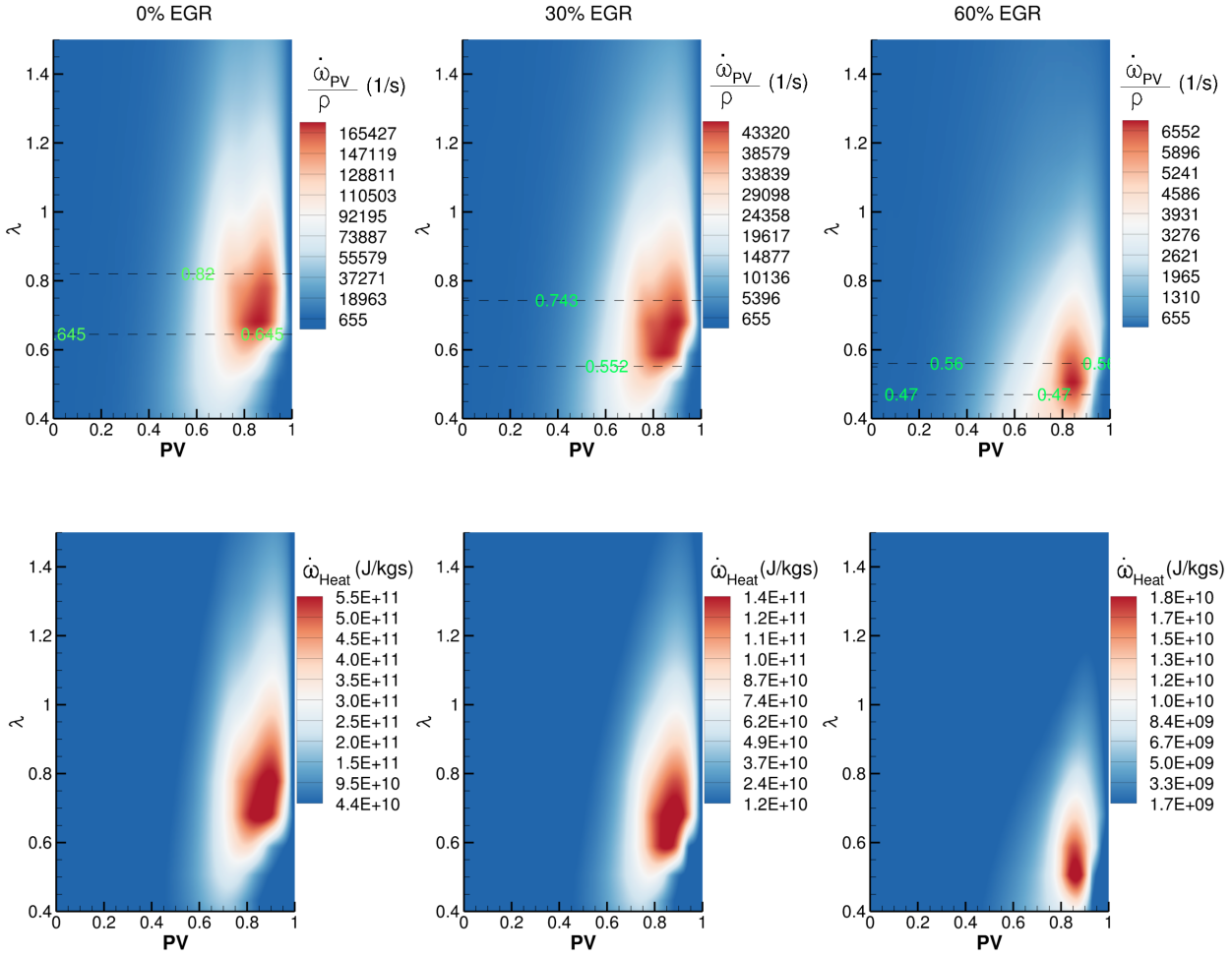

Figure 4.10: 2D slices from the chemistry table showing $\dot{\omega}_{\mathrm{PV}}$ in λ, PV space with 0% 33% and 66% EGR for T_{u}=950K, p = 25 bar.

with dashed lines. This shift in λ range is caused by the excess oxidizer in species composition of *EGR*. As already mentioned, the *EGR* is the burned gas of a fresh mixture with $\lambda = 1.3$. And this amount of λ corresponds to 30% excess air which than shows itself in the burned gas. Finally, the figure shows that increasing *EGR* from 0% *EGR* to 60% *EGR* the source terms decrease for progress variable and heat release almost by factors of 25 and 30 respectively.

4.4.4.1 Interpolation errors in look-up table

The values of the dependent variables for any state inside the tabulation grid can be retrieved from the table by multi-dimensional interpolation. Different interpolation schemes are possible for this task; in this work, a simple linear interpolation method is employed. However, using this method, one obtains interpolation error which might effect later on the results of CAI simulations. To display this problem, in Figure 4.11 reaction trajectories obtained from tabulated 5-dimensional manifold by using linear interpolation (denoted as TC) is compared with detailed chemistry (denoted as DC) results. The homogeneous reactor simulations using detailed chemistry are performed explicitly for the comparisons presented in Figure 4.11. In this figure, evolution of the source terms for heat release $\dot{\omega}_{\mathrm{Heat}}$ and chemical reaction $\dot{\omega}_{\mathrm{PV}}$ are compared at different conditions $\mathbf{\Psi}_{0,1}$, $\mathbf{\Psi}_{0,2}$ and $\mathbf{\Psi}_{0,3}$. These initial conditions are listed in table 4.3.

Table 4.3: Initial conditions for homogeneous reactor simulations in Figure 4.11

$\mathbf{\Psi}_{0,i}$	λ	T_{u}(K)	p (bar)	*EGR*
$\mathbf{\Psi}_{0,1}$	1.0	930	22.4	65%
$\mathbf{\Psi}_{0,2}$	1.0	1017.5	32.4	65%
$\mathbf{\Psi}_{0,3}$	1.52	1017.5	32.4	65%

Generally, Figure 4.11 shows that by using linear interpolation one obtains higher values for both $\dot{\omega}_{\mathrm{PV}}$ and $\dot{\omega}_{\mathrm{Heat}}$. The trajectories represent different ignition behaviour compared to results directly taken from detailed chemistry calculations. Higher values of $\dot{\omega}_{\mathrm{Heat}}$ and $\dot{\omega}_{\mathrm{PV}}$, lead an increase in chemical equilibrium temperature and a decrease in ignition delay, respectively. Since tabulation is done in PV space, a comparison involving the temporal evolution of auto-ignition cannot be made. The effects of interpolation errors on temporal development of temperature and ignition delay will be presented and discussed in the verification section 6.1.

By further evaluating the comparison between TC and DC Figure (4.11) one observes that the error changes, if the initial conditions change. In the figure the reaction trajectory with initial condition $\mathbf{\Psi}_{0,3}$ (green coloured line, denoted as TC) shows an outstanding deviation from the detailed chemistry result in $\dot{\omega}_{\mathrm{Heat}}$ field compared to TCs at $\mathbf{\Psi}_{0,1}$ and $\mathbf{\Psi}_{0,2}$. This difference in deviations depends on how far the desired and

tabulated values of the independent variables lay from each other and also the non-linear relation between independent and dependent variables. Hence, the magnitude of the failure due to interpolation cannot be generalized.

By comparing DC and TC at tabulated values, one could see if the interpolation error disappears. For that purpose a single trajectory is created to be also used later in the verification section (6.1). This single trajectory is obtained at the same conditions as $\mathbf{\Psi}_{0,3}$ from which the results are denoted as TC2. The results of TC2, TC and DC are compared in Figure 4.12. One can see from the comparison, that the interpolation error disappears if interpolation is not required.

Consequently, this problem of linear interpolation could be minimized by generating finer grid points in tabulation. However, a finer the look-up table in each of the 5-dimensions would have immense RAM costs. Instead of a finer look-up table, more accurate interpolation schemes can be employed, but they are be more complex and also computationally more intensive. For the first application in CAI of our 5-dimensional look-up table, the simple linear scheme was found to be sufficient for our purpose and therefore it is employed in this work.

4.4.5 Turbulence-chemistry interaction

The turbulence-chemistry interaction on subgrid scales could be included via presumed probability density function (pdf) integration of the chemistry table during a pre-processing step. The advantage of this model lies in its applicability in LES context in order to include the effects of unsteady flow fields. A further advantage is the incorporation of information obtained from detailed chemistry via the Progress Variable Model, for which only a few additional transport equations need to be solved. However in our case the application of pdf would require two additional access variables for the look-up table, being variances of mixture fraction Z and EGR. Since the dimension of the current chemistry table is already very high (5- dimensions), by involving these two access variables, the look up table would be immense large (7-dimensions). This would then obviously increase the RAM demand of the CAI simulations. Another problem is the interpolation errors within the look-up table. For our case, increasing the dimension of the chemistry table would mean that a coarser look-up table must be generated. This would lead an increase in the interpolation errors (see the previous chapter). This problem might not be a issue for any other CFD code but due to RAM limitations of in this work employed CFD code (see Chapter 5 for code performance), the higher dimension of the look-up table is, coarser it must be generated. Therefore, for the first application of the combustion model on the complicated CAI system, the employed look-up table does not involve variances of Z and EGR, therefore no turbulence-chemistry interaction. However, future work must somehow involve the turbulence-chemistry interaction.

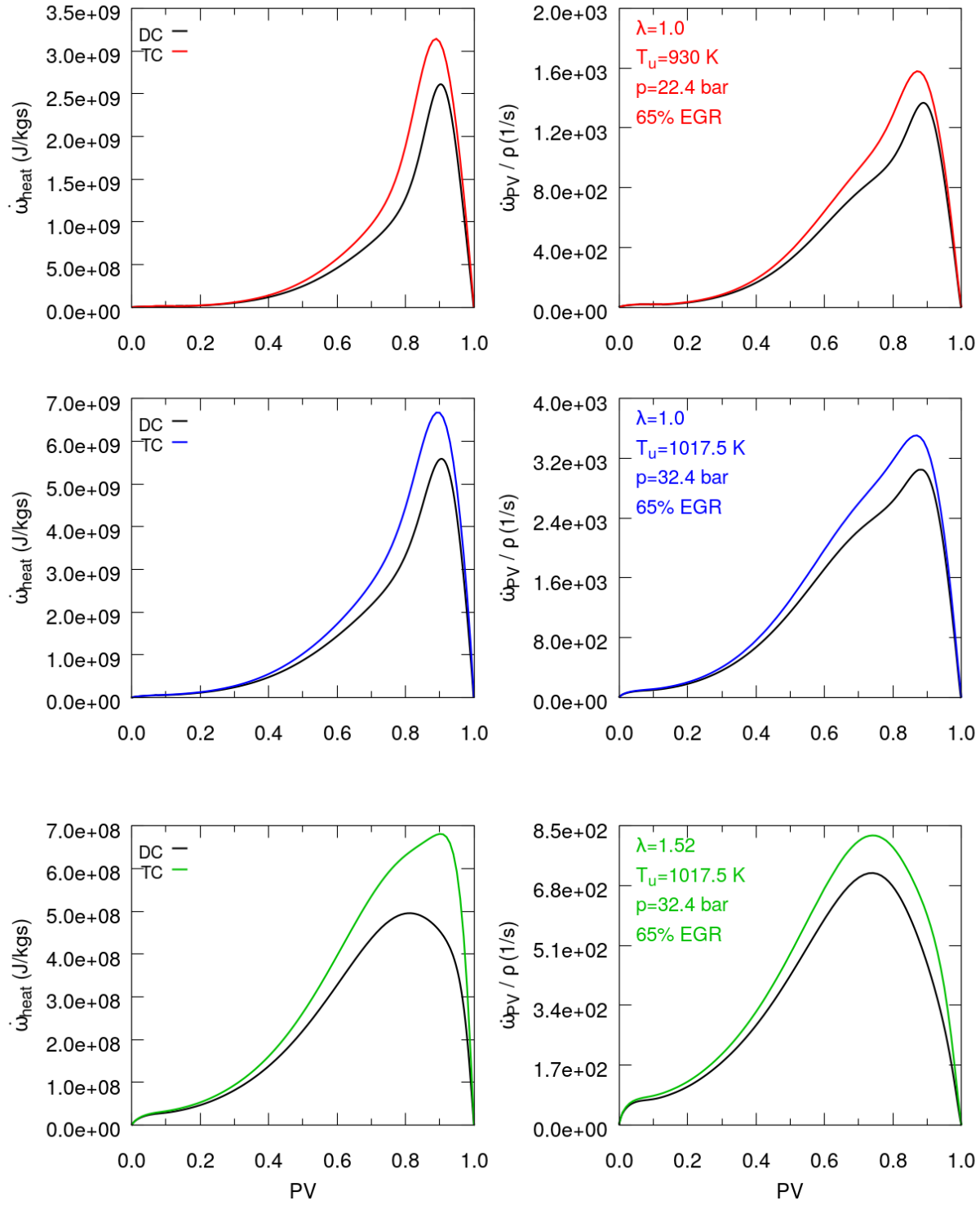

Figure 4.11: Comparison of detailed chemistry (DC) and a reaction trajectory extracted from the multi-dimensional chemistry table (TC)

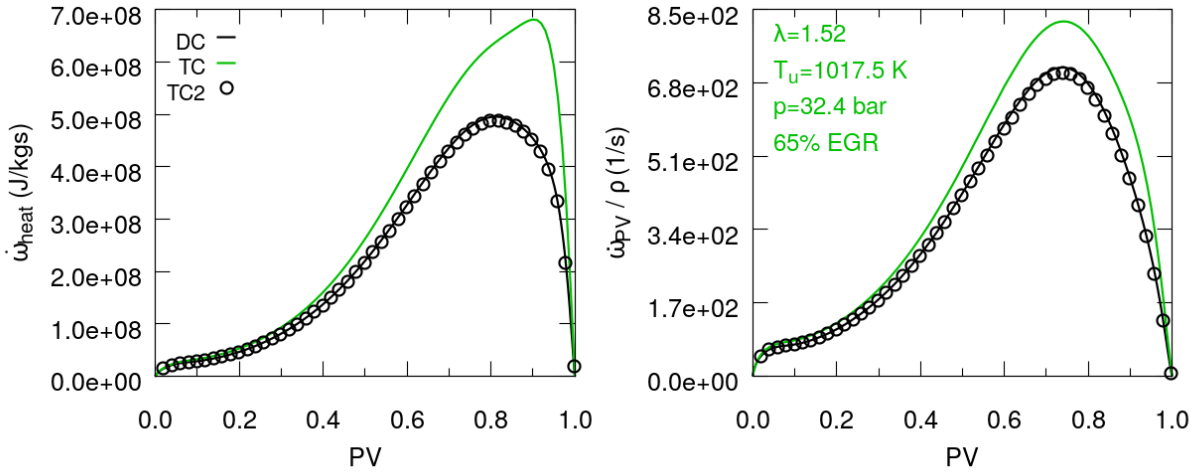

Figure 4.12: Comparison of detailed chemistry (DC) and a reaction trajectory extracted from multi-dimensional chemistry table (TC) and an explict prepared single trajectory (TC2)

4.5 Coupling of the tabulated chemistry model with the LES solver

The tabulated chemistry approach is coupled to the LES-based CFD code. The details of CFD code will be given in section 5. The standard Smagorinsky model [108] with a model constant of $C_s = 0.1$ is used for the subgrid-scale (SGS) modeling. The filtered transport equations for mass, momentum and internal energy solved in Kiva-4MPI are given in Eq. (3.53), (3.54) and (3.56). Additionally, three more equations for transport, Eq. (4.37), (4.38) and (4.39) for the progress variable PV, mixture fraction Z and exhaust gas rate EGR, respectively.

$$\frac{\partial}{\partial t}\left(\bar{\rho}\widetilde{PV}\right) + \frac{\partial}{\partial x_j}\left(\bar{\rho}\tilde{u}_j\widetilde{PV}\right) = \frac{\partial}{\partial x_j}\left[\frac{(\bar{\mu}+\mu_t)}{Sc}\frac{\partial\widetilde{PV}}{\partial x_j}\right] + \bar{\dot{\omega}}_{PV} \tag{4.37}$$

$$\frac{\partial}{\partial t}\left(\bar{\rho}\tilde{Z}\right) + \frac{\partial}{\partial x_j}\left(\bar{\rho}\tilde{u}_j\tilde{Z}\right) = \frac{\partial}{\partial x_j}\left[\frac{(\bar{\mu}+\mu_t)}{Sc}\frac{\partial\tilde{Z}}{\partial x_j}\right] + \bar{\dot{\omega}}_{\text{spray}} \tag{4.38}$$

$$\frac{\partial}{\partial t}\left(\bar{\rho}\widetilde{EGR}\right) + \frac{\partial}{\partial x_j}\left(\bar{\rho}\tilde{u}_j\widetilde{EGR}\right) = \frac{\partial}{\partial x_j}\left[\frac{(\bar{\mu}+\mu_t)}{Sc}\frac{\partial\widetilde{EGR}}{\partial x_j}\right] \tag{4.39}$$

μ, μ_t are the laminar and the turbulent viscosities respectively. In Eq. (4.37), (4.38) and (4.39) the diffusive terms imply the simplification of treating the normalized progress variable PV, the mixture fraction Z and EGR as if they are regular scalars. The source term $\dot{w}_{\text{spray}}$ in Eq. (4.38) describes the effect of droplet evaporation onto mixture fraction and $\dot{w}_{PV}$ in Eq. (4.37) is the source term for the reaction progress variable with the unit of kg/m^3s. The EGR is treated as a passive scalar without any source term. In this

work, the Schmidt-Number is defined as $Sc = 0.7$.

The transport equation of the normalized progress variable Eq. (4.37) implies that in the LES Code the progress variable is treated like a chemical specie, whose diffusive transport is governed by a Fick-type diffusion term. This is a straightforward and simple treatment. In [80] a more physically motivated approach for transporting the normalized progress variables are introduced. However, its application with the high dimensional tabulation, would be complex and computationally expensive. Therefore in this work, for the sake of simplicity the normalized progress variable treated as a regular chemical specie (or one can say as a regular scalar) which is simply transported as given in Eq. (4.37) without the consideration of numerous "cross-diffusion" terms.

To solve the above mentioned equations on moving grids, the (Arbitrary Lagrangian-Eulerian) ALE scheme is utilized in combination with the Semi-Implicit Method for Pressure Linked Equations (SIMPLE) algorithm and the conjugated residual method [116]. The details to the solution procedure will be given in chapter 5.

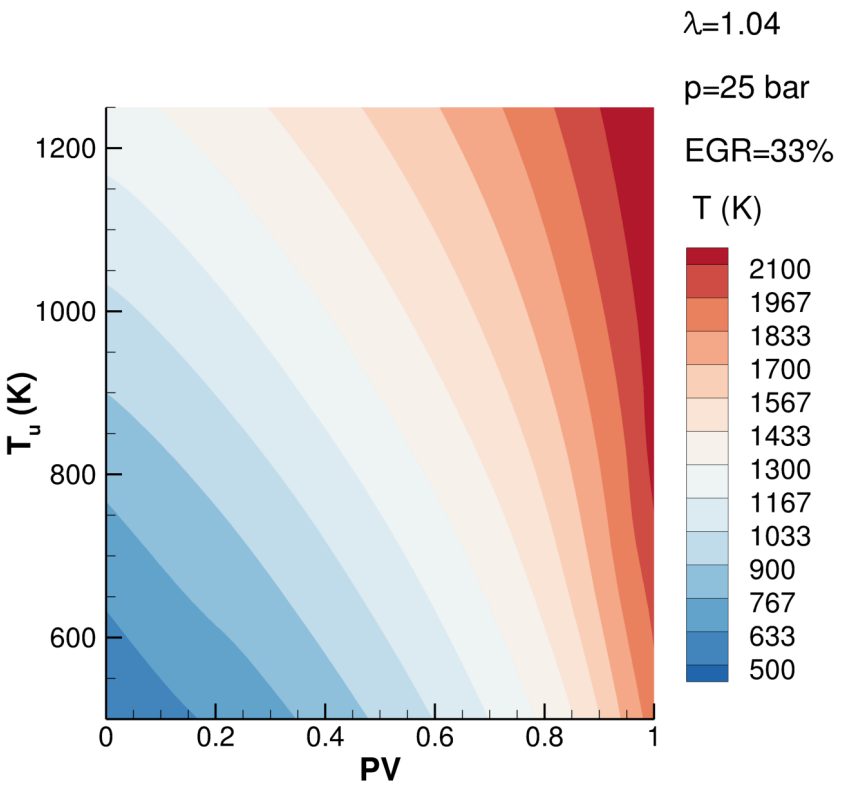

Figure 4.13: T as a function of T_u and PV at $\lambda = 1.04, p = 25bar, EGR = 33\%$

Calculation of the unburnt temperature T_u

During the simulation, the material parameters specific heat capacity (c_p) of mixture and viscosity (μ), the source term for progress variable $\dot{w}_{PV}$ as well as the source term for heat release $\dot{\omega}_\mathrm{heat}$ are provided by the tabulated chemistry database. To get these outputs

from the lookup table for each time step the access variables PV, Z, T_u, EGR and p must be known. Solving the Eqs. (4.37), (4.38), (4.39) and (3.54) one obtains PV, Z, EGR and p respectively. However, the remaining table access parameter T_u (temperature of unreacted mixture) is still unknown. Unlike homogeneous reactor simulations, T_u varies in engine simulations strongly due to compression, heat losses through the cylinder walls and heat transfer within the gas. Therefore, T_u must be updated in engine applications at each time step.

In principle, a partial differential equation (PDE) as given in Eq. (4.37) can be also formulated for T_u. However in this work instead of solving a PDE to determine T_u, a more straightforward procedure is employed which based on solving an algebraic equation. Accordingly, at each time step, the instantaneous temperature $\tilde{T}$ obtained from Eq. (3.56) is compared with the temperatures of the trajectories in the chemistry table. Its location in the temperature field of these trajectories can thereby be identified. The corresponding T_u can then be reconstructed by means of linear interpolation. This procedure is illustrated with a two dimensional slice from chemistry table in Figure 4.13. The figure shows that for given values of Z, EGR and p, the instantaneous temperature $\tilde{T}$ is a function of PV and T_u. This relation can be simply expressed as in Eq. (4.40). In this figure this relation is shown for trajectories at $\lambda = 1.04, p = 25bar, EGR = 33\%$ with different T_u. For other values of Z, EGR and p the plot would show same relation between T_u and $\tilde{T}$ but with different slopes and different ranges of instantaneous temperature.

$$\widetilde{T} = f(PV, Z, T_u, p, EGR) \tag{4.40}$$

4.5.1 Applicability of the model to systems with diffusion

In CAI engines, which are commonly operated with direct injection and high amounts of EGR, inhomogeneities in composition and temperature fields are observed [26, 126, 63] (see also chapter 7). Here at this point the question is whether the reduced model based on homogeneous reactors delivers satisfactory results in CAI systems with high inhomogeneities where diffusion is expected.

To investigate at which strength of diffusion processes the reduced model is still applicable, numerical studies with mixing reactors are presented in this section. These are performed by Dr.-Ing. Robert Schießl (ITT,KIT) by using the results obtained from CAI simulations. These mixing reactors mimick an isobaric reacting system that is perturbed by transport due to diffusion. Its evolution is governed by the following system of ODEs, which extends the ODEs for a homogeneous reactor Eqs. (4.26),(4.27) and (4.28) by mixing terms:

$$\begin{aligned}\frac{dh}{dt} &= \Omega_{\text{mix}}(h_{\text{surr}} - h)\\ \frac{dp}{dt} &= 0\\ \frac{dY_i}{dt} &= \Omega_{\text{mix}}(Y_{i,\text{surr}} - Y_i) + \frac{\dot{\omega}_i M_i}{\rho}\end{aligned} \tag{4.41}$$

where $Y_{i,surr}$ and T_{surr} are composition and temperature of the surrounding gas respectively. Ω_{mix} is the mixing speed at which inflow mass $\dot{m}_{in}$ from the reactor's surroundings is added.

$$\Omega_{\text{mix}} = \frac{\dot{m}_{\text{in}}}{m} \tag{4.42}$$

where m is the total mass in the reactor. The outflowing material has the same composition, temperature and pressure as the reactor contents. The mixing rate Ω_{mix} defined in Eq. (4.42) is a parameter which describes the mass exchange by mixing. This mixing can be interpreted as diffusion due to inhomogeneities in temperature and composition fields in engine applications.

Solving system (4.41) for given initial values $(h, p, Y_i)_0$ and for fixed $h_{\text{surr}}, Y_{i,surr}$, one obtains a trajectory for the mixing reactor, based on detailed chemistry. One can derive the corresponding set of equations in the reduced model, by which the mixing reactor would also be simulated in the LES code. However, this test case was not studied within the LES code. Simulating such a system within the LES code would be a valuable verification case and it is suggested to be performed for the future work.

$$\begin{aligned}\frac{dh}{dt} &= \Omega_{\text{mix}}(h_{\text{surr}} - h)\\ \frac{dp}{dt} &= 0\\ \frac{dPV}{dt} &= \Omega_{\text{mix}}(PV_{\text{surr}} - PV) + \frac{\dot{\omega}_{PV}}{\rho}\\ \frac{dEGR}{dt} &= \Omega_{\text{mix}}(EGR_{\text{surr}} - EGR)\\ \frac{dZ}{dt} &= \Omega_{\text{mix}}(Z_{\text{surr}} - Z)\end{aligned} \tag{4.43}$$

The results here are obtained with a detailed chemistry solver and an algebratic solver which uses a reduced model and the ODEs given in Eq. (4.43). Here in the ODE system, the equation for the enthalpy h is not applied directly in the reduced model. Instead, an algebraic equation for T_{u} is solved in each solution timestep of the explicit solver. This is the same solution procedure as in the LES solver. Therefore, it is fair to claim that the results obtained from the reduced model would deliver almost the same results as the

LES code would.

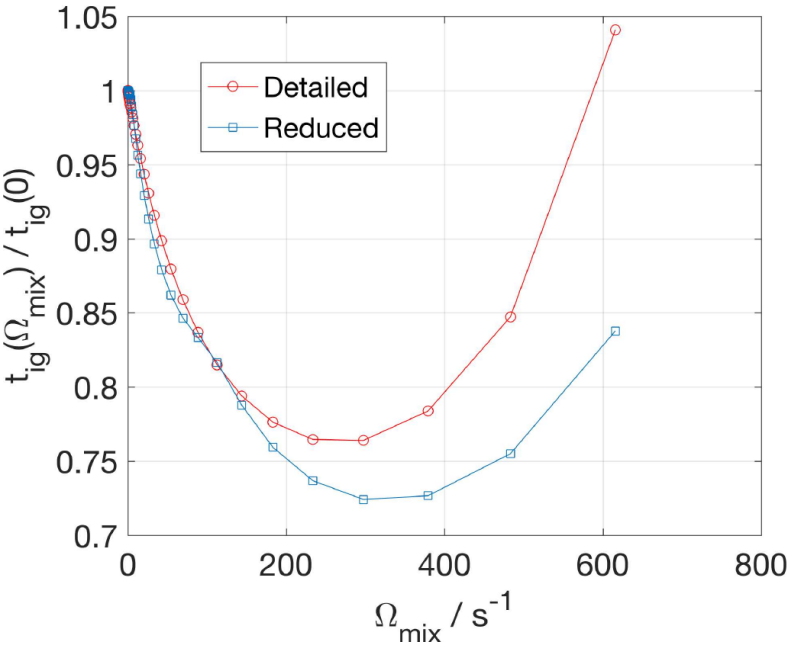

Figure 4.14: Change in ignition delay for different mixing rates [128].

Results of the mixing reactor from the detailed model (eq. 4.41) and the corresponding reduced model (eq. 4.43) are compared. In Figure 4.14 it is shown for a situation that is encountered in our CAI engine immediately prior to ignition, namely one where $Y_{i,\mathrm{surr}}$ corresponds to unbunrt gas with $T_\mathrm{u} = 907\mathrm{K}$, $EGR = 51\%$, $\lambda = 1.14$ and $p = 13bar$. The reactor on the other hand has the initial condition, namely $T_\mathrm{u} = 979\mathrm{K}$, $EGR = 62\%$, $\lambda = 0.9$ and $p = 13bar$. These conditions are observed from results of CAI simulations will be presented in chapter 7.

In Figure 4.14 the dependency of ignition delay t_{ig} on the mixing speed is compared for both the detailed (red curve) and the reduced model (blue curve). In the figure t_{ig} is normalized with $t_{ig}(0)$. The $t_{ig}(0)$ corresponds to ignition delay in reactor without mixing surrounding gas, i.e. $\Omega_\mathrm{mix} = 0$. From the results we obtain that for mixing speeds below about $\Omega_\mathrm{mix} = 150s^{-1}$ detailed and reduced model deliver almost identical ignition delays. At fast mixing rates where chemistry and transport processes are coupled strongly, i.e., combustion is not dominated with chemistry anymore, reduced model starts to become insufficient and deviates more from detailed model. However for CAI engine typical mixing rates, i.e., $\Omega_\mathrm{mix} \leq 10s^{-1}$ the reduced model is capable to describe auto-ignition. This estimated time scale for mixing is based on scalar sample profiles obtained from the LES simulations of the particular CAI engine. The profiles of mixing states in our CAI engine will be illustrated in chapter 7.

Chapter 5

Numerical methods

5.1 CFD code

In this work, KIVA-4mpi [117] code is employed as the CFD tool. KIVA-4mpi is the latest member of the Kiva family of codes which are developed by Los Alamos National Laboratory (LANL). The code is written in Fortran language to simulate transient three dimensional chemically reactive fluids with spray within internal combustion engines. The development of Kiva has a long history. The first version of Kiva is a further development of the code "Conchas-Spray" (May, 1982) [21] which solves the equations of transient multicomponent chemically reactive fluids. The second released version of Kiva is the Kiva-II [10]. Kiva-II extends and enhances the first version by means of computational efficiency and numerical accuracy. Additionally, new or improved physical models are involved in Kiva-II. Later on further versions of Kiva namely, Kiva-3 [8], Kiva-3V [9] and Kiva-4 [116] are released. These versions deal better with complex geometries and have more enhanced turbulence models. However, after Kiva-II, numerical schemes have not been improved further. The latest version KIVA-4mpi [117] is a parallelized version of Kiva-4. The parallelization of the code is based on message passing interface (MPI) library. In Table 5.1 the Kiva versions and their improvements compared to earlier versions are summarized.

5.2 Numerical schemes

In this work, with LES [37, 38] and tabulated chemistry approach extended (see section 4.5) KIVA-4mpi is used. However the same numerical schemes as in the original KIVA-4mpi code are employed and this chapter gives a brief description of these numerical methods.

In all versions of Kiva codes the standard Finite Volume Approach (FVM) is employed as spatial discretization to approximate the governing equations (partial differential equations) and time discretization is performed in variably implicit fashion. The FVM approach discretizes the entire region of interest with control volumes (cells). Volume integration is applied to each control volume and the volume integrals are converted to surface integrals applying Gauss' divergence theorem. After that, the integrals are approximated with quadrature rules. Volume integrals are approximated by function values at the cell center times the cell volume. Surface integrals are approximated by

Table 5.1: Improvements of Kiva starting from the code *Conchas-Spray (1982)* from

Version	Improvements
Kiva (1985)	+ 2D and/or 3D + extended spray model
Kiva-II (1989)	+ computational efficiency + numerical accuracy + new or improved physical models
Kiva-3 (1993)	+ multi block mesh
Kiva-3V (1997)	+ inclusion of intake/exhaust ports + enhanced RANS based turbulence models
Kiva-4 (2004)	+ unstructured grids
KIVA-4mpi (2009)	+ parallelization using MPI

function values at the face center times the face area.

A structured mesh is used in this work, which is composed of hexahedral cells. The velocities are defined at cell vertices in KIVA-4mpi, which is convenient because no interpolation is required for determining vertex motion [10]. In the ALE method implemented in KIVA-4mpi, the velocities are also computed on the cell centers and the accelerations of the cell-face velocities due to pressure gradients are calculated by constructing auxiliary cell so-called *momentum cells*. The thermodynamic quantities such as density, temperature, energy and pressure are saved in cell center. In Figure 5.1 (left) the cell construction and sketch of basic grid information are illustrated.

The FVM method in Kiva codes is based on *Arbitrary Lagrangian-Eulerian* [41, 100, 18] approach which combines both the Lagrangian and the Eulerian method for integrating governing equations with moving solid boundaries (piston and valve movements). Accordingly, each cycle is divided in two stages: Lagrangian stage and Eulerian stage. In Lagrangian stage the fluid moves with the vertices and no convection is considered. Also the droplet phase employs a Lagrangian particle dynamics method [10]. In the Eulerian stage (or rezoning stage) the convective terms of the governing equations are calculated.

The temporal differencing of any filtered quantity $\widetilde{Q}$ is approximated by the 1^{st} order Euler approximation with variably implicit fashion:

$$\frac{\partial \widetilde{Q}}{\partial t} \approx \frac{\widetilde{Q}^{n+1} - \widetilde{Q}^{n}}{\Delta t} \tag{5.1}$$

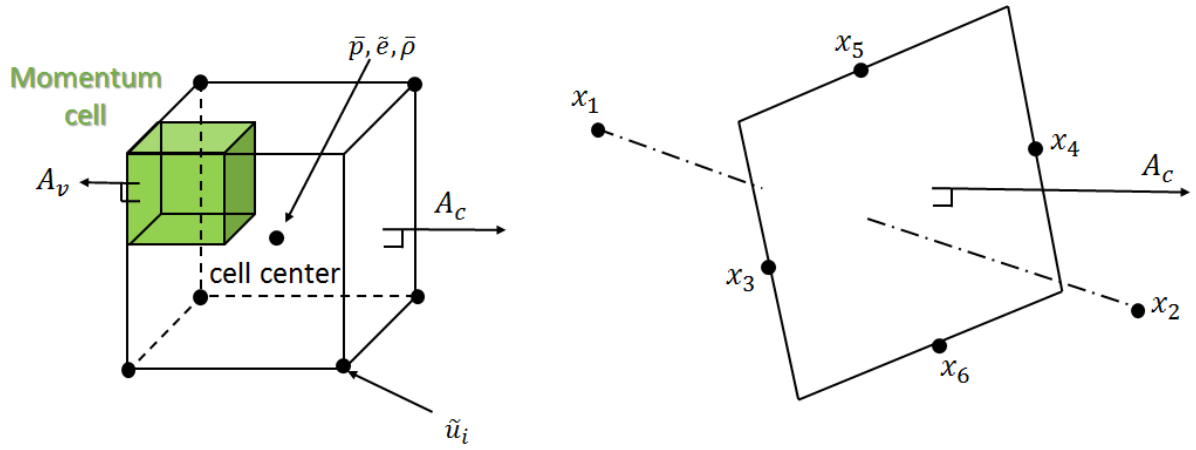

Figure 5.1: Left: Schematic illusturation of a cell and momentum cell showing where grid informations are saved. Right: Points to determine the gradient of a cell centered quantity.

where the interval $\Delta t = t^{n+1} - t^n$ is the timestep and the integer n is the cycle number. The time step is divided into three phases namely Phase A, Phase B and Phase C. Quantities at time t^n will be denoted by subscript n. Similarly, the quantities at Phase A, Phase B and Phase C will be denoted by superscripts A, B and $n+1$ (Phase C is the end of the time step therefore, instead of superscript C, $n+1$ is used.) e.g. T^A and ρ_m^B are temperature and specie density from Phase A and Phase B respectively. The flow of the computation is:

$$\widetilde{Q}^n \rightarrow \widetilde{Q}^A \rightarrow \widetilde{Q}^B \rightarrow \widetilde{Q}^{n+1} \tag{5.2}$$

Phase A and B belong to Lagrangian stage and Phase C corresponds to Eulerian stage. In Phase A, the source terms due to spray and chemical reactions are calculated. In Phase B the vertices move with the fluid and the governing equations are solved in Lagrangian form using a finite volume scheme. In this phase no convection is considered. Finally in Phase C the grid is moved to new locations. Mass, momentum and energy fluxes caused by grid movement and convection are calculated here. In Figure 5.2 this basic time stepping structure is shown schematically.

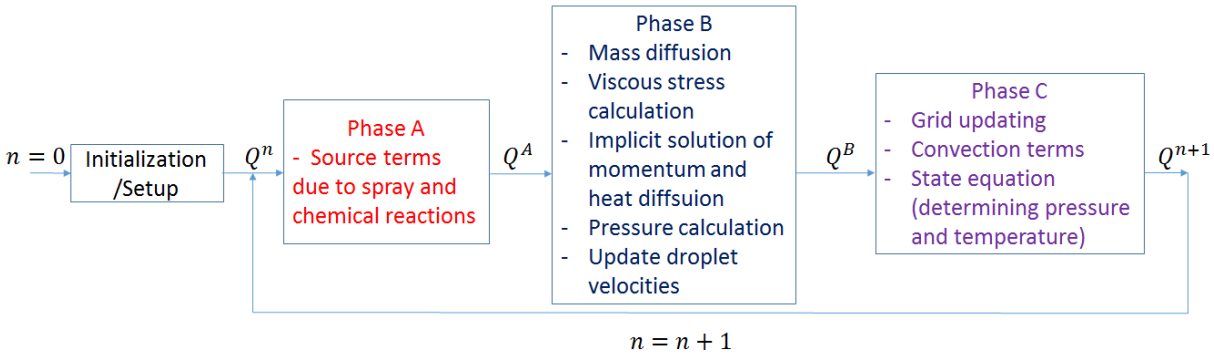

Figure 5.2: Basic time stepping in Kiva (modified from [42]).

KIVA-4mpi solves the LES filtered governing equations (3.53), (3.54), (3.56) and (3.57) presented in integral form:

Species transport:

$$\int_V \frac{\partial}{\partial t}\left(\bar{\rho}\widetilde{Y_m}\right) dV + \int_S \left(\bar{\rho}\tilde{u}_j\widetilde{Y_m}\right) n_j dA = \int_S \left(\frac{\mu_{eff}}{Sc}\frac{\partial \widetilde{Y_m}}{\partial x_j}\right) n_j dA + \int_V \overline{\dot{\omega}}_{\mathrm{n}} dV \tag{5.3}$$

Conservation of mass:

$$\int_V \frac{\partial \bar{\rho}}{\partial t} dV + \int_S \left(\bar{\rho}\tilde{u}_j\right) n_j dA = \int_V \overline{\dot{\rho}^s} dV \tag{5.4}$$

Conservation of momentum:

$$\begin{aligned} \int_V \frac{\partial\left(\bar{\rho}\tilde{u}_i\right)}{\partial t} dV + \int_S \left(\bar{\rho}\tilde{u}_i\tilde{u}_j\right) n_j dA = \\ -\int_S \bar{p} n_i dA + \int_S \left[\mu_{eff}\left(\frac{\partial \tilde{u}_i}{\partial \tilde{x}_j} + \frac{\partial \tilde{u}_j}{\partial \tilde{x}_i} - \frac{2}{3}\frac{\partial \tilde{u}_k}{\partial \tilde{x}_k}\delta_{ij}\right)\right] n_i dA + \int_V \bar{\rho} f_i^s dV + \int_V \bar{\rho} g_i dV \end{aligned} \tag{5.5}$$

where $\mu_{eff} = \bar{\mu} + \mu_t$ is the effective turbulent viscosity.

Conservation of energy:

$$\begin{aligned} \int_V \frac{\partial(\overline{\rho}\widetilde{e})}{\partial t} dV + \int_S (\overline{\rho}\widetilde{e}\widetilde{u_j}) n_j dA = -\int_S (\overline{p}\widetilde{u_j}) n_j dA \\ + \int_V \widetilde{\tau}_{ij}\frac{\partial \widetilde{u_i}}{\partial x_j} dV + \int_S \left[\frac{\left(\bar{\mu} + \frac{c_v}{c_p}\mu_t\right) c_p}{Pr}\frac{\partial \widetilde{T}}{\partial x_j}\right] n_j dA + \int_V \overline{\dot{\omega}}_{\mathrm{heat}} dV + \int_V \overline{\dot{\omega}^s} dV \end{aligned} \tag{5.6}$$

In the following sections the numerical treatment of these equations will be demonstrated.

5.2.1 Lagrangian stage

In this section the solution of the equations (5.3), (5.4), (5.5) and (5.6) in Phase A and Phase B is presented. Accordingly, the contribution of the second terms in these equations which correspond to convective terms, are not involved to the solution procedure.

Species transport

In **Phase A** contributions of chemistry and spray evaporation to species density at constant volume are calculated.

$$\frac{\rho_m^A - \rho_m^n}{\Delta t} = \dot{\rho}_m^{\text{chem}} + \dot{\rho}_m^{\text{s}} \tag{5.7}$$

Once the phase A species densities have been calculated using the relations given in Eq. (3.9) the mass fractions $\widetilde{Y}_m^A$ are determined. The total mass is $M^A = \rho^A V^A$.

In **Phase B** fluid is not convected. Therefore the total mass does not change $M^A = M^B$ from Phase A to Phase B. Using this information, mass fraction $\widetilde{Y}_m^B$ is calculated as given in Eq. (5.8) where Φ_D is the implicitness parameter which depends on the local diffusion Courant number. For a fully explicit, Crank-Nicholson and fully implicit schemes, the implicitness parameters are $\Phi_D = 0, \Phi_D = 0.5$ and $\Phi_D = 1$ respectively.

$$M^B \frac{\widetilde{Y}_m^B - \widetilde{Y}_m^A}{\Delta t} = \sum_c \left(\frac{\mu_{eff}}{Sc}\right) \nabla \left(\Phi_D \widetilde{Y}_m^B + (1-\Phi_D)\widetilde{Y}_m^A\right)_c A_c^n \tag{5.8}$$

where c stands for control volume. A_c is the the normal vector which points in the direction of the outward facing cell face and its magnitude is equal to the area of the cell face. Any term of $\sum_c \left(\nabla \widetilde{Q}\right)_c A_c$ is computed by first calculating geometric coefficients a_{12}, a_{34}, a_{56} (see Figure 5.1 (right)).

$$A_c = a_{12}(x_1 - x_2) + a_{34}(x_3 - x_4) + a_{56}(x_5 - x_6) \tag{5.9}$$

where x_1 is the cell-center, x_2 is the cell-center of the neighbouring cell across the cell face, x_3 and x_4 are the centers of the opposite edges 3 and 4 , and x_5 and x_6 are the centers of the opposite edges 5 and 6. ∇ is the nabla operator which gives the gradient of a vector. Knowing A_c for any quantity saved in the cell center $\left(\nabla \widetilde{Q}\right)_c A_c$ is computed using Eq. (5.10).

$$\left(\nabla \widetilde{Q}_c\right) A_c = a_{12}(\widetilde{Q}_1 - \widetilde{Q}_2) + a_{34}(\widetilde{Q}_3 - \widetilde{Q}_4) + a_{56}(\widetilde{Q}_5 - \widetilde{Q}_6) \tag{5.10}$$

In original Kiva, Eq. (5.8) is solved for Y_m $m = 1, 2, 3..$ where these numbers indicate species, e.g. in a system that counts for only 5 species involving C_8H_{18}, O_2, N_2, CO_2 and H_2O the number of species is $m = 5$ and Eq. (5.8) is solved for $Y_{C_8H_{18}}$, Y_{O_2}, Y_{N_2}, Y_{CO_2} and Y_{H_2O}.

In this work, using a tabulated chemistry approach the species are not transported but the quantities Z, PV and EGR (see Eqs. (4.38), (4.37), (4.39)). These quantities are transported as regular scalars. Their transport equations have the same form as given for Y_m in Eq. (5.8) which turns automatically into a density weighted scalar transport equation for Z, PV and EGR. These might have source terms due to spray and heat release. In case that these scalars have source terms, they are then added as given in Eq. (5.7).

Energy

The first step of the energy calculation occurs in Phase A through a constant volume process, where the spray and chemical reaction sources are considered. In this work the source term for heat release $\dot{\omega}_{heat}$ due to chemical reactions is obtained from the look-up table.

$$\frac{M^A\tilde{e}^A - M^n\tilde{e}^n}{\Delta t} = V^n(\dot{\omega}_{\text{heat}} + \dot{\omega}_{\text{spray}}) \tag{5.11}$$

After adding the source terms arising from spray and heat release, the internal energy is updated to an intermediate state $\tilde{e}^t$, which accounts for enthalpy transport due to species. From this updated energy $\tilde{e}^t$ intermediate temperature $\widetilde{T}^t$ is solved implicitly using the relation given in Eq. (5.12).

$$\tilde{e}^t = \sum_m Y_m^B I_m(\widetilde{T}^t) \tag{5.12}$$

The quantities $e_m(\widetilde{T}^t)$ are obtained from JANAF [111] tables and stored in tabulated form at intervals of 100K. Now knowing $\tilde{e}^t$ and $\widetilde{T}^t$ the intermediate specific heat c_v^t is simply approximated by differences between adjacent tabular values of $e_m(\tilde{T}^t)$ using the relation $c_v^t = \partial\tilde{e}^t/\partial\widetilde{T}^t$.

In this work, a similar tabulation technique for internal energy is used within tabulated chemistry extended KIVA-4mpi (see section 4). However for the sake of simplicity, to be used in CAI engine simulations, the tabulation of internal energy is made only for averaged λ (=1.3) and averaged EGR (= 65%). These averaged values are given by experimentalists. For future work, the internal energy table should be extended to the relevant λ and EGR ranges.

The lagrangian step from the intermediate state to Phase B includes viscous dissipation terms and diffusion terms. They are then solved implicitly in Phase B (see section 5.2.1.1).

5.2.1.1 Implicit Phase B solution of coupled equations

In Phase B the coupled equations for velocity, pressure and internal energy (to determine temperature) are solved iteratively. The solution procedure is based on the SIMPLE algorithm [89, 88]. The species transport solved in Phase B is not a part of the to SIMPLE algorithm, since coupling relation between species and pressure is very weak.

Basically, the SIMPLE method is divided into two parts. The solution procedure starts with selecting a predicted value of Phase B. In the first part this predicted pressure field is frozen and the other flow quantities are calculated where the diffusion terms are differenced implicitly. In the second part of SIMPLE, these diffusion terms (calculated in the first part) are frozen and they are solved again with a corrected pressure. In the second part, equations for the cell-face velocity, the volume change a linearized state equation is solved simultaneously to get the relation between corrected and predicted pressure. In the following, the predicted and corrected pressure are compared. If the

difference is below a specified convergence tolerance, the equations have been solved and Phase C starts. In the original SIMPLE method, the convection terms are also differenced implicitly. However as already mentioned the convection terms of governing equations (2^{nd} terms on the left-hand side of governing equations) are not considered in Phase B within KIVA-4mpi. They are calculated in Phase C in a subcycled explicit fashion. In this section the solution procedure of the SIMPLE algorithm will be outlined briefly.

In order to determine the velocity field, the momentum equation is solved. Since in KIVA-4mpi the velocities are defined at vertices, the mass M_v is to be determined. This is done by adding mass contributions of cells M_c from each sharing the vertex according to

$$M_v = \sum_c \chi_c M_c \tag{5.13}$$

χ_c is the reciprocal of the distinct number of vertices a cell owns. Since a hexahedron grid is used in this work $\chi_c = \frac{1}{8}$. Using Eq. (5.13) the lagrangian discretized momentum is given in Eq. (5.14).

$$\begin{aligned}\frac{M_v^B \widetilde{u}_i^B - M_v^n \widetilde{u}_i^n}{\Delta t} = &- \sum_v \left[\Phi_P \overline{p}^B + (1-\Phi_P)\,\overline{p}^n\right]_c A_v^n + \\ &\sum_v \left[\mu_{eff}\left(\Phi_D \tilde{\tau}_{ij}^B + (1-\Phi_D)\,\tilde{\tau}_{ij}^n\right)\right]_c A_v^n - \\ &\sum_v N_P \frac{4}{3}\pi\overline{\rho}_d \left[\left(r_d^B\right)^3 v_{j,d}^B - \left(r_d'\right)^3 v_{j,d}'\right] + M_v^n g_j \ .\end{aligned} \tag{5.14}$$

where the sum over β_c is over all momentum facets corresponding to a given cell c and the sum over c is over all the cells which share the common vertex v. The third term on right hand of the Eq. (5.14) is the momentum transfer due to spray $\int_V \bar{\rho} f_i^s dV$ (see Eq. (5.5)). The quantities $r_p^{'}$ and $v_p^{'}$ stand for radius and velocity after droplet aerodynamic breakups, collisions and gravitational acceleration respectively. The terms r_p^B and N_p denote the droplet radius after evaporation and the number of droplets in a parcel [116]. Calculation of the contribution of this term S_v is also performed in Phase A.

The SIMPLE iteration is initiated with a predicted pressure $\bar{p}^p$ which is a extrapolated value from previous time steps:

$$\bar{p}^p = \bar{p}^{n-1} + \frac{\Delta t^n}{\Delta t^{n-1}}\left(\bar{p}^{n-1} - \bar{p}^{n-2}\right) \tag{5.15}$$

The Eq. (5.14) is reformulated by replacing $\overline{p}^B$ with $\overline{p}^p$ as follows

$$\begin{aligned}\left(M_v^B + S_v\right)\frac{\widetilde{u}_i^B - \widetilde{u}_i^A}{\Delta t} = &- \sum_v \left[\Phi_P \overline{p}^p + (1-\Phi_P)\,\overline{p}^n\right]_c A_v^n + \\ &\sum_v \left[\mu_{eff}\left(\Phi_D \tilde{\tau}_{ij}^B + (1-\Phi_D)\,\tilde{\tau}_{ij}^n\right)\right]_c A_v^n + M_v^n g_j \ .\end{aligned} \tag{5.16}$$

where S_v covers the spray contributions which is solved in Phase A and therefore known. For further information about spray and its contributions to momentum equation the reader is referred to [10, 116]. Φ_P is the implicitness factor same as Φ_D. The viscous stress tensor $\tilde{\tau}_{ij}$ involves the velocity gradients which are evaluated using the relation below:

$$\left(\frac{\Delta\tilde{u}_i}{\Delta x_j}\right)_c \approx \frac{1}{V_c}\int_{V_c}\frac{\Delta\tilde{u}_i}{\Delta x_j}dV = \frac{1}{V_c}\sum_c(\tilde{u}_i)_c A_c^n \tag{5.17}$$

Now knowing the terms, M_v^B, S_v, $\overline{p}^n$, $\overline{p}^p$, $\tilde{\tau}_{ij}^B$, $\tilde{\tau}_{ij}^n$ from Eq. (5.16) the velocity $\widetilde{u}_i^B$ can be calculated.

The viscous and dissipative terms of energy equation is solved to obtain the temperature $\widetilde{T}^B$ by

$$\begin{aligned} M^B\frac{\tilde{e}^B-\tilde{e}^t}{\Delta t} \approx -\frac{\bar{p}^B-\bar{p}^n}{2}\frac{V^B-V^n}{\Delta t} + \left(\Phi_D\left(\tilde{\tau}_{ij}\frac{\Delta\tilde{u}_i}{\Delta x_j}\right)^B + (1-\Phi_D)\left(\tilde{\tau}_{ij}\frac{\Delta\tilde{u}_i}{\Delta x_j}\right)^n\right)V^n \\ + \sum_c\left(\frac{\left(\bar{\mu}+\frac{c_v}{c_p}\mu_t\right)c_p}{Pr}\right)^n_c \nabla\left(\Phi_D\widetilde{T}^B+(1-\Phi_D)\widetilde{T}^*\right)_c A_c^n \end{aligned} \tag{5.18}$$

where $\widetilde{T}^*$ represents the sum of all heat contributions from Phase A up to this point (the last update state was the intermediate state t, see the internal energy calculations in section 5.2.1) and it is assumed that in the computational cycle it has occurred at constant pressure. The temperature change at constant pressure is equal to the enthalpy change:

$$\tilde{h}^t = \tilde{h}^n + c_p^n(\widetilde{T}^* - \widetilde{T}^n) \tag{5.19}$$

For constant volume and pressure $M^B\tilde{h}^t - M^n\tilde{h}^n = M^B\tilde{e}^t - M^n\tilde{e}^n$ and using the fact that $\tilde{h}^n = \tilde{e}^n + \bar{p}^n/\bar{\rho}^n$ one obtains for $\widetilde{T}^*$ by the following equation:

$$\widetilde{T}^* = \widetilde{T}^n + \frac{1}{c_p^n}\left[\tilde{e}^t - \tilde{e}^n + \bar{p}^n\left(\frac{1}{\bar{\rho}^A}-\frac{1}{\bar{\rho}^n}\right)\right] \tag{5.20}$$

Using the simplification $\tilde{e}^B - \tilde{e}^t \equiv c_v^t(\widetilde{T}^B - \widetilde{T}^t)$ and the equation of state for an ideal gas $V^B = \frac{M^B}{p^p}\bar{R}T^B$ in Eq. (5.18), the Phase B temperature $\widetilde{T}^B$ is solved by

$$\begin{aligned} \widetilde{T}^B = \Bigg\{\widetilde{T}^t + \frac{\bar{p}^p+\bar{p}^n}{2c_v^t}\frac{\Delta t}{M^B c_v^t}\Bigg[\sum_c\left(\frac{\left(\bar{\mu}+\frac{c_v}{c_p}\mu_t\right)c_p}{Pr}\right)^n_c\nabla\left(\Phi_D\widetilde{T}^B+(1-\Phi_D)\widetilde{T}^*\right)_c A_c^n + \\ \left(\Phi_D\left(\tilde{\tau}_{ij}\frac{\Delta\tilde{u}_i}{\Delta x_j}\right)^B + (1-\Phi_D)\left(\tilde{\tau}_{ij}\frac{\Delta\tilde{u}_i}{\Delta x_j}\right)^n\right)V^B\Bigg]\Bigg\} \Bigg/ \left\{1+\frac{\bar{p}^p+\bar{p}^{\bar{n}}}{2c_v^t\bar{p}^p\bar{R}}\right\} \end{aligned} \tag{5.21}$$

From Eq. (5.16) and (5.21) $\tilde{u}^B$ and $\widetilde{T}^B$ are obtained. Within the SIMPLE algorithm, which was initiated with the predicted pressure $\bar{p}^p$ (see Eq. (5.15)), $\tilde{u}^p$ is solved by replacing $\tilde{u}^B$ in Eq. (5.16). After this, from the Eq. (5.21) the predicted temperature $\widetilde{T}^p$ is calculated. Using the state equation predicted cell volume V_c^p is defined as

$$V^p = \frac{M^B}{\bar{p}^p} R\widetilde{T}^p \tag{5.22}$$

Supposing $\bar{p}^C$ is the corrected pressure, the corrected volume V_c^C is calculated with the cell face normal velocities $(\tilde{u}_i A_c)^C$, which correspond to the Lagrangian volume change (V^{LAG}). Details regarding the calculation procedure of the cell face normal velocities can be found in [116]. The cell face normal velocities are not only used to determine the volume changes due to vertex motion in Lagrangian stage, but they are also used later in the Eulerian stage (Phase C) to calculate the intermediate volume change during rezoning. The corrected volume V_c^C is given by

$$V^C = V^{LAG} = V^n + \Delta t \sum_c (\tilde{u}_i A_c)^C \tag{5.23}$$

The relation between V^p, V^C, $\bar{p}^p$ and $\bar{p}^C$ is given as follows

$$V^C = V^p - \frac{1}{\gamma} \frac{V^p}{\bar{p}^p} (\bar{p}^C - \bar{p}^p) \tag{5.24}$$

A pressure $\bar{p}^p$ is sought so that V^C and V^p agree to some tolerance $|V_c^p - V_c^C| \leq tol$. If this condition is not fullfilled the SIMPLE iteration will proceed further. Otherwise,the Eulerian stage (so-called Phase C) follows. Figure 5.3 summarizes the SIMPLE algorithm employed in Kiva which is coupled with the *conjugate residual method*. For details about the conjugate residual method the reader is referred to [42].

5.2.2 Eulerian stage

As already mentioned above, this stage is called Phase C in which the convective transport associated with the moving mesh is calculated. The flow filed is frozen and remapped onto a new computational mesh. This rezoning is done in a subcycled explicit fashion with a subcycle time step Δt_c. The Δt_c is a submultiple of the main computational time step Δt with the number of subcycles N_k

$$N_k = \frac{\Delta t}{\Delta t_c} \tag{5.25}$$

The time step Δt_c must fullfill the "Courant-Friedrich-Levy" (CFL) criterion $\frac{\tilde{u}\Delta t_c}{\Delta x} \leq 1$, which says that the magnitude of the expansion speed $\tilde{u}$ in a cell must be less than the ratio between grid resolution Δx and the time step Δt so that all temporal changes can be resolved.

The transport of the cell centered quantities is computed by using the volume δV_c which is determined by using the cell face normal velocity $(\tilde{u}_i A_c)^B$ calculated in the Lagrangian phase and the intermediate volume change δV_c^G. The intermediate volume change δV_c^G

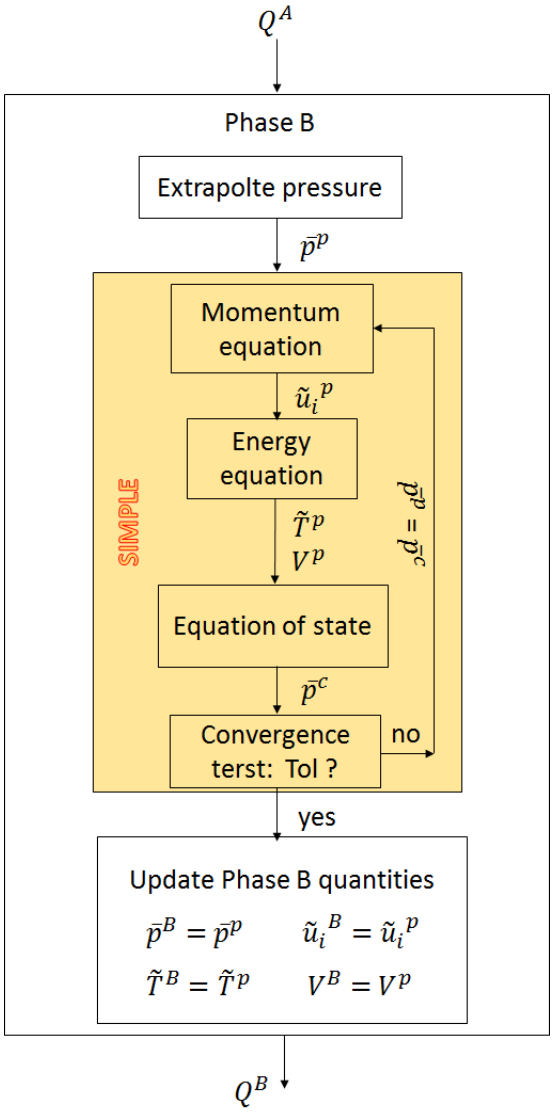

Figure 5.3: Solution procedure of Phase B (Simple Algorithm) (modified from [42]).

is the volume swept out by the cell face when vertices move from their old positions to their new positions from time point n to $n+1$:

$$\delta V_c = \delta V_c^G \frac{\Delta t_c}{\Delta t} - (\tilde{u}_i A_c)^B \Delta t_c \tag{5.26}$$

In the orginal Kiva version the convective subcycles for the species densities $\bar{\rho}_m$ are given with

$$(\overline{\rho}_m)^k V^k = (\overline{\rho}_m)^{k-1} V^{k-1} + \sum_c (\overline{\rho}_m)_c^{k-1} \delta V_c \,, \tag{5.27}$$

After solving Eq. (5.27) the total density $\overline{\rho}^k$ is determined by

$$\bar{\rho}^k = \sum_m \bar{\rho}_m^k \tag{5.28}$$

However, as already mentioned in section 5.2.1, within the tabulated chemistry approach used in this work, no equations are solved for partial densities of species from which total density could be obtained. Therefore, in Phase C an extra convective equation for the total density is solved.

$$(\overline{\rho})^k V^k = (\overline{\rho})^{k-1} V^{k-1} + \sum_c (\overline{\rho})_c^{k-1} \delta V_c \,. \tag{5.29}$$

The cell mass after k convective cycle is found by $M^k = \overline{\rho}^k V^k$ where

$$V^k = \left[kV^{n+1} + (N_k - k)V^B\right]/N_k \tag{5.30}$$

The vertex mass is determined as before in Eq. (5.13) by $M_v^k = \frac{1}{8}M^k$. Accordingly, the momentum, flux is determined by

$$(M_v\widetilde{u}_j)^k = (M\widetilde{u}_j)^{k-1} + \sum_c (\delta M_v\widetilde{u}_j)_c^{k-1} \;, \tag{5.31}$$

Similarly species transport (which in this work corresponds to scalar transport) and internal the convective terms are solve as given in Eqs. (5.32) and (5.32) respectively.

$$\left(\overline{\rho}\widetilde{Y}_m\right)^k V^k = \left(\overline{\rho}\widetilde{Y}_m\right)^{k-1} V^{k-1} + \sum_c \left(\overline{\rho}\widetilde{Y}_m\right)_c^{k-1} \delta V_c \,, \tag{5.32}$$

$$(\overline{\rho}\widetilde{e})^k V^k = (\overline{\rho}\widetilde{e})^{k-1} V^{k-1} + \sum_c (\overline{\rho}\widetilde{e})_c^{k-1} \delta V_c \,. \tag{5.33}$$

The temperature is $\widetilde{T}^{n+1}$ obtained from tabulated internal energies the same way as in Phase A (see section 5.2.1) and the pressure $\bar{p}^{n+1}$ is obtained from the state relation (see Eq. (5.22)).

In Kiva the cell face associated terms $(\overline{\rho})_c$, $\left(\rho\widetilde{Y}_m\right)_c$, $(\rho\tilde{e})_c$ and $(\tilde{u}_i)_v$ can be computed using Partial Donor Cell (PDC) or Quasi Second Order Upwind (QSOU). In this work, QSOU scheme is applied for the solution of these terms.

5.2.3 Time step control and convergence

During the Lagrangian stage, the diffusion terms are differenced implicitly. Therefore, during this stage the restrictions on Lagrangian time step are not based on stability but accuracy. There are several accuracy conditions to determine Δt.

$$\Delta t = min\left(\Delta t_{max}, \Delta t_{maxca}, \Delta t_{acc}^{n+1}, \Delta t_{rst}^{n+1}, \Delta t_{gr}^{n+1}\right) \tag{5.34}$$

First of all, maximum time step with unit second Δt_{max} and the maximum crank angle degree within one time step Δt_{maxca} are predefined in input file. The time step Δt_{acc}^{n+1} controls the maximum vertex movement in the Lagrangian stage given by

$$\Delta t_{acc}^{n+1} = \min_{i,j,k} \frac{f_a \Delta x_{i,j,k}}{|\tilde{u}_{i,j,k}^B - \tilde{u}_{i,j,k}^n|} \tag{5.35}$$

where f_a is a positive real number, which has the default value 0.5.

Another accuracy condition, which limits the amount of cell distortion that can occur due to mesh movement in Lagrangian phase is Δt_{rst}^{n+1} defined by

$$\Delta t_{rst}^{n+1} = \min_{i,j,k} \frac{f_r}{2\sqrt{\frac{\tilde{s}}{3}}} \tag{5.36}$$

where f_r is a positive real number similar to f_a.

Finally, Kiva attempts to increase the old time step. Thereby, Δt_{gr}^{n+1} limits the time step growing rate:

$$\Delta t_{gr}^{n+1} = 1.02 \Delta t^n \tag{5.37}$$

The subcycle time step Δt_c in Phase C is based on the Courant stability condition, which must be less than 1 for fully explicit solutions.

5.3 Boundary conditions

In order to solve the system of equations presented in the previous sections, both initial and boundary conditions are required. The properties of the flow field to be initialized are temperature, pressure, molecular weight and species mass fraction. From these information, the initial density is calculated. These initiations are made for each region, e.g., for engine simulations there are three regions, intake and exhaust ports and the cylinder. These properties can be initialized homogeneously or with stochastic fluctuations. The flow field velocity can be initialized with an expected stochastic distribution, which depends on the coordinate system or it can be set to zero.

There are two basic boundary conditions in Kiva namely rigid wall and periodic boundary conditions. Since in engine simulations rigid walls are employed, details this wall boundary conditions are given in this section.

The rigid walls involve several types depending on how velocity and temperature boundary conditions are set. The velocity boundary conditions on rigid walls can be *free slip* or *no slip*. The free slip condition denotes that the normal velocity of the medium is set equal to normal wall velocity and the other two tangential components of the velocity are specified explicitly. With no slip boundary conditions, fluid velocity on the wall is determined by the velocity of the wall i.e., for a fixed wall its value is set zero and for moving walls such as the piston and valves, it is determined by the piston and the valve speed. Temperature boundary conditions on rigid walls are based on the Dirichlet condition for fixed temperatures or in case of adiabatic walls, they are based on Neumann conditions, where heat flux normal to the wall is set to zero.

Also for the spray equation physical boundary conditions are needed. If a droplet impinges on a rigid wall, the velocity of the droplet is set to the velocity of the wall and there is no heat transfer between droplet and wall. For spray injector droplet mass flow rate and distribution of droplet sizes, velocities and temperatures are to be predefined.

In Kiva for engine simulations pressure boundary conditions are applied at the open borders of intake and exhaust port. One can set fix pressure magnitudes at the open borders of intake and exhaust ports which is physically not true or one can set pressure boundary conditions as a function of crank angle which is provided by experimentalist. These pressure values at intake and exhaust ports are then stored for given crank angle and used as Dirichlet boundary conditions.

5.4 Code performance

The code performance is highly limited due to the weak parallelization strategies of the KIVA-4mpi code. The first problem is the allocation of cells at the very beginning of a simulation. In KIVA-4mpi the initialization of the whole computational grid (typically 2.0 Mio cells for engine simulations) is performed on a single processor, which leads to RAM demand increase drastically.

The second problem arises due to *snapping calculations*. During a simulation within KIVA-4mpi, cells and nodes can become deactivated and activated (e.g. during compression, expansion). This process is called *snapping* in all Kiva codes and it is performed by gathering all the relevant information onto a root processor and performing the snapping calculations on the root processor. The information is then scattered back to the rest of the processors [117]. This problem is the reason for peaks of RAM demand during simulation.

The simulations of systems involving spray is already computationally expensive because for each droplet of the spray, additional variables are allocated such as density, temperature, radius, velocity in x-, y-, z- directions and many others. Additional to this high memory demanding nature of spray simulations, it is not optimal how KIVA-4mpi deals with the parallelization of spray particles. KIVA-4mpi handles the spray by associating each spray particle with the processor that owns the cell the spray particle resides within [117] which leads or might lead to disturbing load-balancing between processors.

Consequently, the KIVA-4mpi require very high RAM at the beginning of a simulation, during a simulation where snapping is performed and also in case of fuel injection.Due to these problems related to parallelization strategies of KIVA-4mpi, the number of CPUs to run parallel jobs and the number of cells are limited, which affects directly the quality of LES applications for complicated systems such as CAI engines.

In this work engine simulations are performed with 16 CPUs with a maximum memory demand of 64GB. For that purpose the computation nodes are used which involve

2×8=16 Intel(R) Xeon(R) CPU E5-2630 v3 @ 2.40GHz processors. The total memory of these nodes is 64 GB RAM plus 32 GB Swap. This exactly corresponds to the computational needs of CAI engine simulations. However using only 16CPUs and a relatively coarse mesh (see section 7.2), this requirement of RAM is extremely high. Therefore, for further work it is suggested to improve parallelization strategies of the KIVA-4mpi code. This would help to use computational resources more reasonable and also deliver more reliable LES results.

Chapter 6

Verification of ignition model

This chapter is devoted to the test cases for the verification of KIVA-4mpi coupled with tabulated chemistry, where results obtained from KIVA-4mpi simulations and detailed chemistry calculations are compared with each other. In the following, shown test cases are a homogeneous reactor and an one dimensional engine. The detailed chemistry calculations are performed by Dr.-Ing. Robert Schießl and Marc-Sebastian Benzinger from the Institute of Technical Thermodynamics (ITT) Karlsruhe.

6.1 Homogeneous reactor

For this test case, within KIVA-4mpi a model scenario is used for which the ignition model was designed, i.e., an adiabatic, isobaric, homogeneous reactor without diffusive transport. The ODE system used for detailed chemistry reactions which describes the homogeneous reactor is given in Eq. (6.1).

$$\begin{aligned} \frac{dPV}{dt} &= \frac{\dot{\omega}_{PV}}{\rho} \quad \text{with} \quad \dot{\omega}_{PV}(PV, Z, T_\mathrm{u}, p, EGR) \\ \frac{dZ}{dt} &= 0 \\ \frac{dT_\mathrm{u}}{dt} &= 0 \\ \frac{dp}{dt} &= 0 \\ \frac{dEGR}{dt} &= 0 \qquad . \end{aligned} \tag{6.1}$$

Here, it is necessary to remind the reader that here in this chapter the equations (cf. Eq. (6.1) or (6.2)) are not LES filtered. Since they are either 0- or 1 dimensional cases (see section 6.2) without turbulence.For homogeneous reactor simulations the instantaneous temperature $\tilde{T}$ changes only due to heat release, $\dot{\omega}_\mathrm{heat}$. This source term of heat release is obtained from the tabulated chemistry and within this simple but important test case, one can see, whether instantaneous temperature calculated within KIVA-4mpi matches with the detailed chemistry. Also this test case allows us to see how well ignition delay is captured with the reduced model in comparison to detailed chemistry.

6.1.1 Numerical setup

Homogeneous reactor simulations are *zero-dimensional* test cases and therefore it would be sufficient to perform these simulations within a single cell. However, due to the definition of boundary conditions within KIVA-4mpi, a mesh with $3 \times 3 \times 3$ control volumes is used. The spatial resolution has no effect on the results, since neither convection nor diffusion occur within the reactor. The boundary conditions are defined beside rigid walls with pressure inlet and outlet. The time step during the simulations are set to $\Delta t = 1 \cdot 1^{-7} s$.

The homogeneous reactor simulations are numerically difficult for KIVA-4mpi to realize. The reason for that is the spontaneous increase in temperature as the chemical equilibrium is almost reached, i.e., $0.8 \leq PV < 1.0$. Just before the state of chemical equilibrium, the highest amount of heat is released (ignition) which is responsible for instantaneous temperature reach to its final value (see Figure 4.10 in section (4.4.4)). At this very moment, a drastic change in temperature emerges which results in a spontaneous increase of pressure. The code tries to damp the pressure to its initial value as fast as possible but during damping the fluctuations in pressure are inevitable. Hence, at the moment chemical equilibrium is almost reached, pressure deviates from its pre-defined value. As a result, the homogeneous reactor condition being $\frac{dp}{dt} = 0$ does not hold any more.

Strength and duration of fluctuations depend on the magnitude of the source term for heat release (i.e., how strong an ignition process is). These fluctuations are observed mostly for cases without *EGR* where heat releases are relatively high. Here it is helpful to remind the reader of the comparison made in section 4.4.4 in Figure 4.10, which shows that at T_{u}=950K, $p = 25$ bar from 0% EGR to 60% the amount of maximum heat release increases by a factor of almost 30. During this damping procedure, pressure fluctuates until it is stabilized to its predefined value. These fluctuations in pressure show themselves in temperature and density. This is due to the coupled solution procedure of pressure, density and temperature in KIVA-4mpi.

As explained in section 4.5 the access variables χ_{PV}, $\chi_Z = Z_{stoi}/(Z_{stoi} + Z)$, $\chi_{T_u} = 1000/T_u$, $\chi_{EGR} = EGR$ and $\chi_p = log10(p)$ are updated with newly calculated PV, Z, T_u, EGR and p each new time step. According to the definition of a homogeneous reactor as given in Eqs. (6.1), these access variables must remain constant during the simulation. However as above mentioned, fluctuations in pressure and instantaneous temperature result in $\frac{dp}{dt} \neq 0$ and $\frac{T_u}{dt} \neq 0$ which lead to wrong table accesses. Therefore, for this test case, the access variables χ_{T_u} and χ_p are fixed to their initial values, i.e., they are not updated. Consequently, with this test case the calculation procedure of T_u cannot be verified but still temperatures at chemical equilibrium state and the ignition delays can be compared with detailed chemistry.

6.1.2 Results

The comparison between KIVA-4mpi and detailed chemistry are made for the engine relevant cases which are given in the table 6.1. These initial conditions were also used in section 4.4.4.1 where reaction trajectories were extracted from the look-up table by linear interpolation and compared with detailed chemistry results. There it was illustrated that reaction trajectories extracted from the look-up table deviate from detailed chemistry results. By this comparison the effects of these interpolation errors on ignition delay could not be shown because the reduced model is not parametrized with time t but PV. However, now by performing homogeneous reactor simulations within KIVA-4mpi, one can see the effects of these interpolation failures on temperatures at chemical equilibrium state (T_{eq}) and ignition delays (τ_{ign}).

Table 6.1: Initial conditions for homogeneous reactor simulations in figures 6.1, 6.2 and 6.3

$\mathbf{\Psi}_{0,i}$	λ	T_{u}(K)	p (bar)	EGR
$\mathbf{\Psi}_{0,1}$	1.0	930	22.4	65%
$\mathbf{\Psi}_{0,2}$	1.0	1017.5	32.4	65%
$\mathbf{\Psi}_{0,3}$	1.52	1017.5	32.4	65%

In figures 6.1, 6.2 and 6.3 results obtained from KIVA-4mpi (denoted as Kiva TC) and detailed chemistry calculations (denoted as DC) are shown for initial conditions $\mathbf{\Psi}_{0,1}$, $\mathbf{\Psi}_{0,2}$ and $\mathbf{\Psi}_{0,3}$ respectively. In the figures temporal development of temperature T (black), source term for heat release $\dot{\omega}_{\mathrm{heat}}$ (blue), progress variable PV (black) and source term for reaction progress $\dot{\omega}_{\mathrm{PV}}$ (blue) are plotted. Also the figures involve subfigures, where the evolution of source terms $\dot{\omega}_{\mathrm{heat}}$ and $\dot{\omega}_{\mathrm{PV}}$ are shown as a function of PV.

Generally, in figures 6.1, 6.2 and 6.3 outstanding shifts in temporal developments of source terms for heat release $\dot{\omega}_{\mathrm{heat}}$ and chemical reaction $\dot{\omega}_{\mathrm{PV}}$ are observed. This shifts can be easily related with the interpolation failure within tabulation which are illustrated by the comparisons between source terms $\dot{\omega}_{\mathrm{heat}}$ and $\dot{\omega}_{\mathrm{PV}}$ in PV space. Due to higher source terms $\dot{\omega}_{\mathrm{heat}}$ and $\dot{\omega}_{\mathrm{PV}}$ delivered by the look-up table, within KIVA-4mpi temperature is over predicted and ignition occurs earlier compared to detailed chemistry.

In Figure 6.2 one can see the fluctuations in temperature. The reason for this fluctuations is already explained above. Here one can see that the fluctuations have occurred for the case from which the highest heat is released: Since $\mathbf{\Psi}_{0,2}$ combines the best conditions to ignite, i.e, a higher T_u and a more convenient λ to ignite compared to $\mathbf{\Psi}_{0,1}$ and $\mathbf{\Psi}_{0,3}$ respectively.

To prove that this deviations in temperatures and ignition delays are caused by the interpolation failure, for initial condition $\mathbf{\Psi}_{0,3}$ a single trajectory is created with reduced model explicitly and it is coupled to KIVA-4mpi. The homogeneous reactor simulation

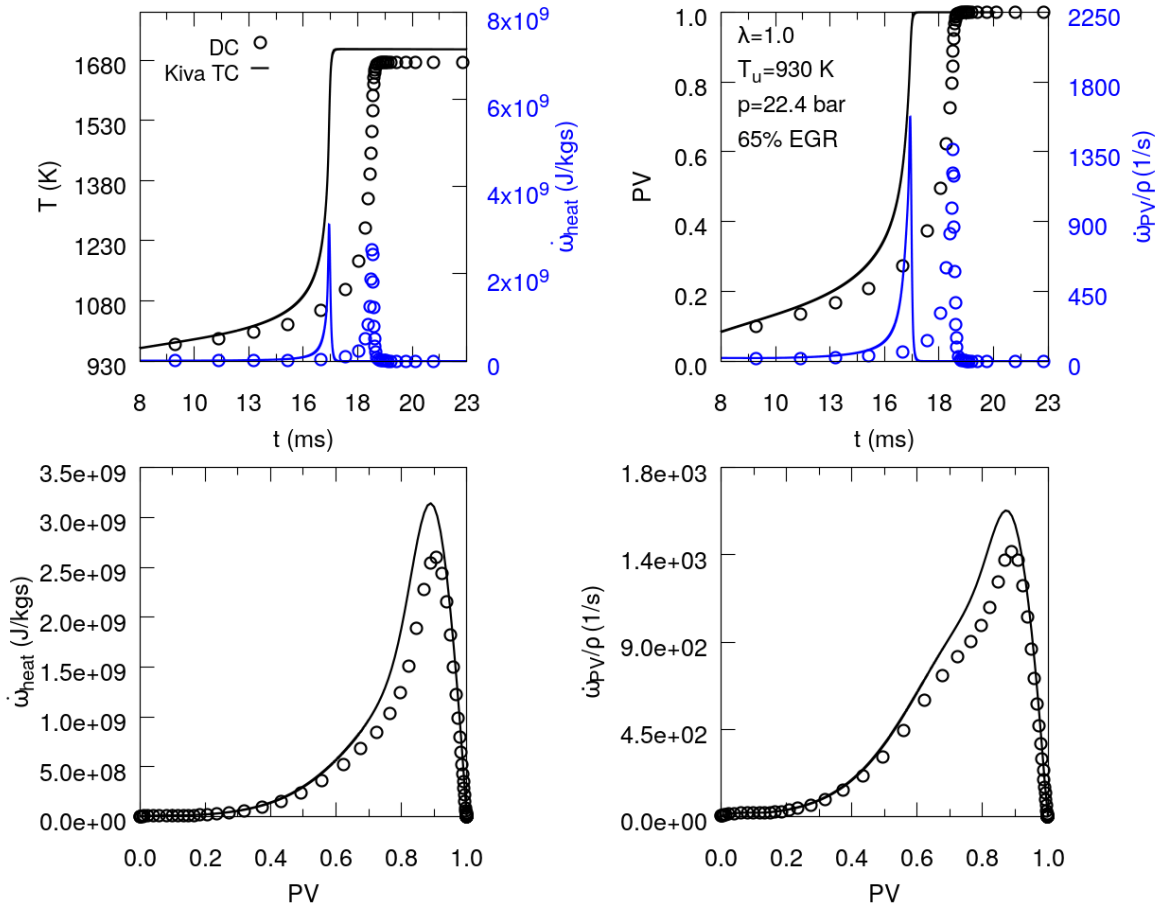

Figure 6.1: Homogeneous reactor simulations at $\lambda = 1.0$ $T_{\mathrm{u}} = 930K$, $p = 22.4$ bar and $EGR = 65\%$. Results obtained with 5 dimensional look-up table (Kiva TC) are compared with detailed chemistry (DC). The top left corner of the figure: Temporal development of temperature (black) and $\dot{\omega}_{\mathrm{heat}}$ (blue). The top right corner of the figure: Temporal development of PV and $\dot{\omega}_{PV}$ (blue). The bottom left and right corners of the figure: Illustration of $\dot{\omega}_{\mathrm{heat}}$ and $\dot{\omega}_{PV}$ in PV space, respectively.

with KIVA-4mpi at this initial condition is then repeated using this one dimensional look-up table (PV is the only access parameter). In Figure 6.4 detailed chemistry results are compared with both the results obtained from KIVA-4mpi simulations with multi-dimensional and one-dimensional look-up tables which are denoted as Kiva TC and Kiva TC2 respectively. From the results one can see that from KIVA-4mpi and detailed chemistry calculated temperature and ignition delay matches almost perfectly if one-dimensional look-up table is used, i.e., no interpolation in Z, T_u, EGR and p but in PV. Very small deviations are observed between DC and Kiva TC2 which is probably caused by interpolation in PV space and would disappear if PV resolution is increased.

With homogeneous reactor simulations, it turns out that the selected tabulation grid, in conjunction with the simple linear interpolation scheme for retrieving source terms $\dot{\omega}_{\mathrm{heat}}$ and $\dot{\omega}_{\mathrm{PV}}$, yields a shift in temporal evolution of temperature and progress variable PV. For the future work, one can use a more accurate interpolation scheme to over come

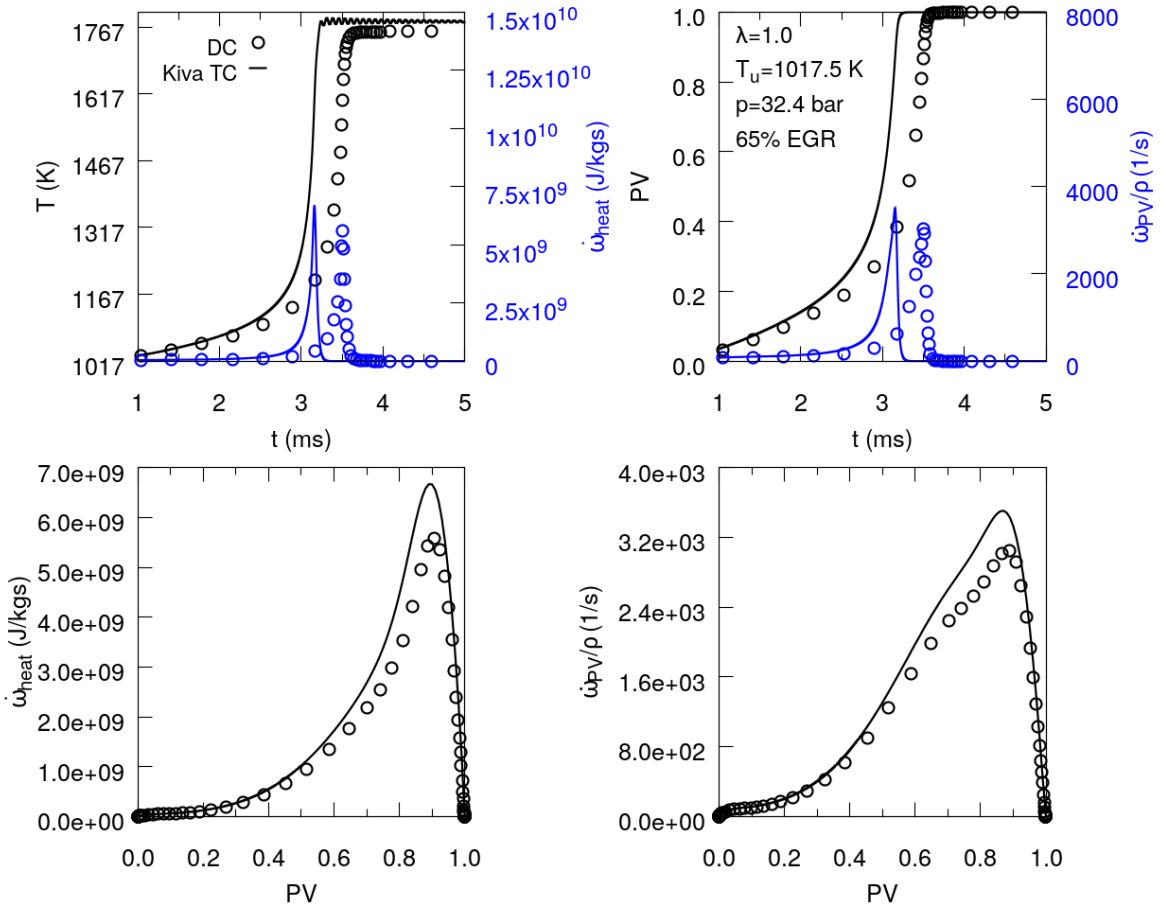

Figure 6.2: Homogeneous reactor simulations at $\lambda = 1.0$ $T_{\mathrm{u}} = 1017.5K$, $p = 32$ bar and $EGR = 65\%$. Results obtained with 5 dimensional look-up table (Kiva TC) are compared with detailed chemistry (DC). The top left corner of the figure: Temporal development of temperature (black) and $\dot{\omega}_{\mathrm{heat}}$ (blue). The top right corner of the figure: Temporal development of PV and $\dot{\omega}_{PV}$ (blue). The bottom left and right corners of the figure: Illustration of $\dot{\omega}_{\mathrm{heat}}$ and $\dot{\omega}_{PV}$ in PV space, respectively.

this problem. However such schemes are more complex and computationally more intense.

To conclude this test case, one can say that homogeneous reactor simulations are not completely appropriate to verify the coupling between tabulated chemistry and KIVA-4mpi. However for the cases where ignition is relatively weak, such as given in table 6.1, one can still use this test case with fixed access parameters χ_p and χ_{T_u} to see whether correct ignition delay and burnt temperature are obtained within KIVA-4mpi. Another important point is that these test cases were performed by transporting a *non-normalized* PV. In engine applications a normalized PV is transported and it is necessary to do all these test cases also by transporting a *normalized* PV.

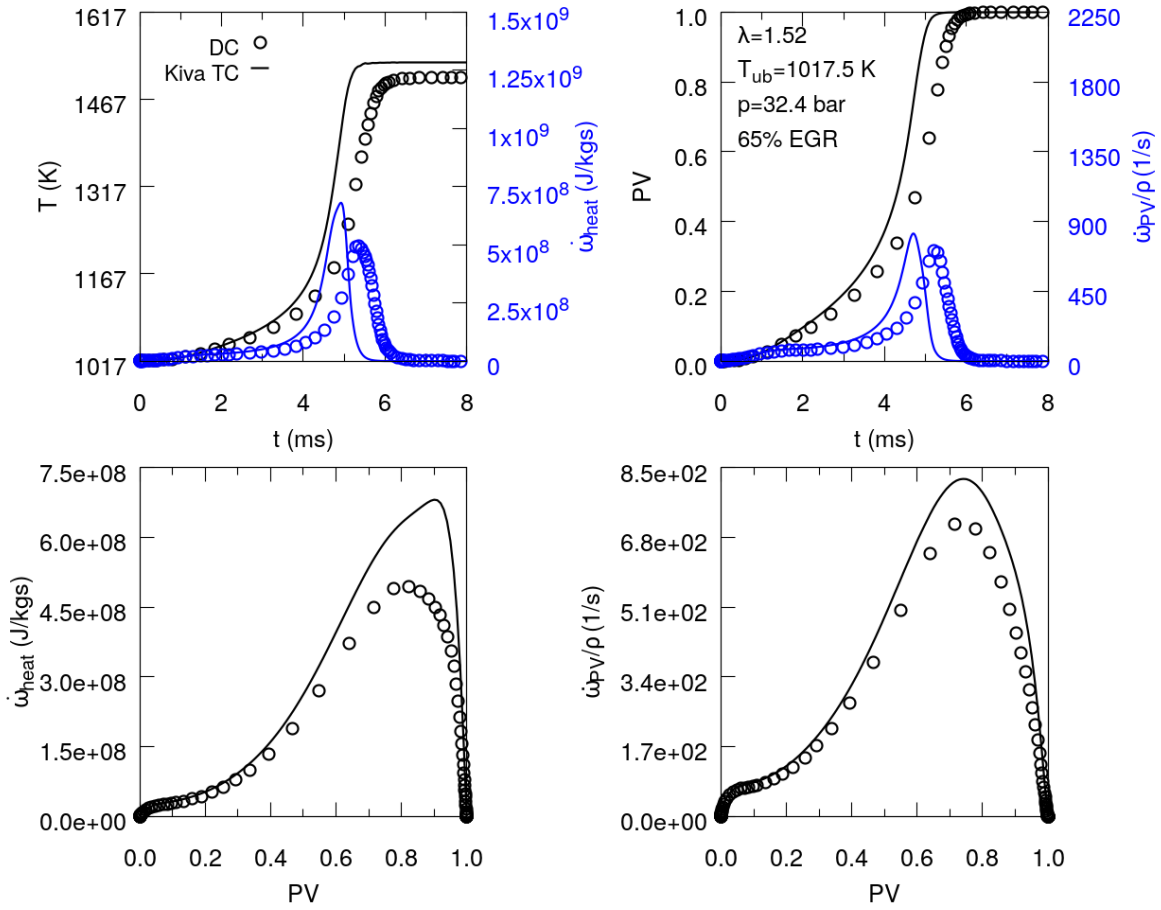

Figure 6.3: Homogeneous reactor simulations at $\lambda = 1.0$ $T_{\mathrm{u}} = 1017.5K$, $p = 32$ bar and $EGR = 65\%$. Results obtained with 5 dimensional look-up table (Kiva TC) are compared with detailed chemistry (DC). The top left corner of the figure: Temporal development of temperature (black) and $\dot{\omega}_{\mathrm{heat}}$ (blue). The top right corner of the figure: Temporal development of PV and $\dot{\omega}_{PV}$ (blue). The bottom left and right corners of the figure: Illustration of $\dot{\omega}_{\mathrm{heat}}$ and $\dot{\omega}_{PV}$ in PV space, respectively.

6.2 One dimensional (1d) engine

Another type of test can be performed by considering systems with unsteady thermodynamical conditions where enthalpy and pressure temporally varies. This kind of system does not physically match the conditions (isobaric-isenthalpic reaction trajectories) for which the tabulation was created. Benzinger studied in [14] the applicability of the model on engine-like systems where pressure/enthalpy varies with time. It was confirmed that the model still performs well also under these conditions, with deviations of ignition delay times from detailed systems that are typically lower than, for instance, deviations between detailed simulations of the same system based on different reaction mechanisms. Therefore, the reduced model still describes the system's evolution well. Here in this section an one-dimensional (1d) engine-like configuration (non-isobaric homogeneous reactor) is simulated using KIVA-4mpi with tabulated chemistry. The results are then compared with ones obtained from detailed chemistry calculations. The essential aim of

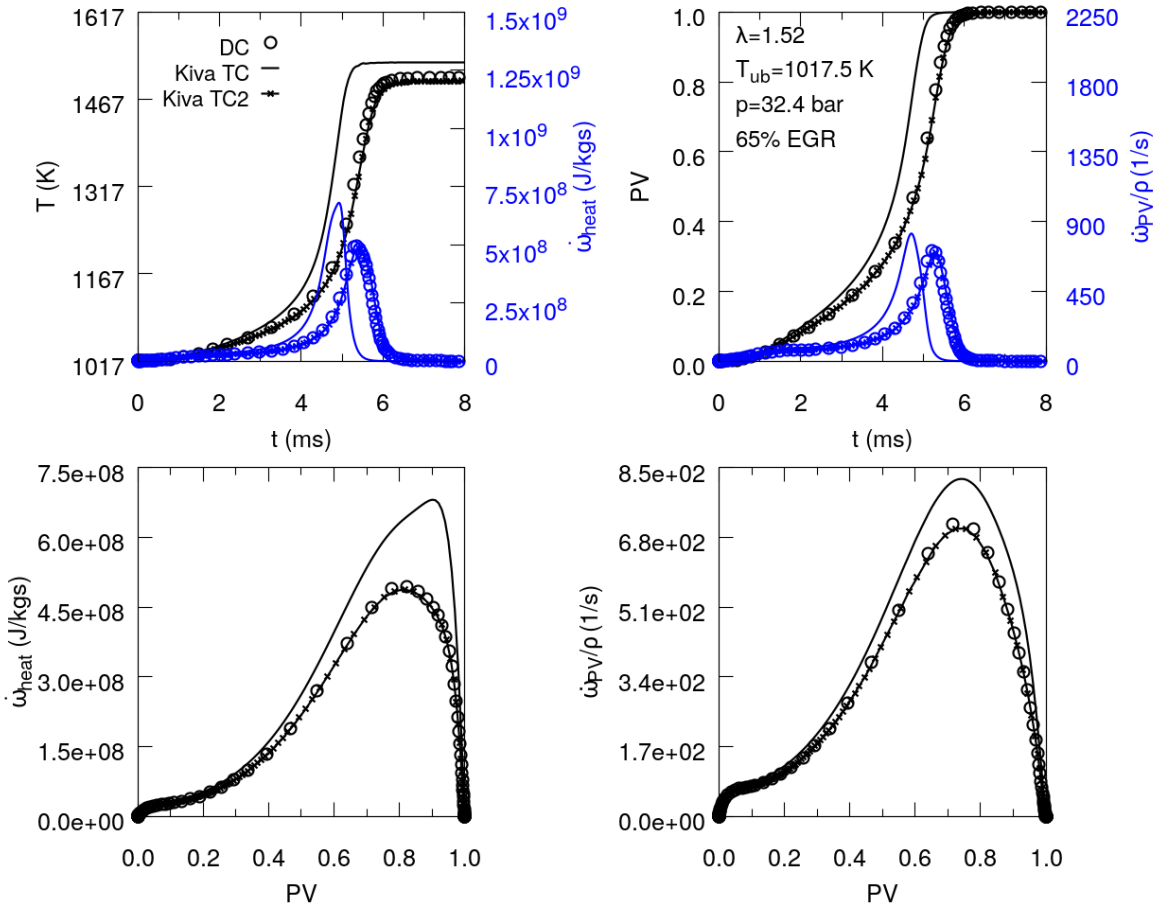

Figure 6.4: Homogeneous reactor simulations at $\lambda = 1.52$ $T_\mathrm{u} = 1017.5K$, $p = 32$ bar and $EGR = 65\%$. Results obtained with 5 dimensional look-up table (Kiva TC) and single trajectory table (Kiva TC2) are compared with detailed chemistry (DC). The top left corner of the figure: Temporal development of temperature (black) and $\dot{\omega}_\mathrm{heat}$ (blue) . The top right corner of the figure: Temporal development of PV and $\dot{\omega}_{PV}$ (blue). The bottom left and right corners of the figure: Illustration of $\dot{\omega}_\mathrm{heat}$ and $\dot{\omega}_{PV}$ in PV space, respectively.

this comparison is to verify the solution procedure of T_u which could not be verified by homogeneous reactor simulations as mentioned in the previous section.

6.2.1 Numerical setup

For KIVA-4mpi simulations the 1d engine-like configuration is created with a compression ratio of ϵ of 10.84 which is the same as the compression ratio of the simulated CAI engine in chapter 7.1. This 1d configuration is a simple closed system which is made for only compression of the medium at initial conditions. The moving rigid walls are adiabatic where no heat is transferred through the walls. For the test case a mesh with a spatial resolution $\Delta x_z = 1mm$ is used which is illustrated on the right side of Figure 6.5a. Resolution in other two directions Δx_x and Δx_y have no influence on results. They can

be seen as parameters to set the compression ratio to the desired value. The time step during the simulations are set to $\Delta t = 1 \cdot 1^{-7} s$.

The simulations are performed only from 20 cad before top dead center (TDC) and ends 30 cad after TDC. The solution procedure is described already in section 4.5.

For the detailed chemistry calculations of the 1d engine system the equations to be solved are given in Eqs. (6.2). To solve these equations the density history $\rho^*(t)$ must be predefined. $\rho^*(t)$ can be obtained for constant mass if volume-history $V^*(t)$ is known. This volume history here was observed from KIVA-4mpi simulations as given on the right side of the Figure 6.5b. $V^*(t)$ is known; for a constant mass, $\rho^*(t)$ is then also known.

$$\begin{aligned} \frac{dPV}{dt} &= \frac{\dot{\omega}_{PV}}{\rho} \quad \text{with} \quad \dot{\omega}_{PV}(PV, Z, T_\mathrm{u}, p, EGR) \\ \frac{dZ}{dt} &= 0 \\ p &= \rho^*(t) RT \\ \frac{dT}{dt} &= \dot{\omega}_\mathrm{heat}/c_p + p\frac{\dot{\rho}^*(t)}{\rho^*(t)^2} \\ \frac{dEGR}{dt} &= 0 \qquad . \end{aligned} \tag{6.2}$$

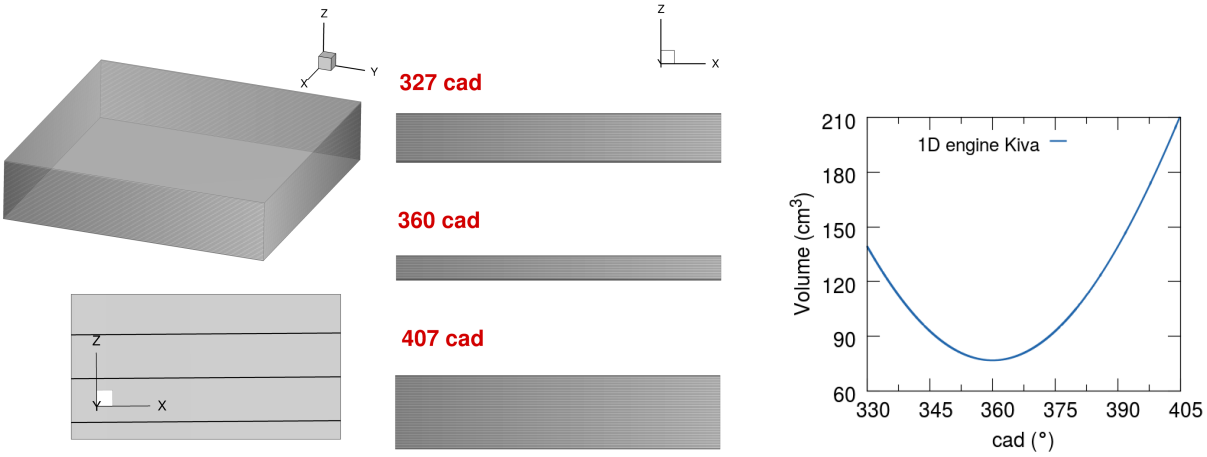

Figure 6.5: Left: Illustrution of 1d engine mesh and its movement from 327 cad to 407 cad. Right: From KIVA-4mpi observed volume curve to be used in detailed chemistry calculations.

6.2.2 Results

The comparison between detailed chemistry calculations and KIVA-4mpi simulations are illustrated in Figure 6.6 where the results from KIVA-4mpi and detailed chemistry are denoted with "KIVA-4mpi (TC)" and "DC" respectively. An arbitrary engine relevant

initial condition $\lambda = 1.0$, $T_u = 940$ K, $p = 13$ bar and $EGR = 70\%$ is chosen for the simulation. For this comparison an additional detailed chemistry calculation is performed with a $10K$ higher T_{u}. This means that the initial unburnt temperature of the second detailed chemistry calculation is $T_{\mathrm{u}} = 950K$. The results from this second detailed chemistry calculation is then denoted as "DC $(+10K)$".

On the left and right side of Figure 6.6 pressure and temperature developments within the 1d engine-like configuration are illustrated respectively. Between KIVA-4mpi (TC) and DC one observes small deviations. This deviations may occur due to different solution procedure of temperature and also due to interpolation inaccuracy clarified in section 6.1. Comparing KIVA-4mpi (TC) with DC, pressure and temperature curves match reasonably well with small deviations. Increasing the unburnt temperature T_u by 10K as in the detailed chemistry simulation (DC (+ 10K)), the deviations in curves disappear for both temperature and pressure. Such a 10K increase at 33 cad before TDC corresponds to a temperature increase of only about 4K at BDC which is well within typical experimental uncertainties.

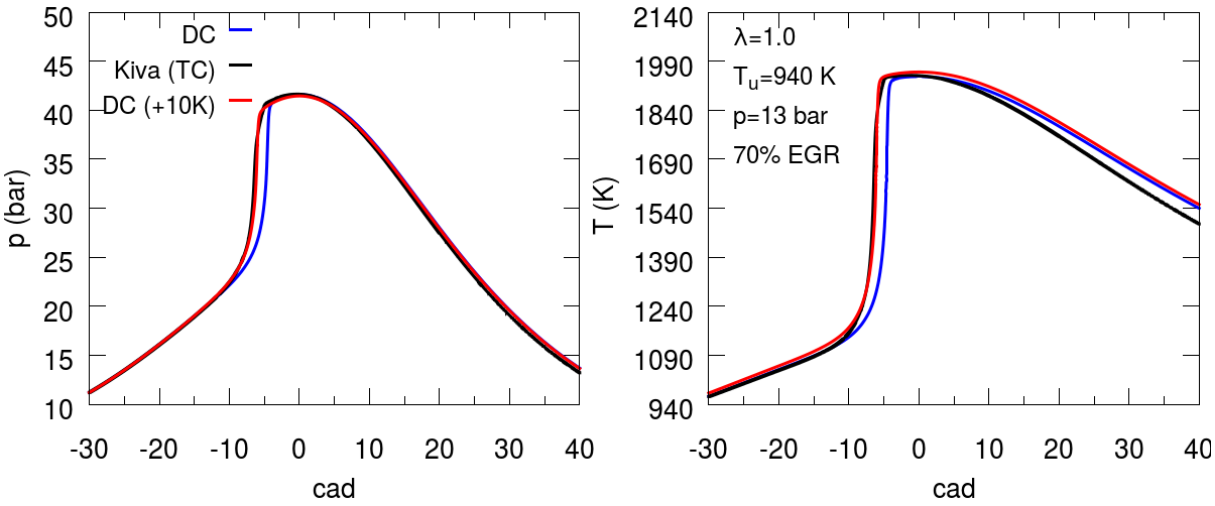

Figure 6.6: Comparison of 1d engine simulations with KIVA-4mpi using the tabulated chemistry approach (TC) with detailed chemistry (DC and DC+10K). Here DC +10K refers to 10K higher initial T_u. Evolutions of pressure and temperature are shown on the left and right sides of the figure, respectively [128].

This test case was performed by transporting a normalized PV and solving T_u as explained in section 4.5. The results obtained from the 1d engine simulation and also from systems with dissipative transport (shown in section 4.5.1) demonstrate that the solution procedure of KIVA-4mpi coupled with the reduced model is appropriate to be employed in CAI engine simulations.

Chapter 7

Simulation of a CAI engine

7.1 Experimental setup and configuration

The experiments are performed by Dipl.-Ing. Marius Neurohr at the Institute of Internal Combustion Engines, Karlsruhe Institute of Technology on a single-cylinder four-stroke direct injection (DI) gasoline engine (Fig. 7.1) with four canted valves, derived from a BMW F650 motorcycle manufactured by Rotax with several constructive modifications for numerous analyses. The valves located on the intake side of the engine have a curved bottom contour, whereas on the exhaust side the valves have an even bottom. The exhaust ducts are straight, whereas the intake ducts are straight only for the second half of the duct length. The maximum valve lifts are 0.186 cm and 0.137 cm for the inlet and exhaust valves respectively. In table 7.1 the geometric properties of the engine are summarized.

Two conventional hydrodynamic phase shifters for intake and exhaust are installed to regulate the residual gas fraction. Extensions of the camshafts are provided with an angle encoder brand while the Top Dead Center (TDC) signal is set to the maximum valve lift. In this way, the information about the phase position is available through the indexing system. The cam profiles are calculated with a 1D-simulation for a previously defined operating point at 2000 rpm with an IMEP of 2.0 bar.

A high pressure multihole injector HDEV5 from Bosch GmbH is placed centrally in the head of the cylinder with an installation angle of 18°. The injected fuel is EuroSuper with overall 84.1 mass-% carbon, 13.7 mass-% hydrogen and 2.2 mass-% oxygen. For the simulations *Toluene Reference Fuel* (TRF) is used, which consists of 85% iso-octane,

Table 7.1: Engine Configuration

Engine properties	Value	Unit
Bore	100	mm
Stroke	83	mm
Connecting rod length	149	mm
Rotational speed	2000	1/min
Compression ratio	10.84	(-)

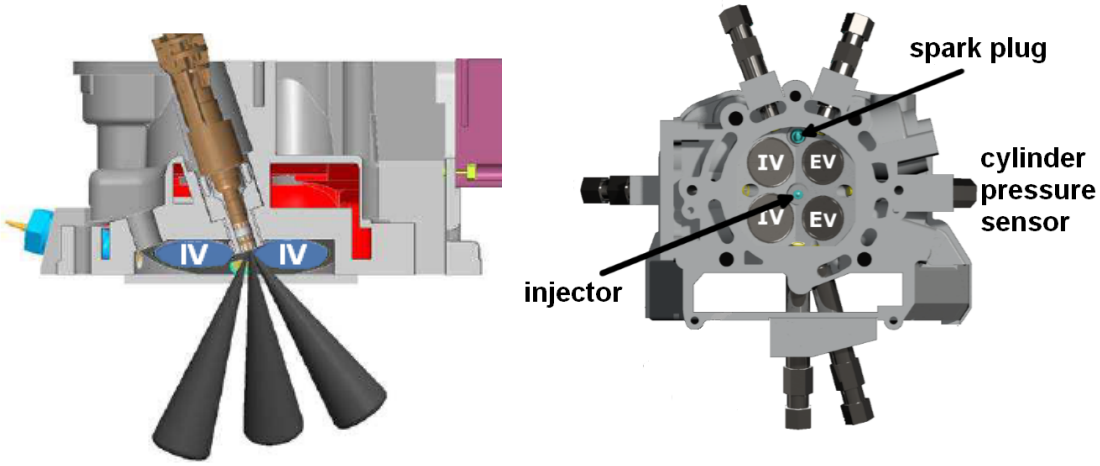

Figure 7.1: Left [68]: Injector installation of the test engine. Right [68]:Illustration of engine head.

5%n-heptane and 10% toluene (liquid volume %) and has the same Research Octane Number (RON) of 95 as the EuroSuper. The injected fuel mass is m_{inj} =1.05e-2 g at a temperature of T_{inj} =350 K. The initial droplet radius is $2.49 \cdot 10^{-4}$ m. The processes throughout a cycle will be illustrated in section 7.3.1.

A high-pressure sensor was adapted between the exhaust valves. The lateral spark plug visible on the left of Fig. 7.1 was needed just for starting operations. The cooling water and oil are set to 95°C with an external conditioning system. The intake air is also conditioned, the temperature is set to 25°C with a humidity of 35% and a pressure of 1050 mbar absolute. The air-mass was measured with a mass flow sensor from Bosch GmbH, the fuel mass is measured with a PLU121 from Pierburg. The air number λ is measured by an LSU4.9 from Bosch GmbH and additionally calculated from the measured exhaust emissions with the Brettschneider formula. The engine was also fully indicated, for intake and exhaust pressure an uncooled pressure sensor 4045 from Kistler is used. The in-cylinder pressure is measured with an uncooled 6054 sensor.

Based on 200 measured cycles the average *EGR* rate defined as already given in Eq. (4.29) in section 4.4 and has a value of approximately 65%. The valve timing for exhaust valves are varied during the experiments to trap the same amount of EGR in the cylinder for each cycle. This is calculated with an in-house pressure trace analysis tool at the institute of internal combustion engines. The calculations are done on single cycles, in which a savitzky-golay-filter is used to reduce signal noise, or on averaged pressure curves.

7.2 Computational domain and numerical setup

As shown in Figure 7.2 LES considers the complete geometry of the single-cylinder engine, including intake and exhaust ducts. The temperature and pressure of the intake and exhaust flow are measured where intake and exhaust ducts ends in Figure 7.2. These measurements are introduced as a function of crank angle and are used as boundary condition for the simulations. At all walls no-slip velocity boundary conditions are

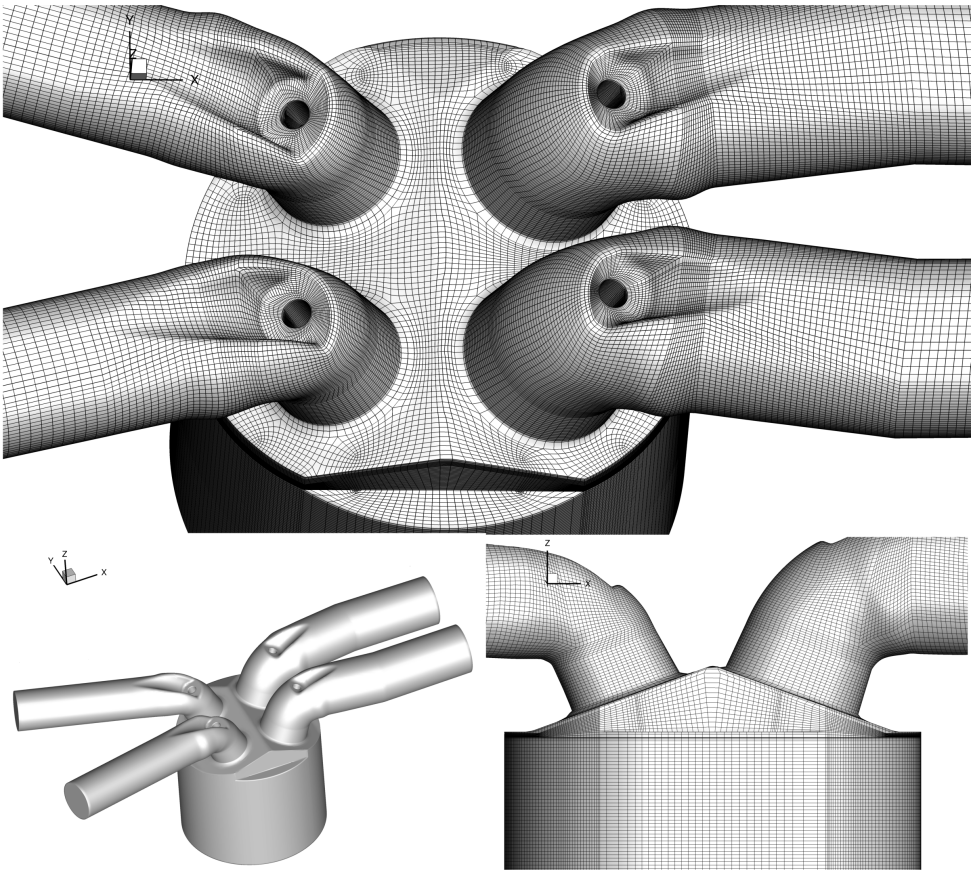

Figure 7.2: Illustration of the numerical domain

defined and no law of the wall is used. The temperatures of the cylinder wall are set to $T_{cw,epw} = 480\,\mathrm{K}$. For the intake duct walls and exhaust walls temperature of $T_{inw} = 317\,\mathrm{K}$ $T_{exw} = 640\,\mathrm{K}$ is specified respectively.

The injector is not reproduced in the engine geometry. Therefore one point is defined as injection point with properties of the injector. For spray injection a solid cone spray profile with a square wave injection pulse is specified. The description of the spray follows the discrete droplet model of Dukowicz [25] with Lagrangian, computational particles that represent parcels of spray droplets with uniform properties. The spray and fluid interactions are accounted for by means of a number of models that are well described in [10, 118].

The grid for the computational domain is a block-structured mesh with o-grids, containing 2.3 million cells in bottom dead center (BDC). The overall mesh size is of order $1\mathrm{mm} - 0.8\mathrm{mm}$. No special refinement of the grid near the walls is made. To solve in section 4.5 mentioned equations on moving grids, the ALE scheme is utilized in combination with a Semi-Implicit Method for Pressure Linked Equations (SIMPLE) algorithm and the conjugated residual method [116] (see section 5). For spatial discretization, quasi-second-order upwind scheme and for temporal discretization the Crank-Nicholson scheme is used. The time step is dynamically adjusted by several regulations like CFL-criteria or the given maximum mesh movement per time step and

is $3 \cdot 10^{-8}\,\mathrm{s} \leq \Delta t \leq 1 \cdot 10^{-6}\,\mathrm{s}$.

Two independent simulations are performed each 20 cycles. The combustion is very sensitive to the initial conditions of the simulations. The cycle to cycle variations for the first 10 cycles are very high. After 10 cycles the system reaches to a stable condition. For that reason, the results from last 10 cycles of each run are evaluated.

7.3 Results

This result presentation is divided into three parts. First, section 7.3.1 outlines the processes taking place throughout a typical cycle to provide a basic understanding. Then, in section 7.3.2 a detailed analysis is conducted to identify the thermal and mixing conditions that determine the auto-ignition. Finally, section 7.3.3 considers the interaction of consecutive cycles to explain the occurrence of cycle-to-cycle variations.

7.3.1 Cycle illustration and pressure curves

The illustration of a cycle is done by means of the global quantities depicted in Fig. 7.3 supplemented by the field quantities given in Fig. 7.4 and 7.5. The top of Fig. 7.3 shows the pressure evolution of a typical cycle spanning from -360<cad<360 (cad=crank angle degree) supplemented by the valve lift curves given in blue. For a better understanding of the process its preceding and subsequent cycle have been added with dashed lines. The process will be explained following the green numbered positions.

The first point at -500 cad represents the exhaust valve opened of the preceding cycle as given in the top row of Fig. 7.4. Before this opening, by definition, the cylinder contains only exhaust gas leaving through the valve. However, the valve timing is chosen such that a considerable amount of this exhaust gas remains within the cylinder for the next cycle being the reason why the explanation is started at this point. According to this early closing of the valve being 87 cad before the top dead center (TDC) a significant pressure increases follows. It is worth noting the strong inhomogeneity of the exhaust gas temperature shown in Fig. 7.4. Its causes are the combustion of different mixing conditions, locally different ignition histories as well as heat losses to the cold wall.

After the TDC one arrives at the second point being the fuel injection done at -300 cad (second row in Fig. 7.4). The liquid fuel is injected into the exhaust gases of the preceding cycle by a multi-hole injector. The droplets are indicated on the right of Fig. 7.4. Furthermore, the fuel mass fraction that already evaporated is given by the contours within the two slices. The middle column of Fig. 7.4 shows the ratio of *EGR*. One can see that the injection direction spreads the fuel mostly towards the positive x-direction. Likewise, the fuel injected at 350 K causes regions of low temperature visible on the right.

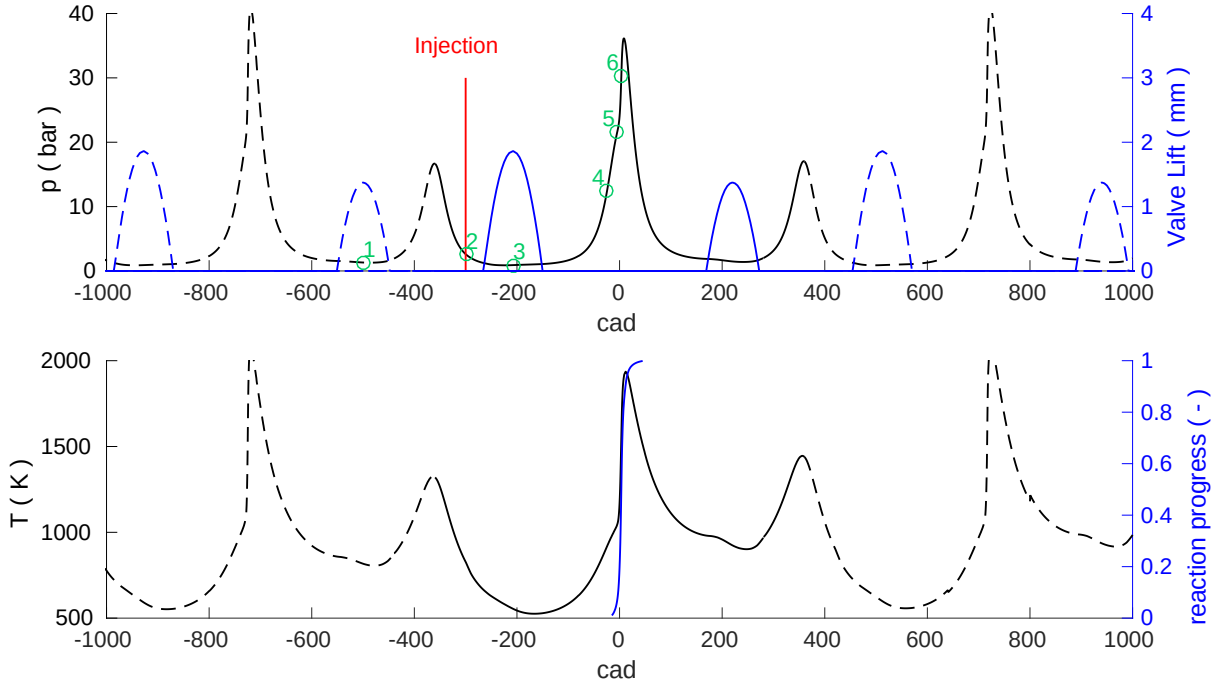

Figure 7.3: Evolution of the pressure (top) and temperature (bottom) for a typical cycle. The dashed parts indicate its preceding and subsequent cycle. Valve lift and reaction progress have been added on the right y-axis in blue to the upper and lower graph, respectively. Green points indicate position referred to in the text.

After this short injection phase the inlet valves are opened at point three. Pure air enters at 317 K leading to a further reduction of the *EGR* and the temperature. At this stage, the third row in Fig. 7.4 reveals certain similarities between the *EGR* and Temperature field. Even though there was little initial correlation (see top row), from this point on, the hot *EGR* is the dominating factor determining the temperature away from walls as will be detailed in the next section.

Going over to point four at -25 cad given in the first row of Fig. 7.5. On the left the air-number λ is introduced. From this moment on it provides reasonable values to visualize the mixing state. However, it is reconstructed based on the mixture fraction and since the exhaust gas contains unburnt oxygen it does not represent the actual air-to-fuel ratio. Accordingly, the stoichiometric ratio is shifted to lower values (i.e. below one) as it will be seen in the next section. With regard to this mixing state it is important to mention that all regions in the cylinder are within the flammability limits by now. This point can be considered as the pre-auto-ignition state. No ignition took place yet but the evolution of the combustion process is mostly determined by the conditions found here. Compared to point three, the *EGR* became more homogeneous by diffusion but still significant spatial variations exist (colormap has been rescaled compared to point three). The temperature increased significantly by the compression, still, it is insufficient for the auto-ignition.

Finally at point five (-5 cad) the first ignition spots visualized by the normalized reaction progress variable (PV) in Fig. 7.5 become visible. The EGR distribution is very similar and that's why it is stated that the process is mostly pre-determined by point four. From this moment on the processes take place in a very short amount of time. Accordingly, the mixing state is mostly frozen and the compression acts in increasing the temperature of these frozen states until sufficiently low ignition delay times are reached at some favourable positions.

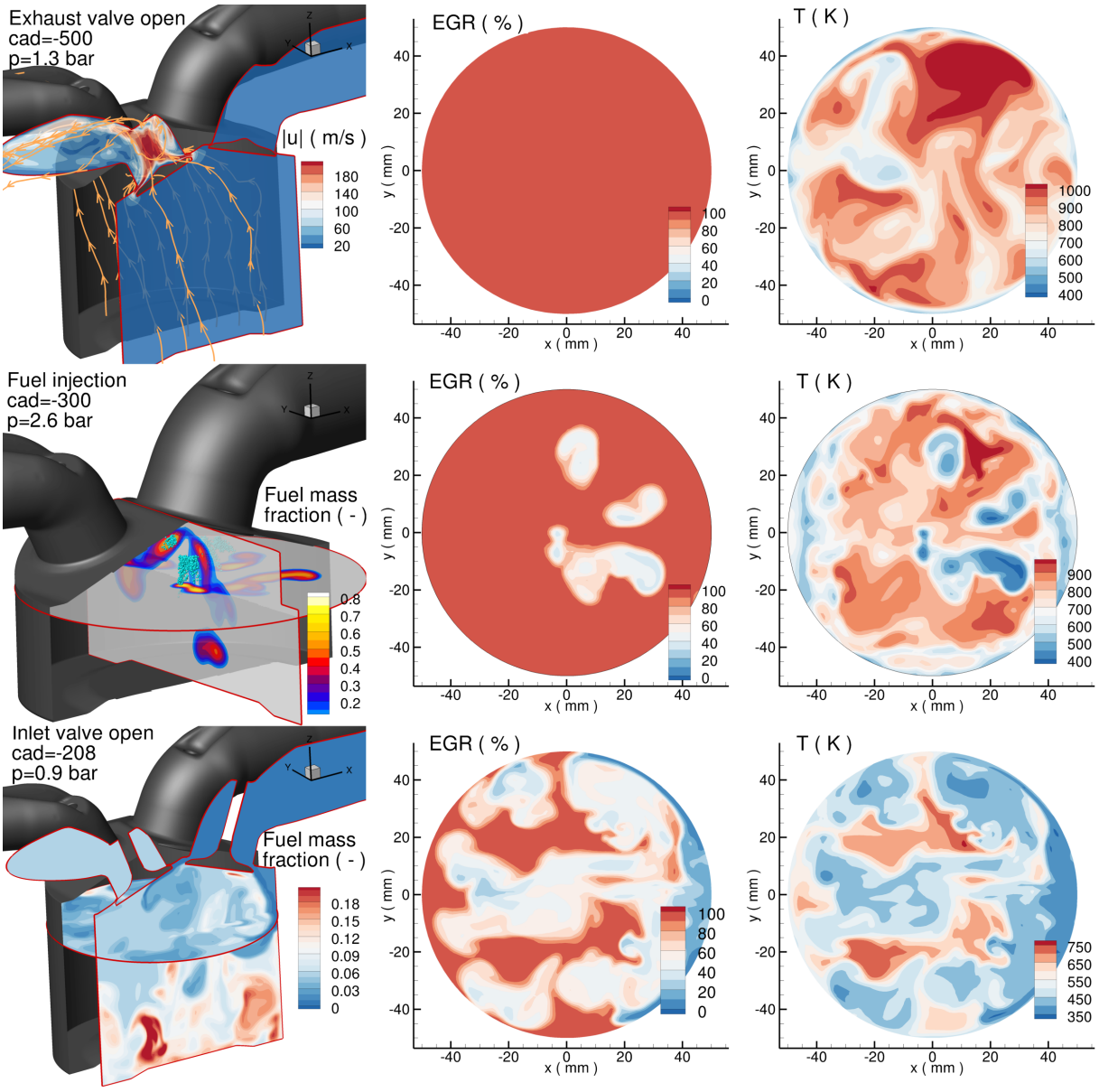

Figure 7.4: Visualization of the field at the instances 1-3 marked in Fig. 7.3. The left column shows a three-dimensional view of the cylinder outlining the physical process specifically corresponding to that instance. The middle and right column show the exhaust gas mass fraction and the temperature within a z-slice, respectively.

Point six being at 3 cad then describes a state where the combustion process is already well developed. The corresponding progress variable depicted on the right in the last row of Fig. 7.5 indicates that some regions are already fully reacted while numerous ignitions spots of intermediate states can be observed[2]. Compared to point five now the temperature shows larger variations being dominated by the combustion process and no longer by the ERG distribution. The combustion initially evolving only at the most favourable positions now increases the pressure such that also in the other regions

[2]Note that not all the regions represent independent spots as may be concluded from this two-dimensional view.

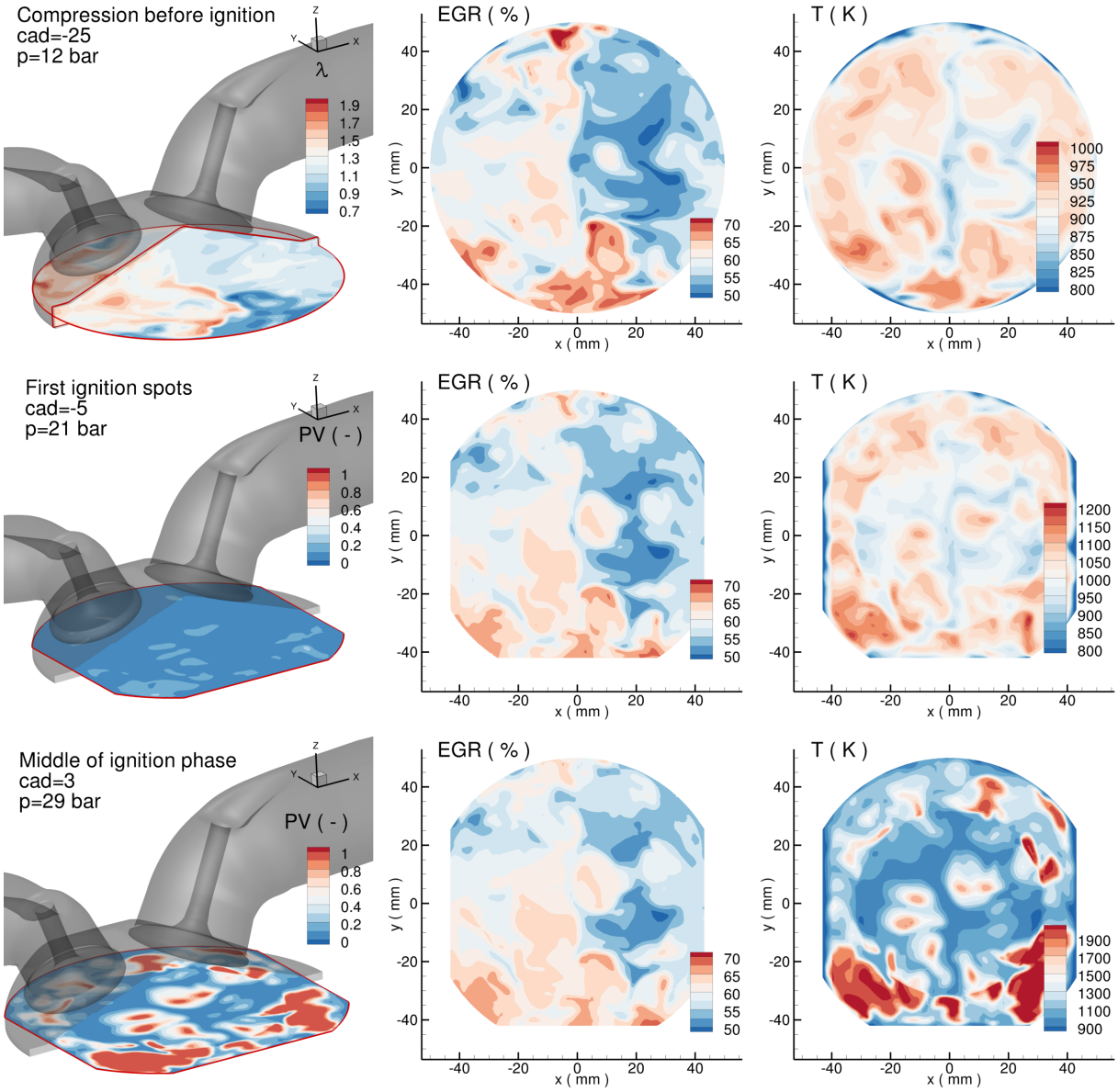

Figure 7.5: Visualization of the field at the instances 4-6 marked in Fig. 7.3. The left column shows a three-dimensional view of the cylinder outlining the physical process specifically corresponding to that instance. The middle and right column show the exhaust gas mass fraction and the temperature within a z-slice, respectively.

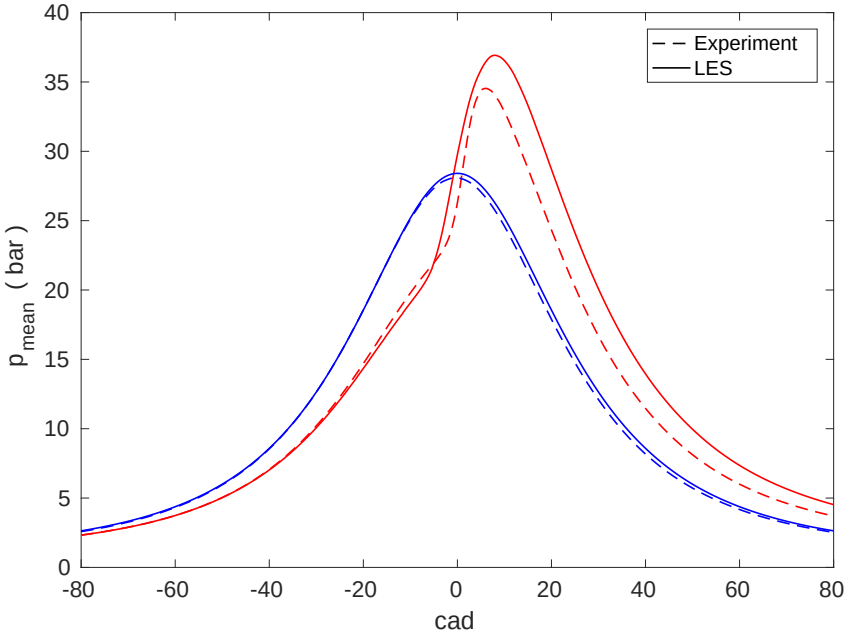

Figure 7.6: Averaged pressure for the motored (blue) and fired (red) mode of the LES in comparison with the experiment.

sufficient activation energy is present.

Figure 7.6 compares the phases averaged pressures predicted by the LES with the measurements. The motored case is also shown here to demonstrate that the numerical setup is suited for this configuration. Specifically, the pressure boundary conditions set in the inlet and exhaust pipes, together with the prescribed vale lift and piston movement lead to the correct trapped mass. These motored curves show the ordinary evolution imposed by the compression at which the LES and the experiment are in close agreement. It is noticeable that the pressure slope caused by the compression is larger than in the fired case. This is caused by the motored case having the larger trapped mass at which the hot exhaust gases of low density take up parts of the in-cylinder volume in the fired case. With combustion, the curves first evolve according to the compression followed by a distinct increase during the reaction. At this auto-ignition process differences in between the simulation and the experiments are visible. The slope during the combustion phase is actually in close agreement but the LES over-predicts the peak pressure by approx. 2 bar.

There are several reasons for the over predicted pressure by LES. First of all, due to high amount of trapped exhaust gas, the combustion depends highly on the initial setup of the simulation. The comparison between the initial conditions of both the experiment and the simulation would be helpful at this point. For the experiment during the first cycle fuel is injected in fresh air (without EGR) with an global λ value of 1.3 which led to a strong auto-ignition due to absence of EGR and it took during the experiment 50 cycles that the engine reaches a " stable condition " from where the statistical analyses were allowed to perform. Excluding these first 50 cycles, the engine run 200 cycles and the

averaged pressure curve was obtained as given in Fig. 7.6 . For LES calculations however, to save computational costs and due to the time limitations, the simulation was initiated from the exhaust stroke fully burned with a homogeneous temperature and mixture distribution. Within LES 20 consecutive cycles were simulated and averaged which is even less than the amount of excluded cycles (the first 50 cycles of the experiment) during the experiment. Hence, the comparison would be fair at least after simulation of 50 consecutive cycles.

Secondly, the averaged amount of the EGR during the experiment and the LES are different and have the value of 65% and 55% respectively. The less amount of EGR during the simulations leads to higher reactivity and also it results in a higher amount fresh air flow in cylinder. Increasing the reactivity and a higher amount of in-cylinder mass lead to higher peak and expansion pressures compared to experiment. The relation between the less amount of EGR and therefore higher in-cylinder mass after intake stroke is a very complicated mechanism and it will be explained in details in section 7.3.3. The local and global effects of EGR on ignition are different and this subject will be detailed in sections 7.3.2.2 and 7.3.3 respectively. However here it is important to point out why such a difference between the averaged amount of EGR within LES and the experiment occurs. One reason for that can be the initiation of the simulation as already mentioned above. Another reason is the different treatment of exhaust valve-timings during the LES and the experiment. The exhaust valve timing is decisive for the amount of the trapped gas and as already mentioned in section 7.1 during the experiment the exhaust valve timing was varied for each cycle to trap the same amount of exhaust gas for each cycle, with other words, the amount of EGR is controlled by varying the exhaust valve timing. However in LES calculations an averaged valve timing for the exhaust stroke is used, which was delivered by the experimentalists and therefore, in the LES the amount of EGR left in the cylinder could not be controlled (The cyclic variations in EGR are given later in section 7.3.3).

Another possible reason for the pressure difference in between LES and the experiment can be the treatment of the heat losses during the simulations. At near wall regions LES requires higher resolution or a special near wall model treatment [97] and both were not included in LES simulations which could possibly result in inaccuracies in heat loss calculations and therefore a pressure difference during combustion and expansion strokes.

7.3.2 Characterization of the inhomogeneities and their relation to the ignition behavior

The analysis is conducted in three steps. First, section 7.3.2.1 shows the ignition behavior of different temperature and mixing states. Section 7.3.2.2 then characterizes the inhomogeneities found at a certain cad within the engine. Finally section 7.3.2.3 then connects these findings to outline the combustion process of a cycle.

7.3.2.1 First view on the auto-ignition under different conditions

In this section the influence of different temperature and mixing states onto the ignition process are analysed. The significance of inhomogeneities within this engine is demonstrated in Fig. 7.7. First the pressure shown in the top is considered. The dashed curve represents a single (arbitrary) cycle taken from the simulation. Out of this cycle several spatial locations of different ignition quality as given by the mixture and temperature are selected, which are summarized in Table 7.2. The two cases with more and less favourable conditions are denoted by *strong* and *weak* , respectively. With these initial conditions a one-dimensional simulation featuring the same compression ratio but without heat losses has been performed. One further simulation has been performed with the conditions that would be present if the distribution within the real engine would be homogeneous (denoted by *hom*). All simulations start at -25 cad where the corresponding initial conditions have been taken from the real engine. As one can see in the top of Fig. 7.7 the pressure then increases equally for all simulations until a very early ignition is observed for the strong conditions. As expected it then follows the homogeneous simulation with a strong delay since its initial temperature is significantly lower. After that, the weak simulation reacts. Its initial temperature is equal to the homogeneous case but it has a less favourable mixing state given by λ. Not only the ignition delay is increased but also the time required for the reaction. This is visible in the second plot in Fig. 7.7 showing the reaction progress variable. The time required from the initial increase until the end of combustion is about twice for the weak case in comparison to the strong one. The real cycle evolves like a smoothened curve in between these conditions.

Finally, the lowest plot in Fig. 7.7 shows the ignition delay derived from the corresponding homogeneous reactor simulations, i.e. when freezing a certain state of T, EGR, λ, and p, an isenthalpic (isobaric and adiabatic) reaction would require this time to react. For the visualization this delay time is transferred into the cad, it would require at the 2000 rpm of the engine. According to this derivation, this delay time is not the one of the real engine but provides an idea whether the ignition can already evolve. In the initial state at -25 cad the delay is at least tens of degree, representing obviously insufficient conditions for the engine. The temperature increased by the compression then reduces this delay and when it approaches about 10 cad the delay time is in a comparable order with the engine relevant combustion range such that an increase of the progress variable can evolve. From this one-dimensional study the following can be concluded: First, the local inhomogeneities found within the real cylinder show significant differences in the ignition behaviour. Second, due to these inhomogeneities, the combustion evolves very smooth over a certain cad range within the real engine. Third, without these inhomogeneities, the operation mode would be less reliable. Considering that a rather strong cycle and adiabatic conditions for the one-dimensional piston were used, the ignition strength under homogeneous conditions may be insufficient for the real engine.

7.3.2.2 Spatial inhomogeneities at a given crank angle

This first view provided the information about the ignition behaviour of certain thermo-chemical states. The conditions used therein have been given as granted without

Table 7.2: Thermal and mixing states for the one-dimensional piston simulations.

	weak	hom	strong
T_u (K)	1013	955	955
λ (-)	1.344	1.157	0.835
EGR (%)	58	58	60.6

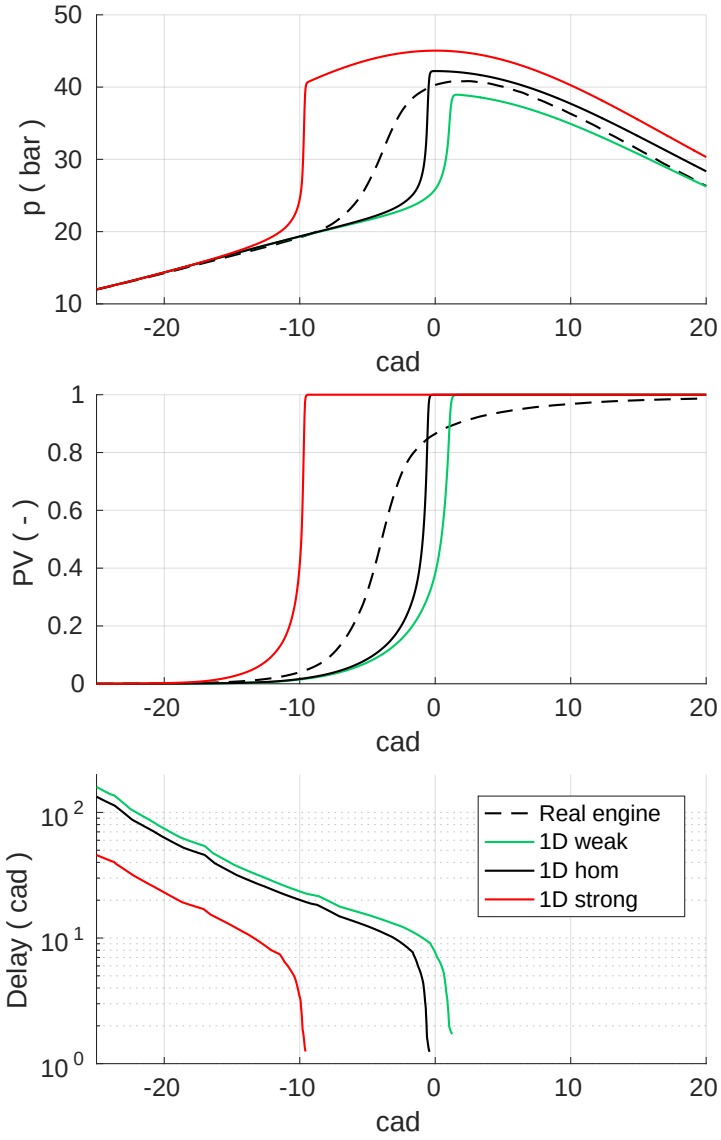

Figure 7.7: Results from the one-dimensional piston simulations. Evolution of the pressure, reaction progress and ignition delay for different thermal and mixing states as given in Table 7.2. The dashed curve is taken from the LES of the real engine.

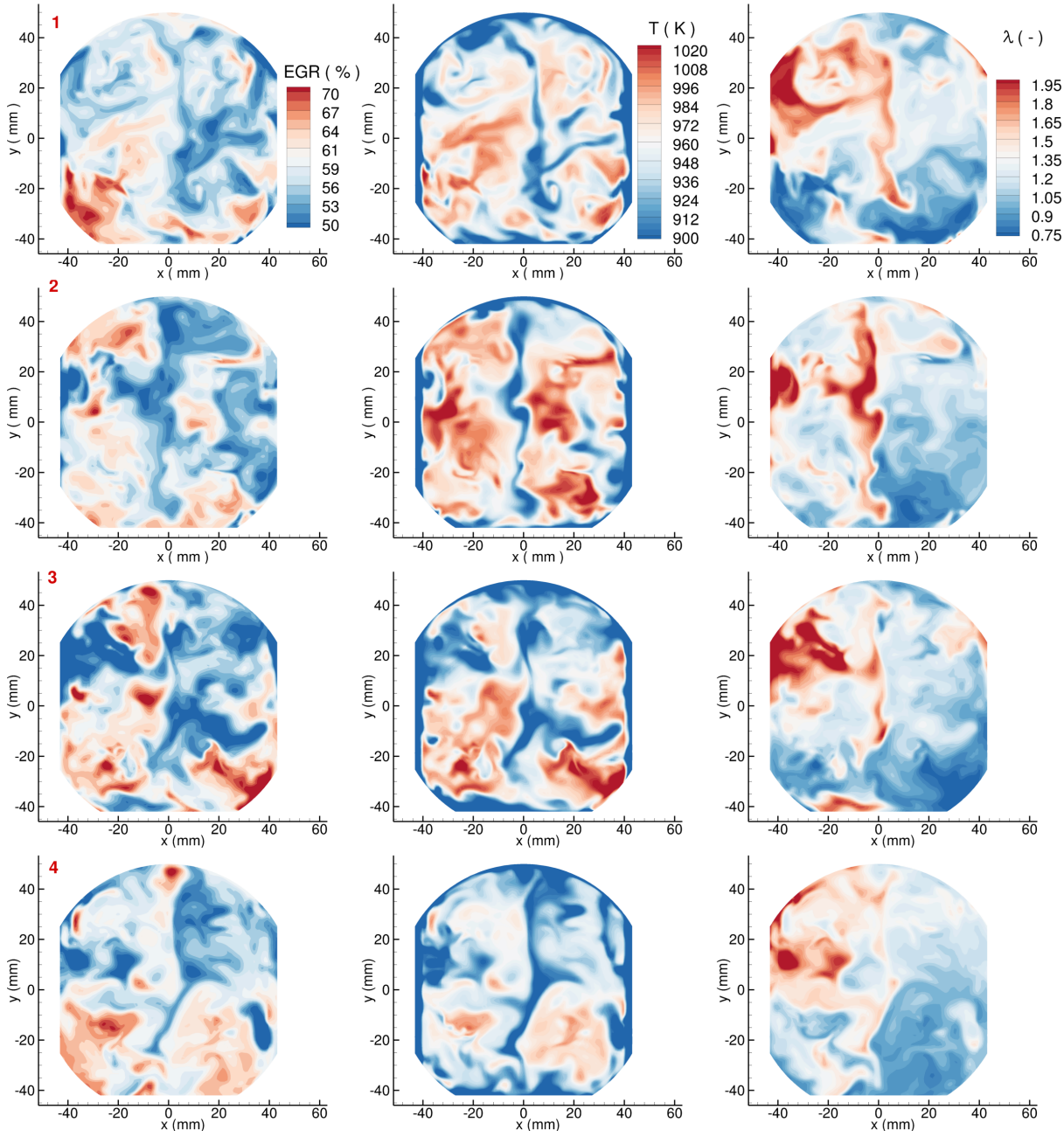

Figure 7.8: Snapshots showing the thermo-chemical state of different cycles at -25 cad within a z-slice.

explaining how the combinations of T_u, λ and *EGR* actually form. Therefore, as the next step in analysing the process, in this section it is aimed to characterize the spatial inhomogeneities. Figure 7.8 shows the scalar fields of four different cycles (subfigures 1 to 4) at -25 cad on the left and right, respectively. A similarity is the central vertical line of high λ and corresponding low temperature and *EGR*. It is visible more or less pronounced in all cycles and geometrically caused by the flow issuing through the inlet valve. However, except for this structure, the spatial distribution in between cycles is very different. Likewise, the occurrence of ignition spots is found at different spatial locations. In Figure 7.9 the positions of ignition kernels with a PV threshold

being $PV = 0.1$ are illustrated for each 20 cycles. With the contour colours the crank angle degrees are represented at which the first ignition kernels ($PV = 0.1$) occur. In the figure from 1 to 4 enumerated ignition kernels belong to the cycles illustrated in Figure 7.8 (subfigures 1 to 4). From Figure 7.9 one can observe that for each cycle, the first ignition kernels occur at different positions (they mostly occur close to intake valve in negative y-direction) and crank angles. The cycle to cycle variation of the ignition delay (here it is defined as $PV = 0.1$) is stronger compared to the cycle to cycle variation of kernel positions. As mentioned in the previous section the ignition is strongly linked to the scalar field. If conditioned on this latter the cycles show identical behaviour. Furthermore, as already indicated, the scalars are not independent from each other which will be quantified in the following for representative cycles.

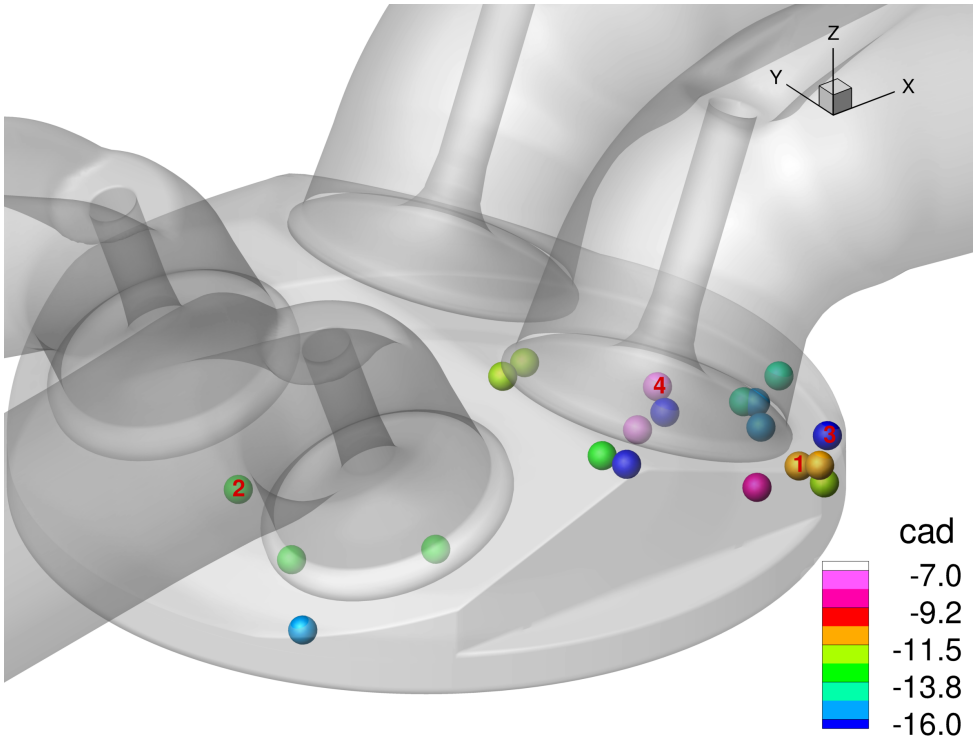

Figure 7.9: The first occurance (cad with contour colors) and positions of the ignition kernels with threshold PV=0.1 for each 20 cycles.

The left of Fig. 7.10 shows the joint probability density function (pdf) of T and *EGR* found within a slice at -25 cad where a clear correlation can be observed as it was very clear for all cycles. As indicated it is caused by the high temperature of the *EGR* as illustrated on the left of Fig. 7.11. Here one can see the strong alignment of the temperature field with the *EGR* lines. The *EGR* lines are colored to provide the information that high *EGR* levels are associated with a high temperature and vice versa. As expected there is one exception of this correlation: At boundaries the temperature is reduced by the heat flux into the wall (see left and right border) which does not affect the EGR. This region has been removed for the samples entering the pdf in Fig. 7.10 but the influence was not significant.

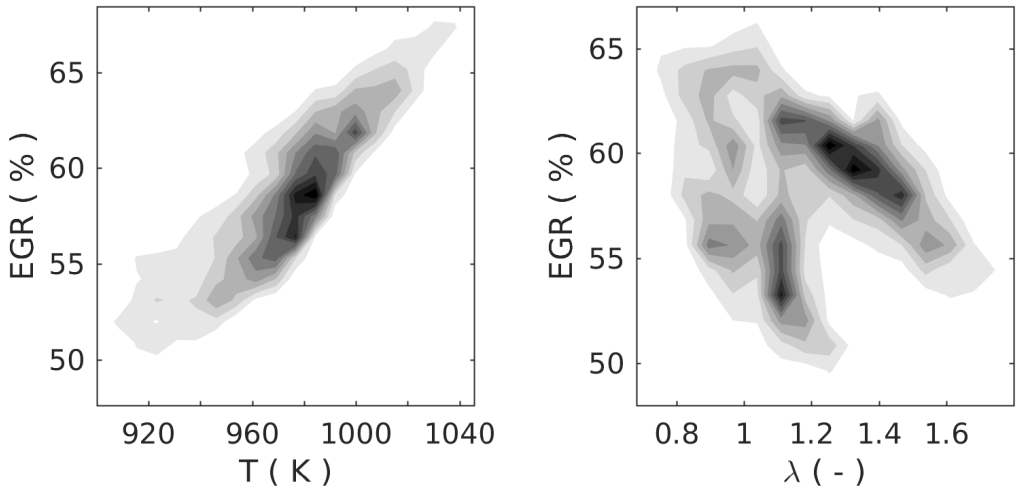

Figure 7.10: Joint pdfs at -25 cad. Wall regions have been excluded.

Next the joint pdf of λ and *EGR* shown on the right of Fig. 7.10 with the corresponding field shown on the right in Fig. 7.11 is considered. The pdf shows two distinct branches. Those where not always that distinct as the one shown but existed for all cycles. Their physical significance is explained on the left of Fig. 7.11. First one can see the diagonal branch where the *EGR* drops with increasing λ. It simply results from mixing where the fresh air entering the intake increases λ and reduces *EGR*. Accordingly, low *EGR* values are associated with a high λ as visible in most of the top left region of the slice. One extremum is marked by the circle 1 where the spatially lowest *EGR* rate and highest λ are found. The second branch shows a reduction of the *EGR* and constant λ. This is caused by mixing of air and *EGR* as well. However, here also additionally fuel is entered into the mixture such that λ remains constant while *EGR* significantly reduces. Such a situation is marked by circle 2 in Fig. 7.11. Specifically in this region, the *EGR* changes strongly from 50% to 60% while λ is literally constant.

Now one has a good understanding on how certain states form so the next step is to link them to the ignition. Figure 7.12 shows the ignition delay as derived from isenthalpic simulations. For this given pressure corresponding to the one found at -5 cad it is a function of *EGR*, λ and T. The dependencies are clear and expected: First, the delay decreases strongly with the temperature due to the exponential link of the reaction to the temperature by the Arrhenius law. Second, the delay increases with *EGR* since it mostly consists of inert products that reduce the reactivity. Third, the excess in oxidizer causes the delay to increase with λ.

This would suggest that for example a high temperature and a low *EGR* provide good ignition conditions. However as one knows from their correlation in Fig. 7.10 such conditions do not exist in the engine. In Fig. 7.13 the pdf of the states found in the engine is superimposed onto the thermochemical states determining the ignition delay. Regarding this delay, the increasing *EGR* and T have opposed effects but one

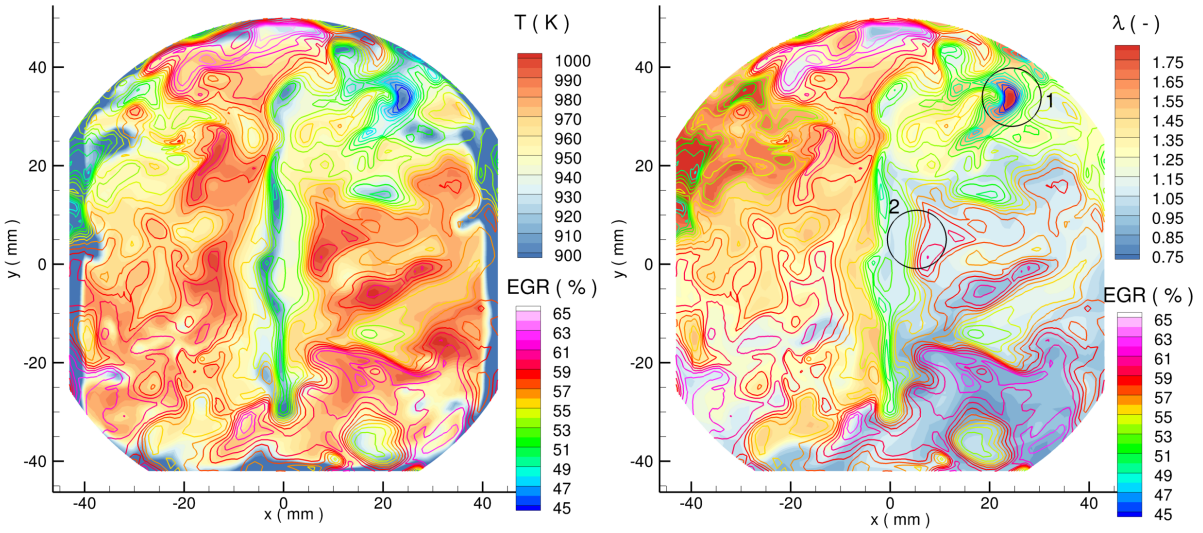

Figure 7.11: Slice illustrating the scalar alignment of *EGR* (lines, rainbow colormap) with the temperature (left) and λ (right). Circles mark positions referred to in the text.

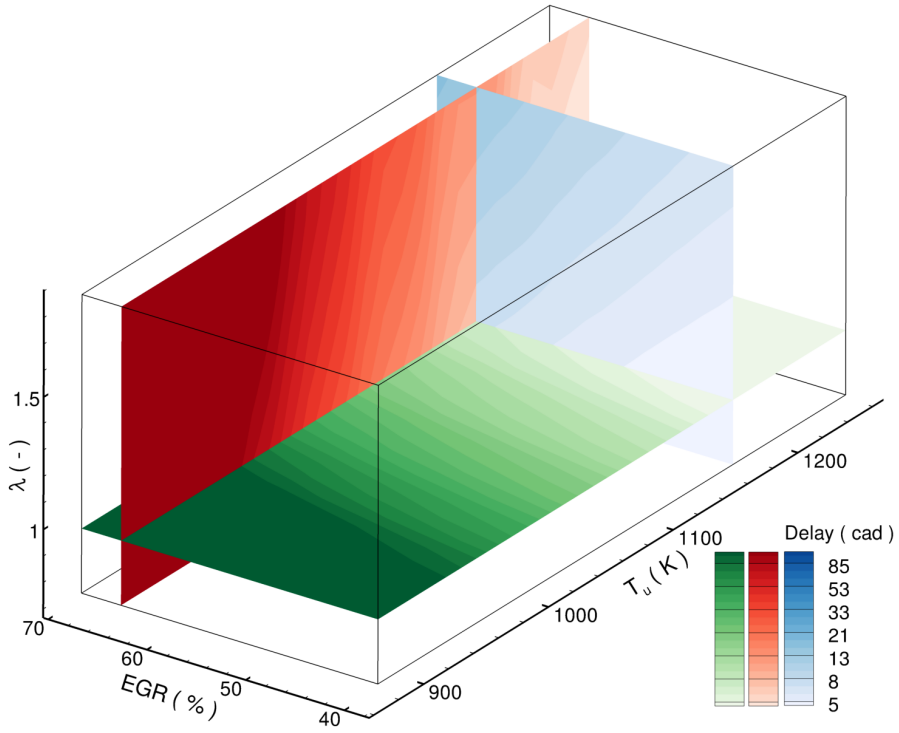

Figure 7.12: Ignition delay for 20 bar derived from a series of isenthalpic homogeneous reactor simulations.

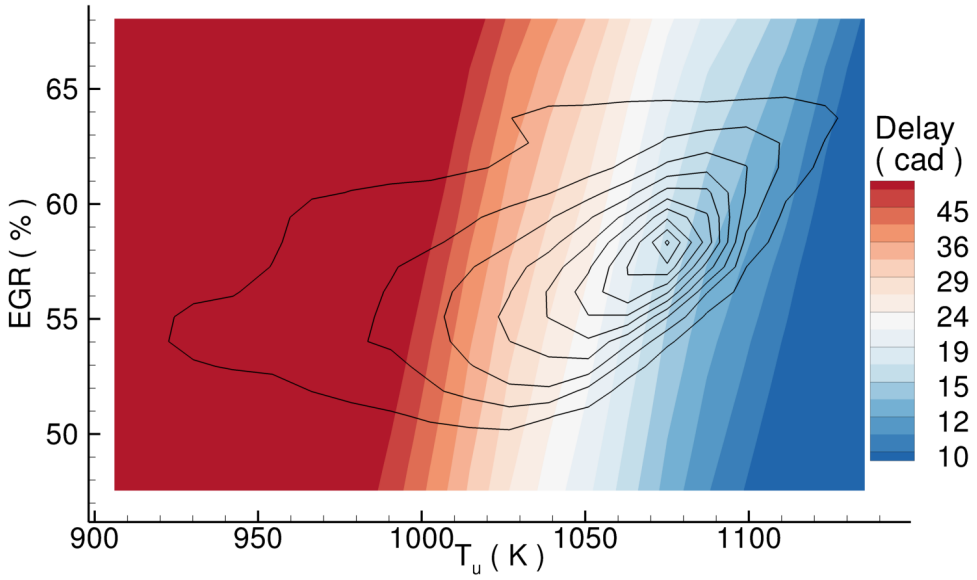

Figure 7.13: Joint pdf of T_u and *EGR* found within the engine at -10 cad (onset of ignition) superimposed onto the ignition delay of the corresponding thermo-chemical state. Wall regions are included in the pdf.

can see, that the slope is such that their correlated increases evolves with a slope leading to an overall decrease of the ignition delay. The pdf shown here is taken from -10 cad to show realistic delay times. Furthermore, wall regions have not been excluded for this pdf do show that some regions of exceptionally low temperature exist. Excluding these low values influenced by heat losses, throughout the slope of the pdf the ignition quality varies from about 40 cad to 10 cad for this crank angle. This is a first strong indicator that the combustion process gets determined by this distribution.

To supplement this assumption, one can make one further step. The top left of Fig. 7.14 shows again the pdf of T and *EGR* but with normalized coordinates. Here the *Heating-Coordinate* is introduced, which is given by the red arrow. It represents a joint coordinate linearising the dependency of *EGR* and *T*. The *Heating-Coordinate* is obtained by performing a simple linear regression analysis of the pdf of normalized *EGR* and *T* being EGR_n and T_n respectively (Fig. 7.14 top left). General formulation of the obtained regression line is given as follows:

$$EGR_n = \beta_0 + \beta_1 T_n \tag{7.1}$$

where, β_0 and β_1 are the offset and slope of the regression line (*Heating-Coordinate*) respectively. For each cycle this analysis delivers different values of β_0 and β_1, i.e. different *Heating-Coordinates*. Surely, one could perform here instead of linear regression analysis, a conditional mean value analysis $< EGR|T >$. However, due to the absence of statistically sufficient data, the results from conditional mean value analysis $< EGR|T >$ would be staggering. Additionally, as illustrated in Figures 7.10 and 7.14 the pdfs of EGR and T show a very clear linear dependency and therefore linear regression analysis of the pdf of EGR and T was found to be appropriate.

The *Heating-Coordinate* has a certain error (all deviations from this line) but it allows to reduce the three dimensional state description f(T,EGR,λ) to a two-dimensional f(*Heating-Coordinate*,λ) one to ease further insight. Accordingly the delay given in Fig. 7.12 reduces to a slice being given in the middle left in Fig. 7.14. Here one can see that the major factor is the preheating but also, that for a given value of this preheating the local air number λ can then have a certain influence.

The top right of Fig. 7.14 shows the joint pdf of the *Heating-Coordinate* and the ignition delay. They are indeed strongly linked. The two plots below show the average values of λ and the *EGR* superimposed onto this pdf. These contours show that variations orthogonal to the evolution are associated with variations in λ while the *EGR* is aligned rather parallel to the *Heating-Coordinate* which confirms its derivation. So far the analysis only showed a certain ignition likeliness. The proof, that these conditions are actually determining the combustion process is given in the bottom left of Fig. 7.14. Since a cad is chosen, where first slight ignition spots already formed, it is possible here to demonstrate that a clear dependency of the reaction progress to the *Heating-Coordinate* exist.

7.3.2.3 Process throughout the full cad range to outline the course of the combustion process

From the analysis of the last section one could see that strong spatial inhomogeneities exist. It is showed that a preheating by *EGR* takes place along a trajectory in the thermo-chemical space which it is termed the *Heating-Coordinate*. Due to its slope it is the main vector determining ignition. A certain scatter orthogonal to this coordinate exists which is mostly caused by variations in λ. The analysis was conducted for a given crank angle and holds for all cycles. Within this section to complete the picture, the full evolution of the combustion process throughout a cycle is considered .

First the combustion process is followed as monitored at the five points marked in Fig. 7.15, each of them characterizing one of the typical evolutions found. The variables found at these points is provided in Fig. 7.16 as a function of the cad being detailed in the following according to their number:

1. The first point is the earliest to ignite. One can see that it has a high initial temperature, a corresponding high *EGR* and a rather low λ at onset of ignition. Accordingly, its ignition delay is very short.

2. This point is close to point one but ignites independent. It has a comparable evolution but all ignition favoring parameter are just a bit lower and accordingly its reaction process is delayed.

3. The third point is an example where good conditions are countered by heat losses to the walls. It is positioned within the gap at the cylinder walls and from its temperature and progress variable evolution one can see that the reaction gets slowed down despite an initially high temperature, *EGR* and low λ.

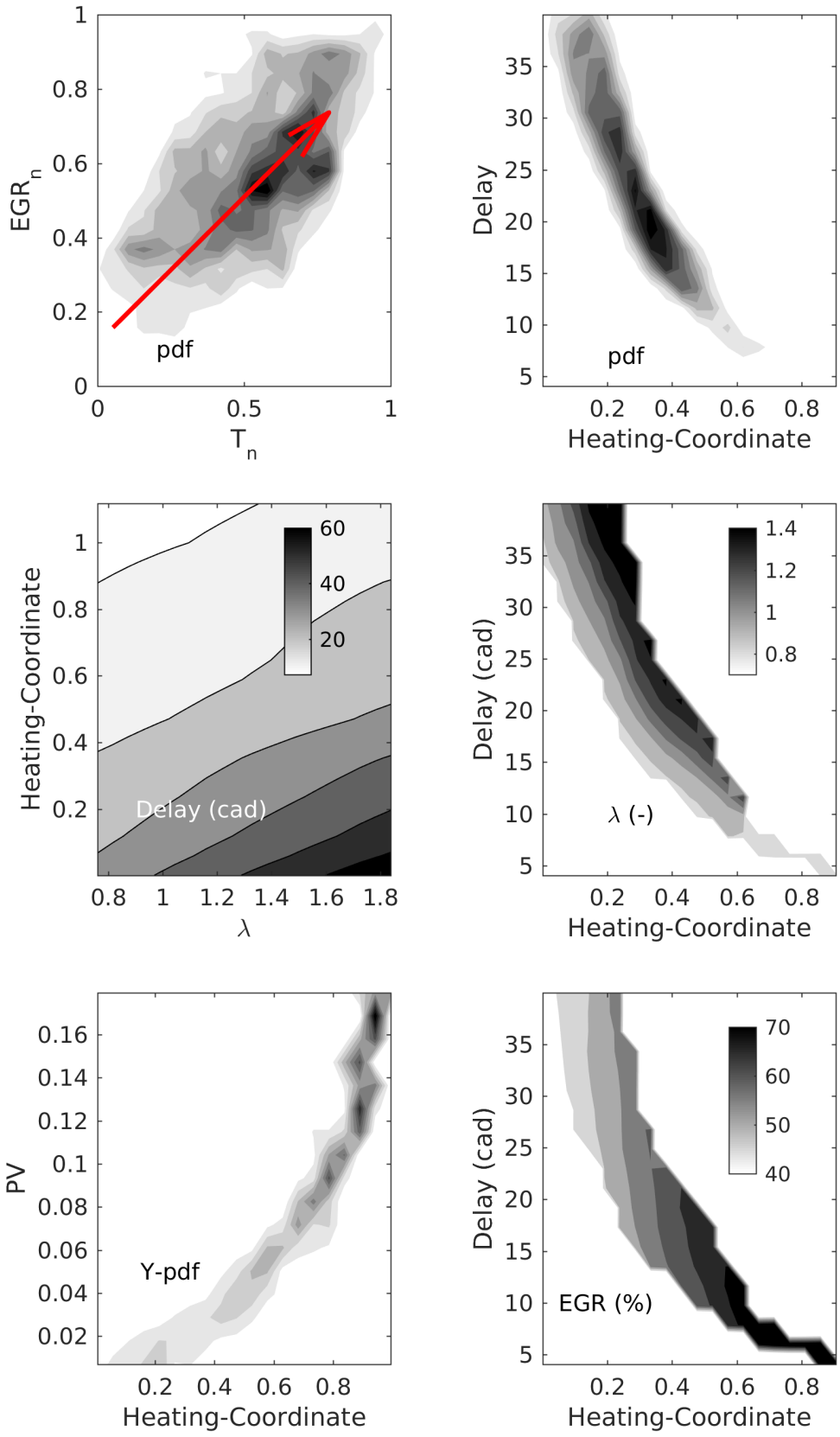

Figure 7.14: Illustration of the thermo-chemical states within the engine at -10 cad by means of the *Heating-Coordinate* as introduced in the top left by means of the normalized (index n) T-EGR-space.

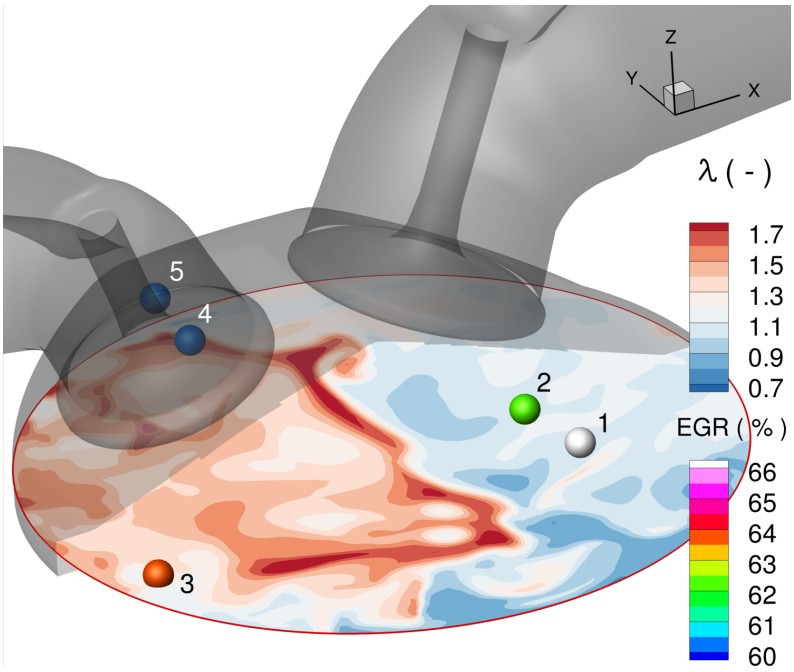

Figure 7.15: Positions of the points considered. Points are coloured with their *EGR* at -10 cad. The slice shows λ at -20 cad.

4. The fourth point has no wall influence but very poor mixing conditions. Its *EGR* is still average but λ is high. Accordingly, it has a low temperature and ignites rather late.

5. Finally this point has poor mixing conditions and is also submitted to heat losses. These conditions represent the last to complete the reaction. However, since the volume-to-surface ration is low at the TDC, those conditions have a significant contribution to the overall process.

To provide a better view on the spatial distribution Fig. 7.17 shows the temporal evolution found along a line connecting two of these points. First, Fig. 7.17a is monitored along the line connecting the points one and two. As one can see, in between point one (at r=0 mm) and point two the reaction evolves slower. The main cause is that they are separated by a region with a significantly lower *EGR* and corresponding initial temperature as illustrated in the left plot. Furthermore, as the plot on the right indicates, also λ is higher and accordingly it requires further compression to sufficiently lower the ignition delay.

Still for all positions along this line, λ was still within the range for a good ignition. This is contrasted in Fig. 7.17b showing the same information for a line connecting the points one and four. As one can see in Fig. 7.15 on about half the way one enters regions of high λ representing poor ignition conditions with the correspondingly increased delay.

As the last part of this section it is useful to supplement the observations at certain positions by statistics gathered within the whole in-cylinder volume. Therefore a conditioned analysis was performed as exemplified in Fig. 7.18. It shows the pdf of the

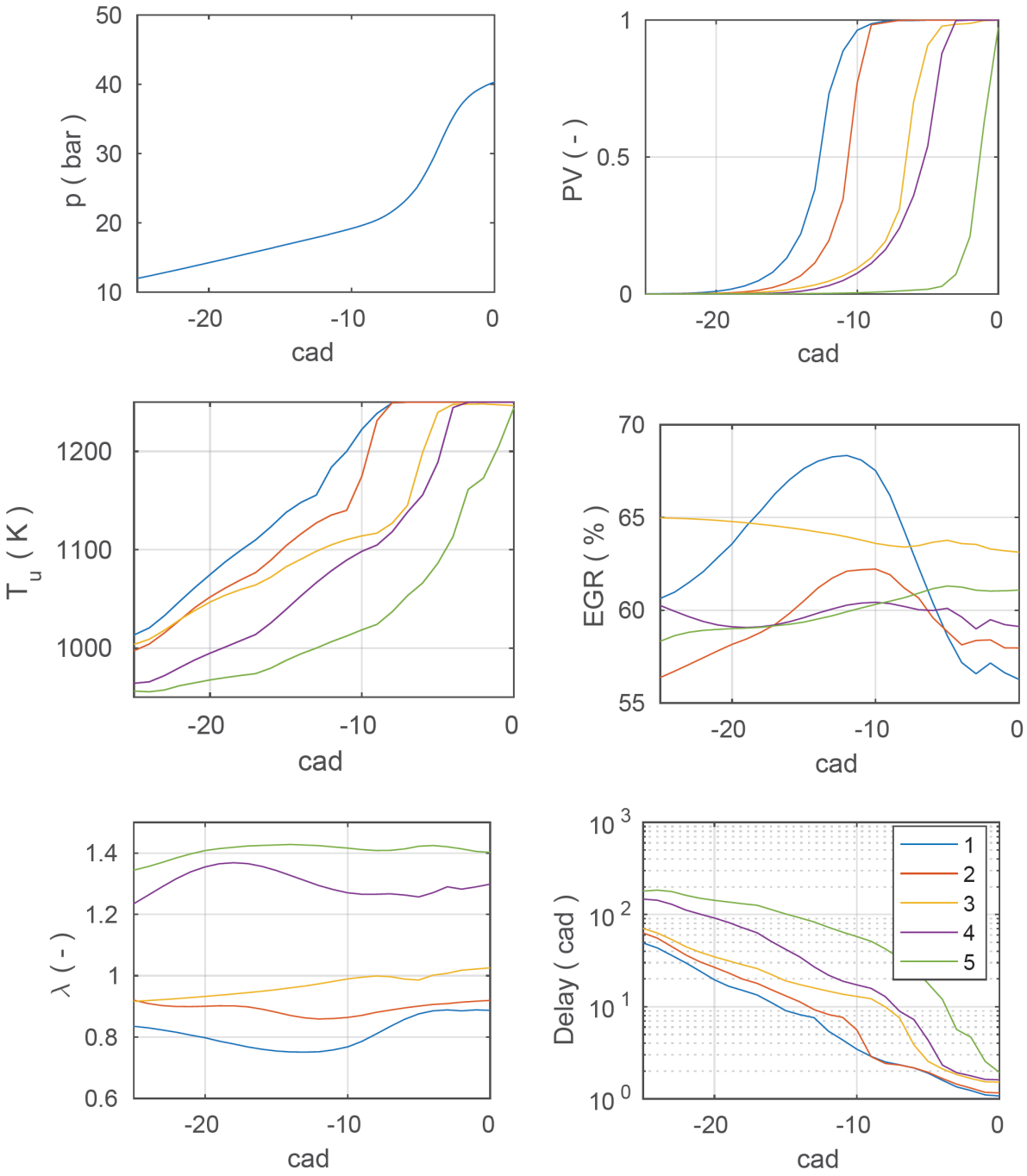

Figure 7.16: Evolution of thermo-chemical quantities over cad for the five positions marked in Fig. 7.15. The pressure of the corresponding cycle has been added in the top left for orientation.

EGR conditioned on the progress variable, i.e. it shows which *EGR* values are found for a given progress variable. The first instant shown is -12 cad where the first spots approach the fully reacted state. The evolution shows what is already known from the previous section: only at high *EGR* values reaction progress is found. At -10 cad reaction is already found also for lower *EGR* values. Furthermore, the distribution became broader since the ignition criteria are now no longer limited to the best spots exclusively. Within

the third plot showing -5 cad a completed reaction progress is found for all kinds of *EGR* values and broadening continued. Finally at -2 cad the reaction mostly completed where now also the lowest *EGR* states (50%) react.

This representation of the reaction progress by means of the conditioned pdf is summarized in Fig. 7.19. For a more compact presentation it only shows the mean values

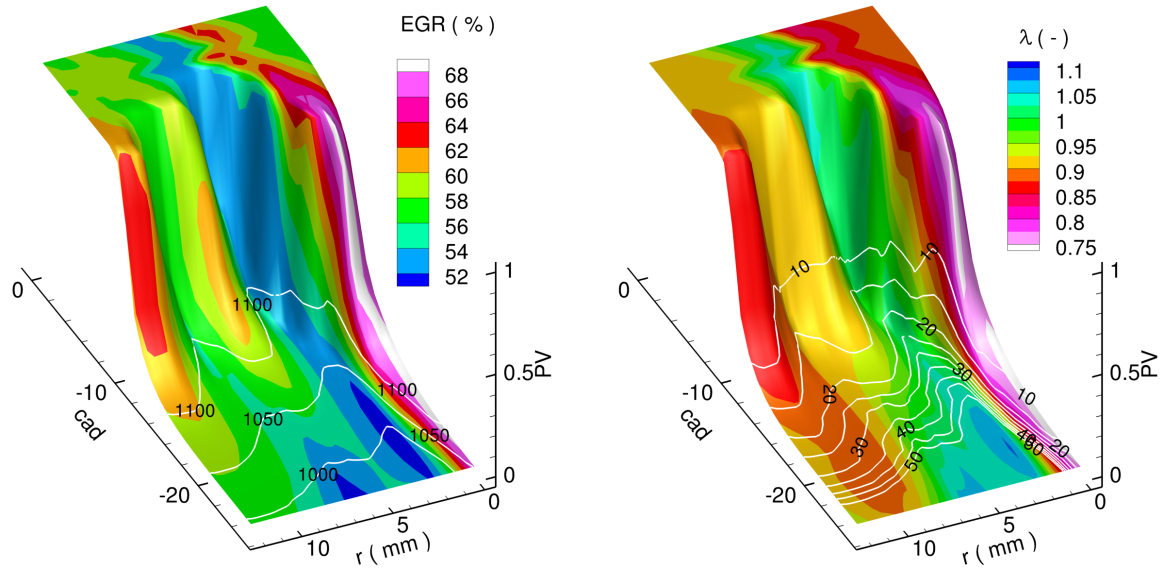

(a) Line from point one to two.

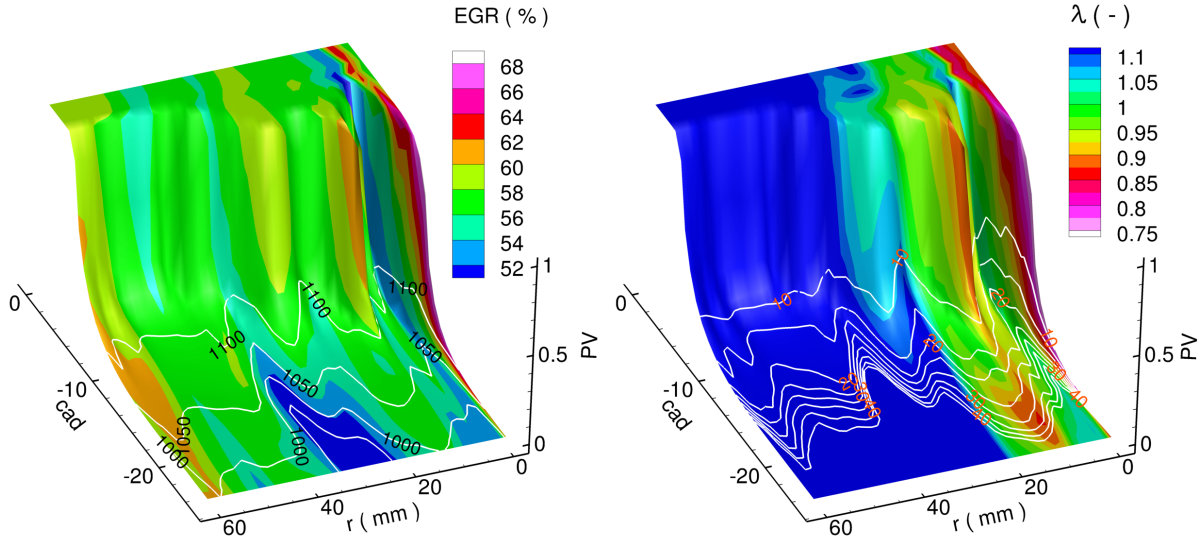

(b) Line from point one to four.

Figure 7.17: Evolution of the reaction progress variable over cad. States are extracted along a line connecting two of the points marked in Fig. 7.15. The unburnt gas temperature (K) and ignition delay times (cad) have been added with lines to the left and right plot, respectively. r denotes the distance starting at the first point.

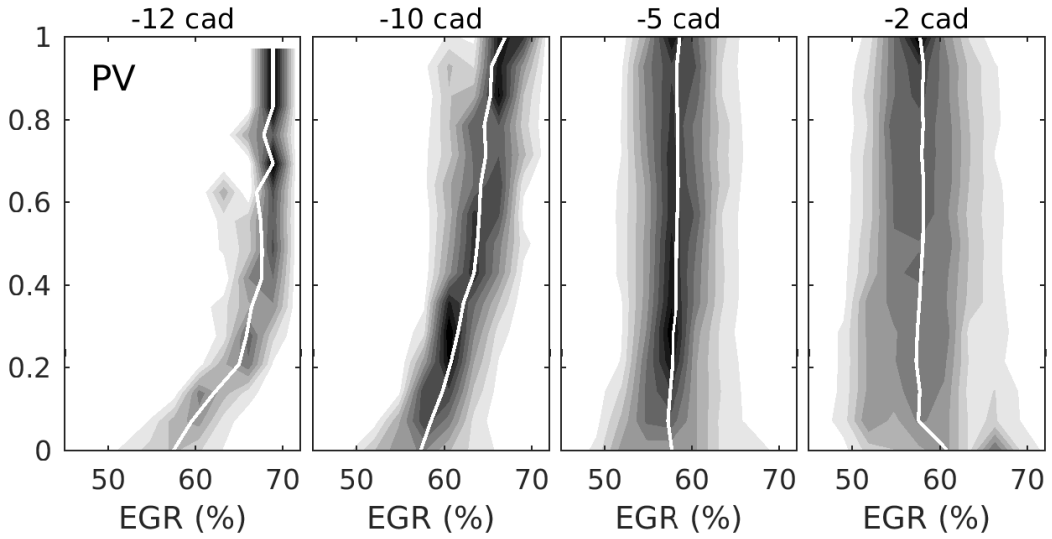

Figure 7.18: pdf of *EGR* conditioned on the progress variable for four different cad. White line denotes the average.

as indicated by the white line in Fig. 7.18. For λ an identical evolution as outlined for the *EGR* is found where the lowest values react first and the behavior converges towards a vertical line with increasing cad. The temperature behaves different due to its physical significance. In contrast to the *EGR* and λ it increases by the compression and determines the ignition for a given mixing state. Even though the curves show a certain statistical inaccuracy an interesting and somehow expected observation can be made. Looking for example at which unburnt gas temperature T_{u} certain conditions reach half of the reaction progress (PV=0.5) the following evolution is visible: Up to approx. -4 cad, the temperature required to reach this state increases. This is likely linked to the dependencies shown in Fig. 7.12, i.e. with increasing cad the ignition takes place at less suited mixing conditions which require a higher temperature to ignite. Within the two latest cad it becomes visible that the reaction gets strongly influenced by the wall being that intermediate states of the reaction progress variable are found for rather low temperatures.

Before closing this section to visualize the whole ignition process, the temporal development of PV and T are illustrated within a z-slice in Figures 7.20 and 7.22, respectively. The illustrated cycle is identical with the cycle shown in Figure 7.15. Accordingly, the same illustrations are given within a y-slice in Figures 7.21 and 7.23, respectively.

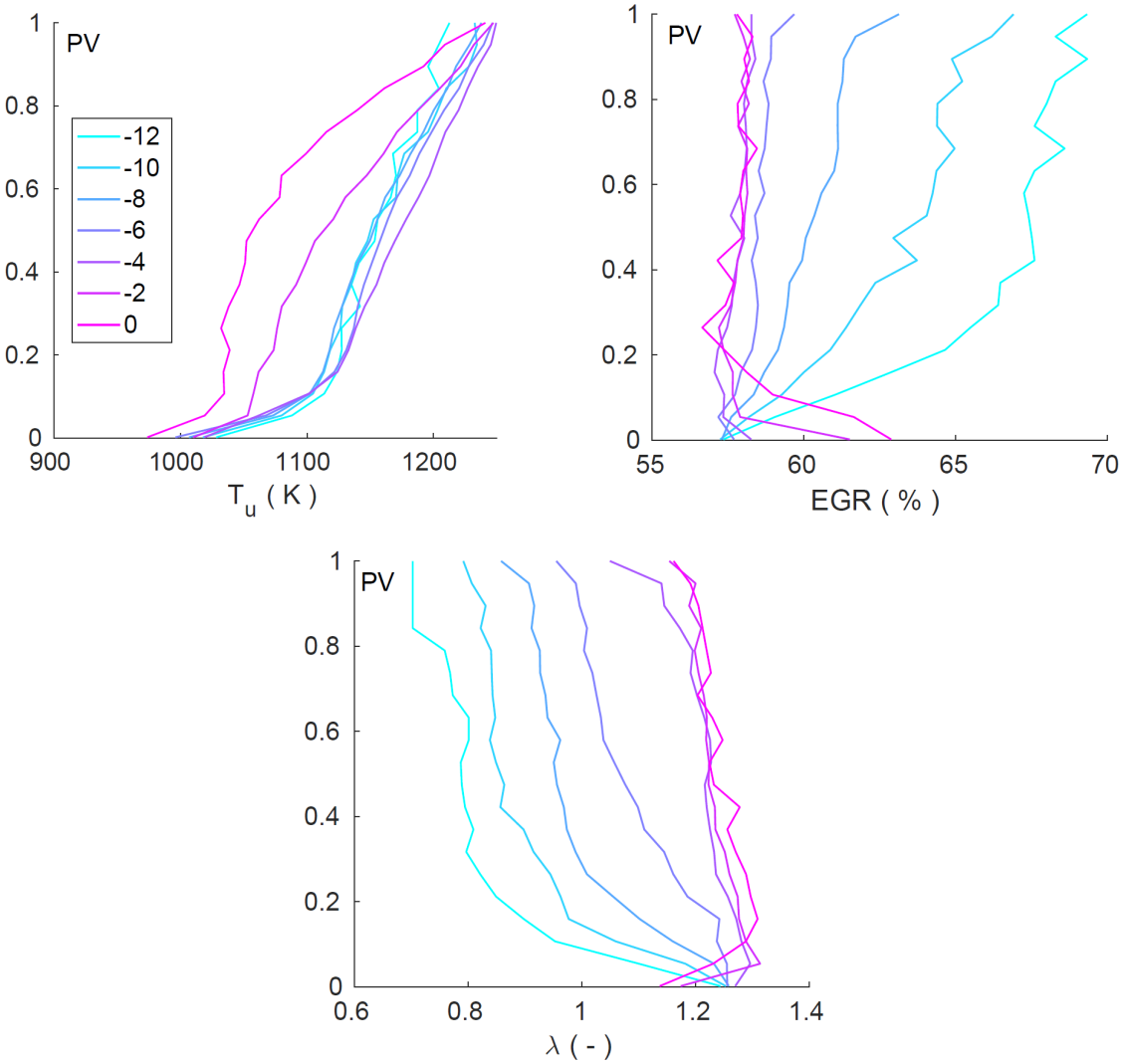

Figure 7.19: Average values of T_u, EGR and λ conditioned on the progress variable. Evolution throughout the combustion process indicated by the range of cad (legend).

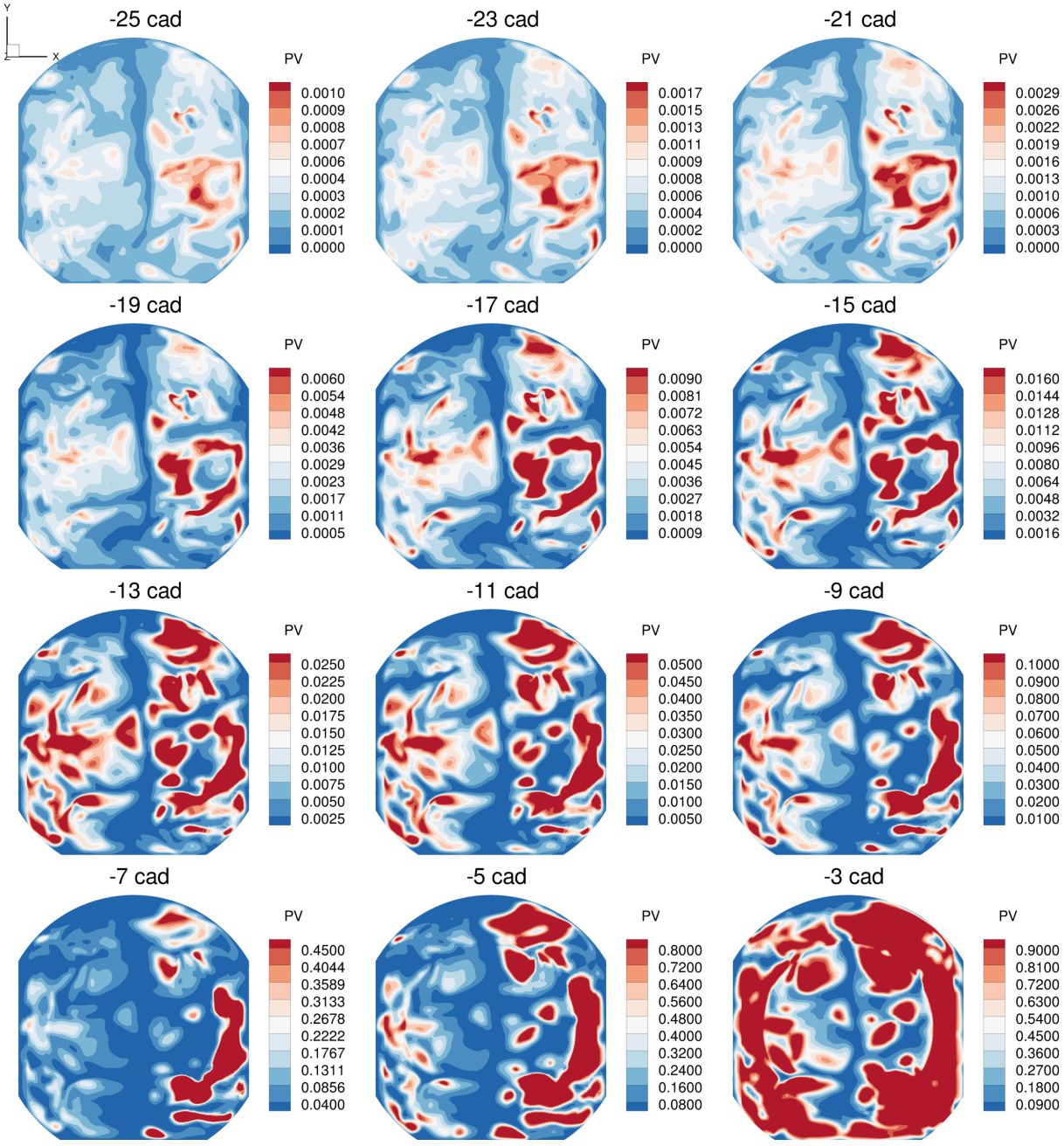

Figure 7.20: Temporal development of PV for the cycle which is illustrated in Figure 7.15 (z-direction)

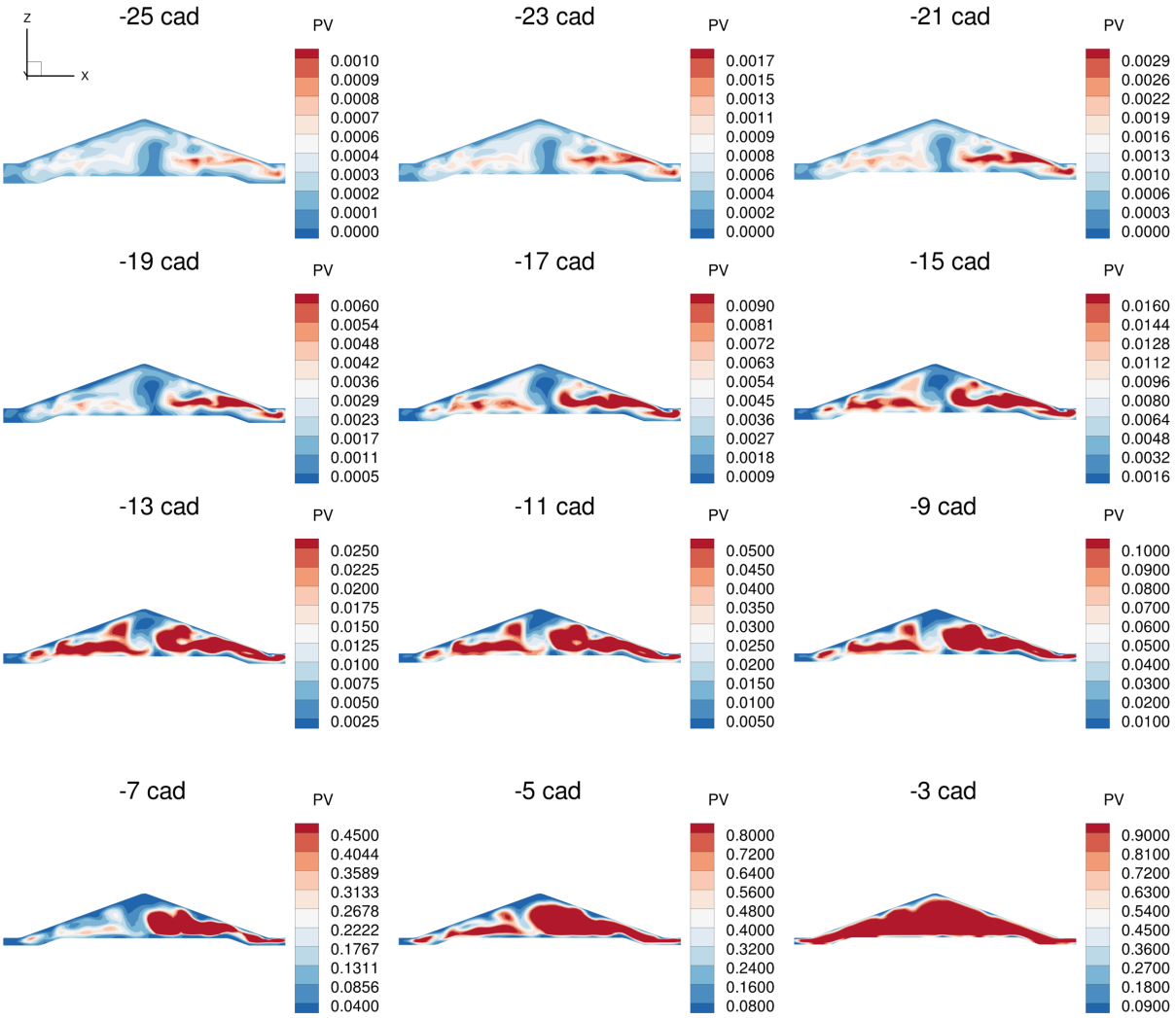

Figure 7.21: Temporal development of PV for the cycle which is illustrated in Figure 7.15 (y-direction)

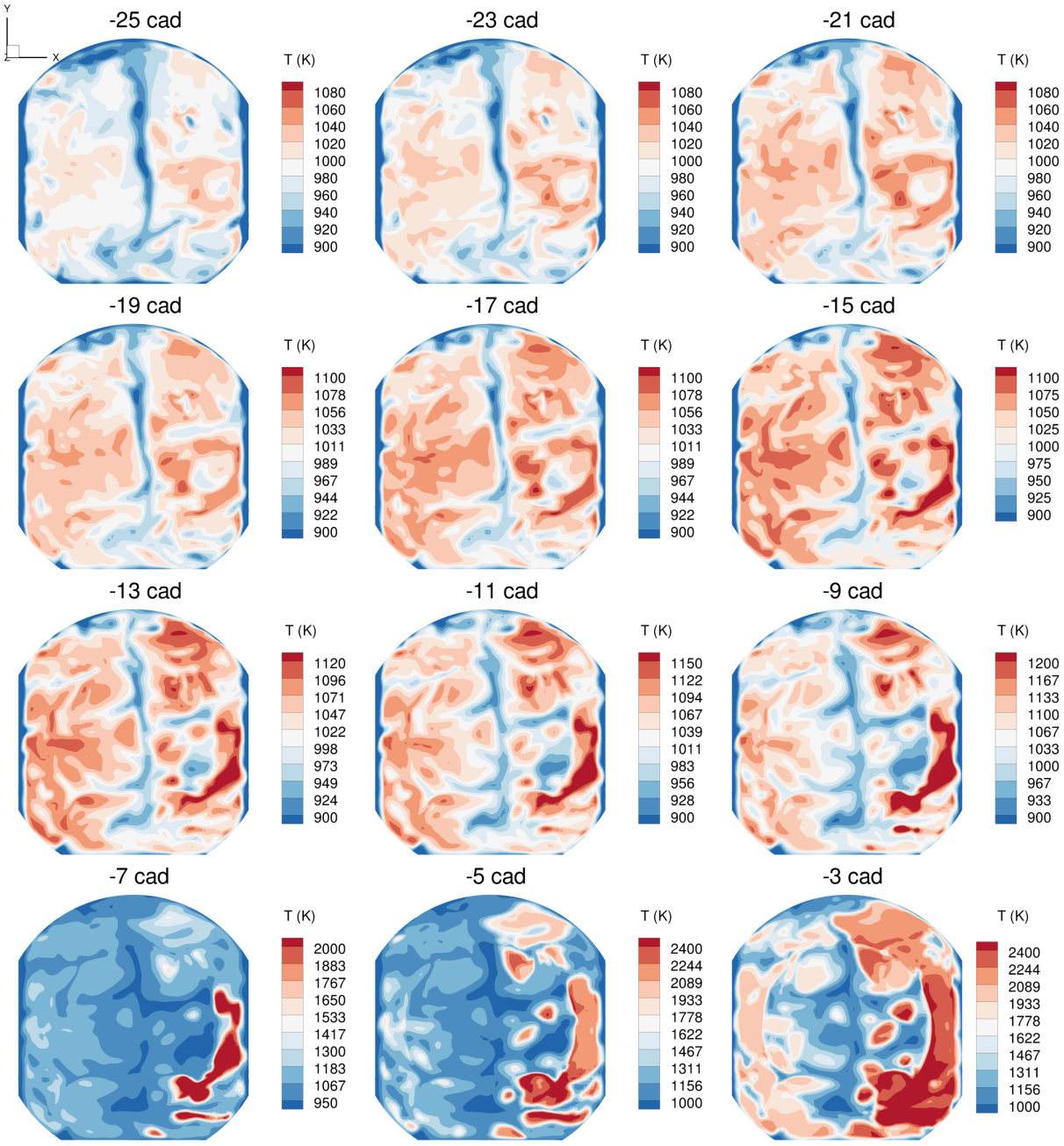

Figure 7.22: Temporal development of T for the cycle which is illustrated in Figure 7.15 (z-direction)

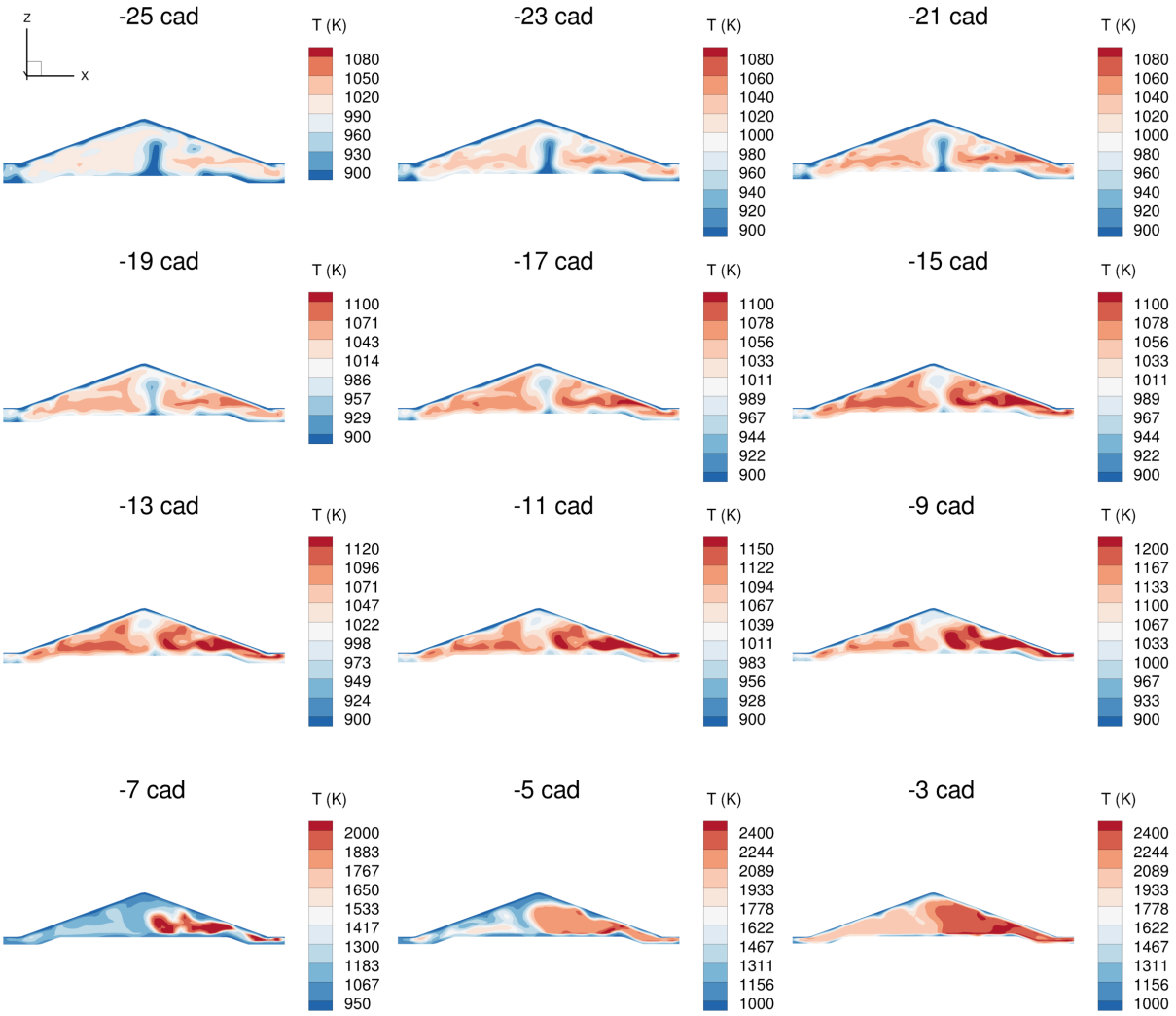

Figure 7.23: Temporal development of T for the cycle which is illustrated in Figure 7.15 (y-direction)

7.3.3 Global behavior and consecutive cycles

Up to now only a single cycle is considered. The analysis provided us a good understanding of the process, specifically the distribution of scalar quantities, how they interact and accordingly determine the combustion process. To complete the analysis of this engine within this last results section, the global behaviour and compare different cycles are considered.

Plot 1 in Fig. 7.24 shows the ignition time for eleven consecutive cycles. For the illustration in this section the cycles 11 to 20 of the first set of simulations are chosen. The first ten cycles have been excluded to remove effects from the initialization which persist for a long time due to the EGR. This ignition time is defined to be the cad where the slope of the spatially averaged reaction progress variable has its maximum. This criterion was found to be appropriate to judge on the ignition strength of a cycle and is consistent with other quantities like the instant of pressure increase when comparing the cycles amongst each other. One can observe a total variation of about 7 cad and a maximum difference of about 4 cad between two consecutive cycles. This is quite significant and worth a deeper look. From the previous analysis one knows that a high *EGR* can produce good ignition conditions but as the first plot in Fig. 7.25 demonstrates there is no clear correlation - at least not to the average *EGR* of the respective cycle. Still it could be that the *EGR* is more homogeneous for the cycles that show a late ignition. But this is not the case as given in Fig. 7.28. It shows the joint pdf as already introduced in Fig. 7.10 but for cycles of different ignition strength. As the corresponding pressure curves on the right illustrate a rather weak, average and strong cycle are chosen respectively. One can see, that for a given cad before ignition, indeed the *EGR* distribution spans a similar range indicating equal inhomogeneities. However, the slope is very different such that the strong cycle reaches high temperatures that do not even exist in the weak one and have a lower probability for the average cycle. Accordingly, the inhomogeneities are analyzed in the last section are important for the combustion process for a given cycle. But when comparing individual cycles there seem to be further determining factors. The cycles apparently have a different average temperature superimposed onto a similar inhomogeneous mixture. Indeed, a clear correlation exists between this average temperature before ignition (T_{Ign} defined to be at -25 cad where no combustion yet occurred) and the ignition time as given by their correlation in plot 2 of Fig. 7.25.

Accordingly, the question is what this increased average temperature caused. To understand this, first it is aimed to see from where it evolved, simply from an observing point of view and then follow it up by an explanation. Since the engine has no significant thermal variations and fuel gets injected at identical temperatures for each cycle, it is clear that the difference is in the history of the gases. Therefore one can backtrack it through its state at the inlet-valve-close and open (IVC and IVO), the preceding's cycles exhaust valve close and open (EVC and EVO) and its state found after the combustion of the preceding cycle (aComb) defined to be at 80 cad. Starting from the third plot in Fig. 7.25, as expected T_{Ign} translates from T_{IVC} which in turn correlates with T_{IVO} (plot 4). This latter is not necessarily expected but will be explained later. Going further

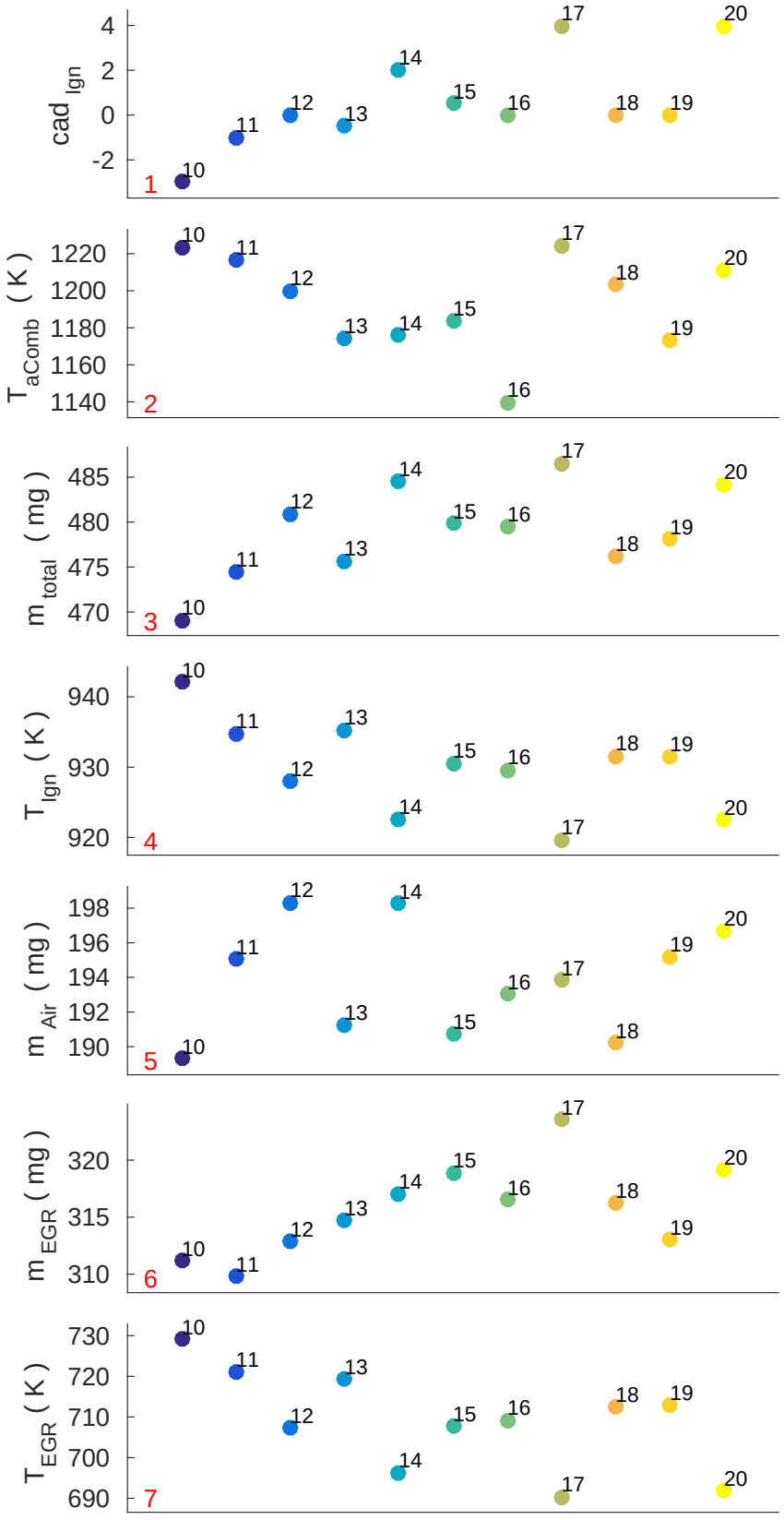

Figure 7.24: Evolution of (spatially averaged) quantities over eleven consecutive cycles. Cycle numbers are indicated at the symbol. Like the symbol color those correspond to the one shown in Fig. 7.25. The red numbers denote the respective plot as referred to in the text. See Table 7.3 for the decleration of the quantities.

Table 7.3: Decleration of the global quantities shown in Figure 7.24

Quantity	Declaration
cad_{ign} (cad)	Ignition start
T_{aComb} (K)	Temperature after combustion at 80 cad.
m_{total} (mg)	Total mass after inlet valves are closed.
T_{Ign} (K)	Temperature before ignition at 25 cad.
m_{Air} (mg)	Mass of total fresh air issued in-cylinder.
m_{EGR} (mg)	Trapped exhaust gas mass from the previous cycle.
T_{EGR} (K)	Temperature of trapped exhaust gas before inlet valves are opened, at -266 cad.

back to plot 5, the temperature T_{IVO} correlates with the one found after the exhaust valve close of the preceding cycle. As plot 6 indicates also the gases after and before the exhaust phase correlate but with certain deviations. The latter in turn is perfectly correlated to the state after combustion (plot 7 in Figure 7.26). Accordingly, one can bridge these subsequent steps in plot 8 of Figure 7.26 showing the temperature before ignition as a function of the one found after combustion of the preceding cycle. This

Table 7.4: Decleration of the global quantities shown in Figure 7.25

Quantity	Declaration
cad_{ign} (cad)	Ignition start
$EGR(\%)$	EGR in mass fraction.
T_{Ign} (K)	Temperature before ignition at -25 cad.
T_{IVC} (K)	Temperature right after the inlet valves are closed, at -150 cad
T_{IVO} (K)	Temperature right before the inlet valves are opened, at -266 cad.
T_{EVC} (K)	Temperature right after the exhaust valves are closed, at 273 cad.
T_{EVC-1} (K)	T_{EVC} of the previous cycle.
T_{EVO} (K)	Temperature right before the exhaust valves are opened, at 170 cad.

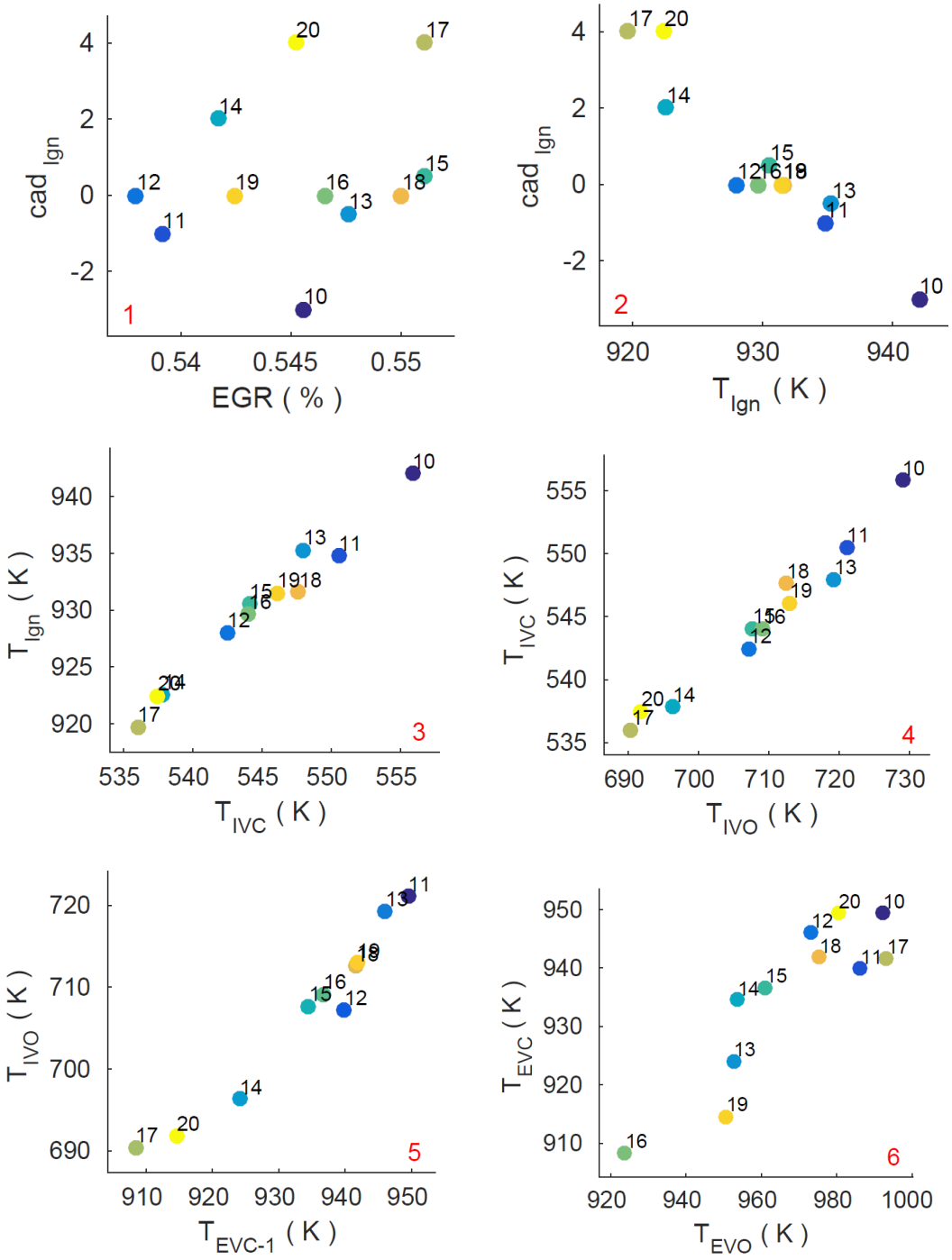

Figure 7.25: Correlations of important quantities. The '-1' in the subscript denotes quantities from the preceding cycle. Symbol numbers and colors correspond to Fig. 7.24. The red numbers denote the respective plot as referred to in the text (Part I). See Table 7.4 for the decleration of the quantities.

correlation has a certain scatter arising from the sum of the intermediate processes but still shows a visible trend. Via the correlation in plot 2 of Figure 7.25 one can now directly link these conditions after combustion to the cad of ignition in plot 9 of Figure 7.26.

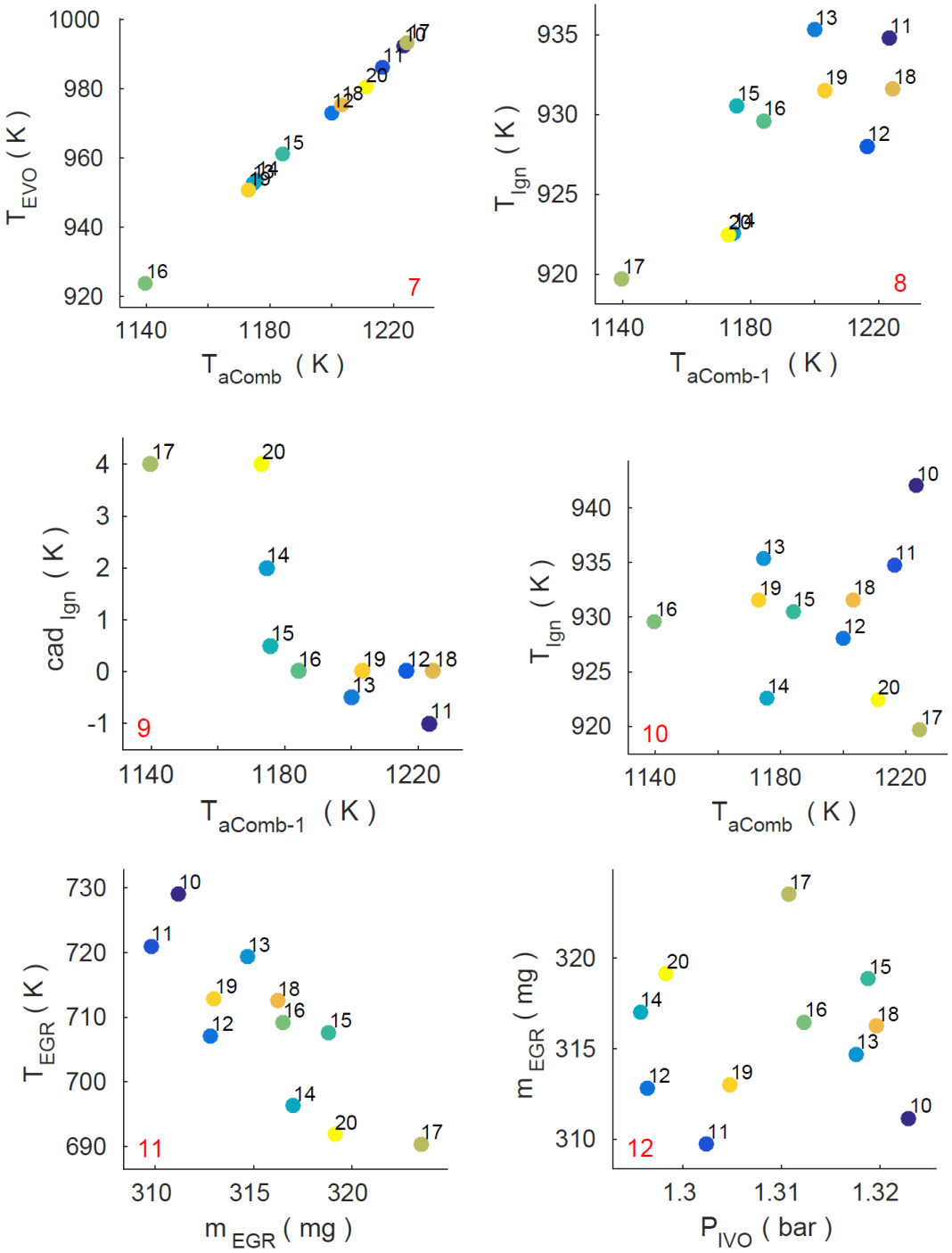

Figure 7.26: Correlations of important quantities. The '-1' in the subscript denotes quantities from the preceding cycle. Symbol numbers and colors correspond to Fig. 7.24. The red numbers denote the respective plot as referred to in the text. (Part II). See Table 7.5 for the decleration of the quantities.

Table 7.5: Decleration of the global quantities shown in Figure 7.26 and 7.27

Quantity	Declaration
T_{EVO} (K)	Temperature right before the exhaust valves are opened, at 170 cad.
T_{aComb} (K)	Temperature after combustion at 80 cad.
T_{Ign} (K)	Temperature before ignition at -25 cad.
$T_{aComb-1}$ (K)	T_{aComb} of the previous cycle.
cad_{ign} (cad)	Ignition start
m_{EGR} (mg)	Trapped exhaust gas mass from the previous cycle.
T_{EGR} (K)	Temperature of trapped exhaust gas before inlet valves are opened, at -266 cad.
p_{IVO} (bar)	Pressure before inlet valves are opened, at -266 cad.

So it is observed, that a cycle leaving exhaust gases with a high temperature very likely lowers the ignition delay of its successor. The scatter indicates that there are other parameters but a trend definitely exists. Shedding further light onto this requires to consider many parameters. For example, from the equation of state one guess could be, that a high temperature is caused by a large trapped mass, but those are not correlated (not shown). Also the peak pressure is not a good indicator since it does not strongly depend on the overall energetic state but rather on the cad where it occurs. Also, a bit surprising, as plot 10 in Fig. 7.26 indicates, the temperature after combustion is not correlated with the one before combustion. This could be suggested when assuming a given energy release that causes an offset to its initial state. The root causes are not straight

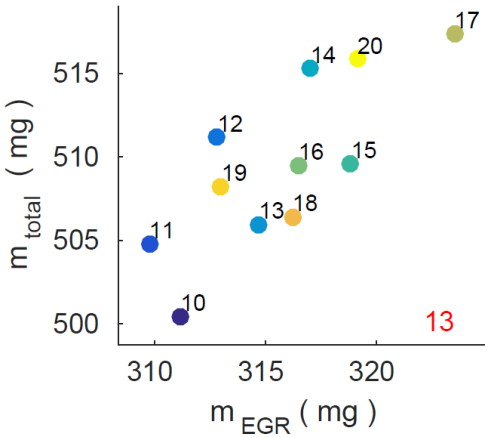

Figure 7.27: Correlations of important quantities. The '-1' in the subscript denotes quantities from the preceding cycle. Symbol numbers and colors correspond to Fig. 7.24. The red numbers denote the respective plot as referred to in the text. (Part III)

forward and some correlations appear counterintuitive at a first glance. We found it best to outline the mechanisms along some consecutive cycles to provide a good understanding.

We consider the cycles starting with cycle number 15. As given in Fig. 7.24, cycle 17 has a very late ignition and from our above analysis cycle 16 then should have a low T_{aComb} which holds true (plot 2 in Fig. 7.24), but cycle 15 is chosen to start. As one can see in Fig. 7.24, cycle 15 and 16 have the same mass, the same temperature before

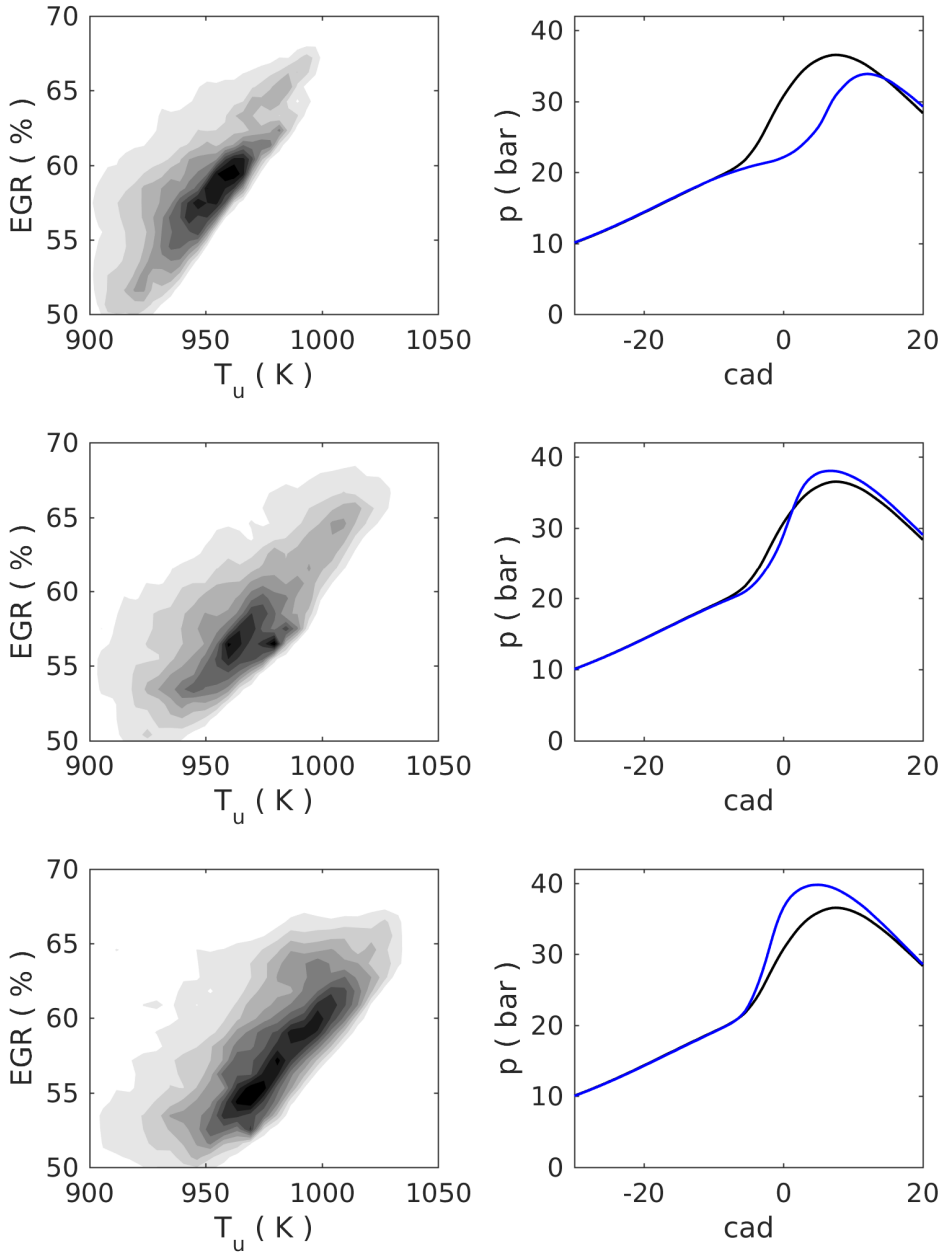

Figure 7.28: Joint pdf of T_{u} and *EGR* for a weak (top), average (middle) and strong (bottom) cycle at -25 cad. On the right the corresponding pressure curve is given in blue in comparison to the averaged one in black.

ignition and corresponding ignition time (plot 3, 4 and 1, respectively). However, the temperature after combustion of cycle 16 is lower by 44 K being a visible drop in this regard. The difference to cycle 15 is that in cycle 16, the same mass constitutes of a lower *EGR* mass and a larger amount of air issued through the inlet valve. The causes for this latter will become clear when one considers the processes following the combustion of cycle 16 and first take the low T_{aComb} of it as granted.

Given the low T_{aComb} of cycle 16, the pressure is correspondingly low and as a result a lower amount of mass will leave the cylinder when the exhaust valves open. Hence, as one can see in plot 6 of Fig. 7.24, cycle 17 has a high *EGR* mass. It is important to keep in mind that this exhaust gas is comparatively cold as given by its previous cycle. It is visible in plot 7 of Fig. 7.24 that cycle 17 has a rather low *EGR* temperature and indeed, as plot 11 in Fig. 7.26 indicates, the *EGR* mass and its temperature are generally negatively correlated. This is a first property to notice. From our local analysis it is known that a locally high *EGR* favors ignition. However, when considering a globally high *EGR* it is partially countered by having a low temperature. When one approaches the IVO with this *EGR* mass, two countering effects come into play. The in-cylinder mass is rather high but it is also cold such that the pressure at this instant does not correlate with the in-cylinder mass as indicated in plot 12 of Fig. 7.26. Indeed, as visible in this plot those pressures are almost identical for cycle 16 and 17 yielding the same mass of air issuing during the intake phase (see plot 5 in Fig. 7.24). This means, that cycle 17 has a high *EGR* mass and the same mass of air, i.e. a larger total mass. Indeed, plot 13 of Fig. 7.27 confirms that those are often correlated. This now also explains why the temperatures before and after the inlet valve phase are correlated (plot 4 in Fig. 7.25): Given that the same amount of air enters in the cycles 16 and 17 with the same air-temperature, the state is obviously determined be the exhaust gas temperatures.

Looking at the properties of cycle 17 in Fig. 7.24 one can see that this history results in one of the latest reactions leaving a high temperature after combustion. At this, the strong ignition delay is caused by the low exhaust gas temperature of its preceding cycle giving little potential for hot spots has discussed in the previous section. However, it also has a high temperature after combustion due to its large total mass yielding high pressure and temperature conditions for a given cylinder volume. Still, is necessary to remind, that it is not the total mass alone but also its composition as outlined for this cycle. According to this high T_{aComb}, cycle 18 has a low ignition delay again. The procedure outlined here for cycle 15 to 17 repeats at cycle 18 to 20. It would require a significant amount of more cycles computed to gather statistics of this processes spanning over several cycles. However, our explanation represents logical basis to understand such large cycle-to-cycle variations. Also for some of the smaller variations in between consecutive cycles observed this explanation holds true but the physical significance is less dominant such that other parameters like local inhomogeneities can interfere.

Chapter 8

Summary and conclusions

Building upon the previous studies, within this work a numerical method to simulate CAI engines is developed. The model consist of the joint application of LES and pre-tabulated auto-ignition chemistry which is implemented into the engine code KIVA-4mpi. The pre-tabulation of the chemistry was performed by Dr. Ing.-Marc-Sebastian Benzinger from Institute of Technical Thermodynamics, Karlsruhe Institute of Technology. To capture the complex chemistry of auto-ignition, a detailed reaction mechanism [12] is used. As the progress variable specific entropy is chosen, which shows a good sensitivity to chemical activity of early phases of the ignition process and increases monotonically. A multi-dimensional chemistry table is generated to cover inhomogeneous engine conditions.

The simulated CAI engine has high inhomogeneities in mixture and temperature field. Therefore, the auto-ignition model which is based on homogeneous reactor simulations, has been tested for systems with dissipative transport. For that purpose, from the CAI simulations obtained mixture and temperature profile is used to simulate a Continuously Stirred Tank Reactor (CSTR). The simulations with different mixing rates are performed by using the detailed chemistry and the reduced model (The results are delivered by Dr.-Ing. Robert Schießl from the Institute of Technical Thermodynamics (ITT)). At fast mixing rates where chemistry and transport processes are coupled strongly, i.e., combustion is not dominated with chemistry anymore, reduced model starts to become insufficient and deviates more from detailed model. However for our CAI engine for which the mixing rate is less than $10s^{-1}$ the reduced model is capable to describe auto-ignition[128].

Within KIVA-4mpi, the overall numerical framework is verified with zero and one dimensional test cases and applied to a real engine configuration. The zero dimensional test cases have shown that the selected tabulation grid, in conjunction with the simple linear interpolation scheme for retrieving source terms $\dot{\omega}_{\mathrm{heat}}$ and $\dot{\omega}_{\mathrm{heat}}$, yields a shift in temporal evolution of temperature and progress variable PV. This problem of linear interpolation could be minimized by generating finer grid points in tabulation. However, a finer the look-up table in each of the 5-dimensions would have immense RAM costs. Instead of a finer look-up table, more accurate interpolation schemes can be employed, but they are be more complex and also computationally more intensive. For the first application in CAI of our 5-dimensional look-up table, the simple linear scheme was found to be sufficient for our purpose and therefore it is employed in this work. The 1d test case, where an engine-like configuration is simulated, verified the solution procedure of unburnt

temperature. The results from 1d simulation has also shown that the interpolation errors have an acceptable affect on ignition delay for systems in which enthalpy and pressure varies strongly.

This work applied LES to a CAI engine using a five-dimensional pre-tabulation strategy to predict the auto-ignition process. The individual physical mechanisms evolving throughout the cycle have been outlined to provide a basic understanding of the overall process. The dependency of the ignition on scalar quantities being the temperature, air-ratio, *EGR*, and pressure is outlined. The effect has been quantified by means of one-dimensional piston simulations for typical combinations of those as found in the actual engine.

A statistical analysis was performed to characterize the strong spatial inhomogeneities within the cylinder. It revealed a strong correlation between the *EGR* and the temperature as well as two separate branches along which the probability of *EGR* and the air-ratio evolved. These evolutions have been explained by outlining and visualizing the respective processes. It is showed that a preheating by *EGR* takes place along a trajectory in the thermo-chemical space which we termed the *Heating-Coordinate*. By projecting this heating coordinate onto the thermo-chemical space of the ignition table it is showed that its slope is the main vector in producing conditions able to ignite. Accordingly the reaction process was strongly correlated with this composition coordinate. A certain scatter orthogonal to this coordinate exists which is mostly caused by variations in the air ratio. It was demonstrated that the combustion process is pre-determined by these conditions which we supplemented by tracking individual points and lines through the reaction phase.

The analysis of consecutive cycles revealed a strong influence caused by the EGR. It was shown that the cycles show non-negligible differences in the ignition delay. An explanation was provided for a variation that spans over 3-4 cycles supported by correlations of the decisive quantities. This study was somehow limited by the sample number but still enabled to shed light onto the mechanisms evolving. Therefore for a better statistical analysis of the results, CAI simulations should run further at least until 50 cycles are completed.

Finally, although for the computations of the CAI engine only 16 CPUs and a relatively coarse mesh (almost 2.3 Mio. cells) mesh are used, the requirement of RAM is extremely high (64 GB) . This is the result of the parallelization strategies of the KIVA-4mpi code, which highly limits the spatial resolution of the computational domain and the dimension and resolution of the chemistry table. As a result, the quality of the LES of CAI engines are affected. Therefore, for further work it is suggested to improve parallelization strategies of the KIVA-4mpi code. This would help to use computational resources more reasonable and also deliver more reliable LES results.

Bibliography

[1] *REGULATION (EC) No 715/2007 OF THE EUROPEAN PARLIAMENT AND OF THE COUNCIL.* online.

[2] *Kyoto protocol to the united nations framework convention on climate change.* November 15, 2008.

[3] *Kyoto protocol to the united nations framework convention on climate change.* November 15, 2011.

[4] A., Leonard: *Energy cascade in large eddy simulation of turbulent fluid flow.* Adv. Geophys., 18A:237–248, 2004.

[5] A., Paykani, Kakaee A. H., Rahnama P. and Reitz R. D.: *Progress and recent trends in reactivity-controlled compression ignition engines.* International Journal of Engine Research, 17:481–524, 2016.

[6] A., Zagaris, Kaper H. G. and Kaper T. J.: *Fast And Slow Dynamics For The Computational Singular Pertubation Method.* Multiscale Model. Sim., 2:613–638, 2004.

[7] Aceves S. M., Flowers D. L., Martinez-Frias J. and Dibble R. et al.: *HCCI Combustion: Analysis and Experiments.* SAE Technical Paper 2001-01-2077, 2001.

[8] Amsden, A. A.: *KIVA-3: A KIVA program with block-structured mesh for complex geometries.* Technical Report LA-12503-MS, Los Alamos National Laboratory, 1993.

[9] Amsden, A. A.: *KIVA-3V: A block-structured KIVA program for engines with vertical or canted valves.* Technical Report LA-13313-MS, Los Alamos National Laboratory, 1997.

[10] Amsden A. A., O'Rourke P. J. and Butler T. D.: *KIVA-II: A computer program for chemically reactive flows with sprays.* Technical Report, 1989.

[11] Andrae J.C.G. , Björnbom P. , Cracknell R.F. and Kalghatgi G.T.: *Autoignition of toluene reference fuels at high pressures modeled with detailed chemical kinetics.* Combustion and Flame, 149:2–24, 2007.

[12] Andrae J.C.G. and Head R.A.: *HCCI experiments with gasoline surrogate fuels modeled by a semidetailed chemical kinetic model.* Combustion and Flame, 156:842–851, 2009.

[13] Bendu H. and Murugan S.: *Homogeneous Charge Compression Ignition (HCCI) combustion: Mixture preparation and control strategies in diesel engines.* Renewable and Sustainable Energy Reviews, 38:732–746, 2014.

[14] Benzinger, M.S., R. Schiessl and U. Maas: *A Unified Reduced Model for Auto-Ignition and Combustion in Premixed Systems.* Eurasian Chemico-Technological Journal, 16:107–116, 2014.

[15] Benzinger M.-S.: *Phd. Thesis, Entwicklung eines reduzierteModells zur Beschreibung der Zündung und Flammenausbreitung in kompressionsgezündeten Motoren.* 2016.

[16] Benzinger, M.-S., Schiessl R. and Maas U. : *A Unified Reduced Model for Auto-Ignition and Combustion in Premixed Systems.* Eurasian Chemico-Technological Journal, 16.

[17] BP: *Statistical review of world energy 2016.* online.

[18] Butler, T. D., Cloutman, L. D., Dukowicz, J. K. and Ramshaw, J. D.: *CONCHAS: An arbitrary Langrangian-Eulerian computer code for multicomponent chemically reactive fluid flow at all speeds.* Technical Report LA-8129-MS, Los Alamos National Laboratory, 1979.

[19] Bykov, V. and U. Maas: *The extension of the ILDM concept to reaction–diffusion manifolds.* Combustion Theory and Modelling, 11(6):839–862, 2007.

[20] Bykov, V. and U. Maas: *Problem adapted reduced models based on Reaction–Diffusion Manifolds (REDIMs).* Proceedings of the Combustion Institute, 32(1):561 – 568, 2009.

[21] Cloutman, L. D., J. K. Dukowicz, J. D. Ramshaw and A. A Amsden: *A computer code for reactive flows with fuel sprays.*

[22] Contino F., Lucchini T., D Érrico G., Duynslaegher C., Dias V. and Jeanmart H.: *Simulations of advanced combustion modes using detailed chemistry combined with tabulation and mechanism reduction techniques.* SAE Technical Paper 2012-01-0145, 2012.

[23] Daw C. S., Wagner R. M., Edwards K. D. and Green Jr. J. B.: *Understanding the transition between conventional spark-ignited combustion and HCCI in a gasoline engine.* Proceedings of the Combustion Institute, 31:2887–2894, 2007.

[24] Dec, John E. and Robert E. Canaan: *PLIF Imaging of NO Formation in a DI Diesel Engine1.* SAE International, 1998.

[25] Dukowicz J. K.: *A particle-fluid numerical model for liquid sprays.* Journal of Computational Physics, 35:229–253, 1980.

[26] E., Dec J.: *Advanced compression-ignition engines-understanding the in-cylinder processes.* Proceedings of the Combustion Institute, 32:2727–2742, 2009.

[27] Epping, K., S. Aceves, R. Bechtold and J. Dec: *The Potential of HCCI Combustion for High Efficiency and Low Emissions.* SAE Technical Paper, 2002.

[28] Etheridge J., Mosbach S., Kraft M., Wu H. and Collings N.: *A Detailed Chemistry Multi-cycle Simulation of a Gasoline Fueled HCCI Engine Operated with NVO.* SAE Technical Paper 2009-01-0130, 2009.

[29] Etheridge J., Mosbach S., Kraft M. and Wu H. et al.: *A Detailed Chemistry Simulation of the SI-HCCI Transition.* SAE Technical Paper 2010-01-0574, 2010.

[30] F., Grinstein, Margolin L. and Rider W.: *Implicit Large Eddy Simulation:Computing Turbulent Fluid Dynamics.* Cambridge University Press, 2007.

[31] Fathi M., Khoshbakhti Saray R. and David Checkel M.: *The influence of Exhaust Gas Recirculation (EGR) on combustion and emissions of n-heptane/natural gas fueled Homogeneous Charge Compression Ignition (HCCI) engines.* Applied Energy, 88:4719–4724, 2011.

[32] Favre, Alexandre J. A.: *Formulation of the Statistical Equations of Turbulent Flows with Variable Density, Studies in Turbulence.* Springer New York, 1992.

[33] Ferziger, J. H. and Peric, M.: *Computational Methods for Fluid Dynamics.* Springer, Berlin, 3. edition, November 2001.

[34] Forigua Rodriguez C. F. and Mantilla J.: *Modeling HCCI Engine Combustion Coupling Cantera to KIVA 4.* SAE Technical Paper 2015-01-0816, 2015.

[35] Gan S., Ng H. K. and Pang K. M.: *Homogeneous Charge Compression Ignition (HCCI) combustion: Implementation and effects on pollutants in direct injection diesel engines.* Applied Energy, 88:559–567, 2011.

[36] Gicquel, Olivier, Nasser Darabiha and Dominique Thévenin: *Laminar premixed hydrogen/air counterflow flame simulations using flame prolongation of ILDM with differential diffusion.* Proceedings of the Combustion Institute, 28(2):1901–1908, 2000.

[37] Goryntsev, D.: *Large Eddy Simulation of the Flow and Mixing Field in an Internal Combustion Engine.* PhD thesis, TU Darmstadt, 2007.

[38] Goryntsev D., Sadiki A. and Janicka J.: *Analysis of misfire processes in realistic Direct Injection Spark Ignition engine using multi-cycle Large Eddy Simulation.* Proceedings of the Combustion Institute, 34:2969–2976, 2013.

[39] He, Chao, Guido Kuenne, Esra Yildar, Jeroen van Oijen, Francesca di Mare, Amsini Sadiki, Carl-Philipp Ding, Elias Baum, Brian Peterson, Benjamin Bohm and Johannes Janicka: *Evaluation of the flame propagation within a SI engine using flame imaging and LES.* Combustion Theory and Modelling, submitted, 2016.

[40] Heywood, J. B.: *Internal Combustion Engine Fundamentals.* Automotive Technology Series. McGraw-Hill International Editions, 1988.

[41] Hirt, C. W., Amsden, A. A. and Cook, J. L.: *An Arbitrary Lagrangian-Eulerian Computing Mehtod for All Flow Speeds.* Journal of Computational Physics, 14: 227–253, 1974.

[42] Holst, Michael J.: *NOTES ON THE KIVA-II SOFTWARE AND CHEMICALLY REACTIVE FLUID MECHANICS.* Lawrence Livermore National Laboratory, 1992.

[43] Hosseini V. and David Checkel M.: *Using Reformer Gas to Enhance HCCI Combustion of CNG in a CFR Engine.* SAE Technical Paper 2006-01-3247, 2006.

[44] Ihme, Matthias, Chong M. Cha and Heinz Pitsch: *Prediction of local extinction and re-ignition effects in non-premixed turbulent combustion using a flamelet/progress variable approach.* Proceedings of the Combustion Institute, 30(1):793 – 800, 2005.

[45] Ihme, Matthias, Lee Shunn and Jian Zhang: *Regularization of reaction progress variable for application to flamelet-based combustion models.* Journal of Computational Physics, 231(23):7715–7721, 2012.

[46] International Energy Agency: *Key world energy statistics 2016.* online. http://www.iea.org/publications/freepublications/publication/kwes.pdf.

[47] International Energy Agency: *World energy outlook 2016.* online.

[48] J., Gullbrand and K. Chow F.: *Numerical investigation of numerical errors, subfilter-scale models, and subgrid scale models in turbulent channel flow simulations.* Center of Turbulence Research, 2002.

[49] Jafarmadar S., Nemati P. and Khodaie R.: *Multidimensional modeling of the effect of Exhaust Gas Recirculation (EGR) on exergy terms in an HCCI engine fueled with a mixture of natural gas and diesel.* Energy Conversion and Management, 105:498–508, 2015.

[50] Jia, Ming and Maozhao Xie: *A chemical kinetics model of iso-octane oxidation for {HCCI} engines.* Fuel, 85(17–18):2593 – 2604, 2006.

[51] Jia M. and Xie M.: *A chemical kinetics model of iso-octane oxidation for HCCI engines.* Fuel, 85:2593–2604, 2006.

[52] Joos, F.: *Technische Verbrennung.* Springer, 2006.

[53] K., Inagaki, Fuyuto T., Nishikawa K., Nakakita K. and Sakata I.: *Dual-fuel PCI combustion controlled by in-cylinder stratification of ignitability.* SAE technical paper 2006-01-0028, 2006.

[54] Knop V. and Jay S.: *Latest Developments in Gasoline Auto-Ignition Modelling Applied to an Optical CAI Engine.* Oil & Gas Science Technology - Rev. IFP, 61:1:121–137, 2006.

[55] Knop V., Thirouard B. and Cherel J.: *Influence of the Local Mixture Characteristics on the Combustion Process in a CAI Engine.* SAE Technical Paper 2008-01-1671, 2008.

[56] Kong, Song-Charng: *A study of natural gas/DME combustion in HCCI engines using CFD with detailed chemical kinetics.* Fuel, 86:1483–1489, 2007.

[57] Kruger C., Steiner R., Wenzel P., Schiessl R., Hofrath C. and Mass U.: *3D-CFD Simulation of DI-Diesel Combustion Applying a Progress Variable Approach Accounting for Detailed Chemistry.* SAE Technical Paper 2007-01-4137, 2007.

[58] Kruger C., Steiner R., Wenzel P., Schiessl R., Hofrath C. and Mass U.: *3D-CFD Simulation of DI-Diesel Combustion Applying a Progress Variable Approach Accounting for Detailed Chemistry.* SAE Technical Paper 2007-01-4137, 2007.

[59] Lam, S. H. and D. A. Goussis: *The CSP method for simplifying kinetics.* International Journal of Chemical Kinetics, 26(4):461–486, 1994.

[60] Lam, S.H. and D.A. Goussis: *Understanding complex chemical kinetics with computational singular perturbation.* Symposium (International) on Combustion, 22(1):931 – 941, 1989.

[61] Laramee, R.S., D. Weiskopf, J. Schneider and H. Hauser: *Investigating swirl and tumble flow with a comparison of visualization techniques.* IEEE, 51(58):10–15, 2004.

[62] Lewander M., Ekholm K., Johansson B., Tunestal P., Milovanovic N., Keeler N., Harcombe T. and Bergstrand P.: *Investigation of the Combustion Characteristics with Focus on Partially Premixed Combustion in a Heavy Duty Engine.* SAE Technical Paper 2008-01-1658, 2008.

[63] Liu, Haifeng, Peng Zhang, Zheming Li, Jing Luo, Zunqing Zheng and Mingfa Yao: *Effects of temperature inhomogeneities on the HCCI combustion in an optical engine.* Applied Thermal Engineering, 31(14–15):2549 – 2555, 2011.

[64] Liu H., Zheng Z. and Yao M., et al.: *Influence of temperature and mixture stratification on HCCI combustion using chemiluminescence images and CFD analysis.* Applied Thermal Engineering, 33-34:135–143, 2012.

[65] Lovell, Wheeler G.: *Knocking Characteristics of Hydrocarbons.* Ind. Eng. Chem., 40(12):2388–2438, 1948.

[66] Lu X., Dong H., Rahnama P. and Huang Z.: *Fuel design and management for the control of advanced compression-ignition combustion modes.* Progress in Energy and Combustion Science, 37(6):741–783, 2011.

[67] Lumley, John, L.: *Engines An Introduction.* Automotive Technology Series. Cambridge University Press, 1999.

[68] M.-S.Benzinger, T. Breitenberger, M. Schild N. Fuhrmann C. Dahnz: *Numerische Simulation und Validierung der Benzinselbstzündung.*

[69] Maas, U. and V. Bykov: *The extension of the reaction/diffusion manifold concept to systems with detailed transport models.* Proceedings of the Combustion Institute, 33(1):1253 – 1259, 2011.

[70] Maas, U. and S.B. Pope: *Implementation of simplified chemical kinetics based on intrinsic low-dimensional manifolds.* Symposium (International) on Combustion, 24(1):103 – 112, 1992.

[71] Maas U., Schiessl R., Benzinger M.-S., Janicka J., Breitenberger T., Schulz C., Kaiser S., Schild M., Dreizler A., Fuhrman N., Spicher U., Kubach H. and Dahnz C.: *Numerical simulation and validation of fuel auto-ignition.* In: Proceedings Aachen Colloquium Automobile and Engine Technology, 22:1099–1144, October 2013.

[72] Maas U., Pope S. B.: *Simplifying Chemical Kinetics: Intrinsic Low-Dimensional Manifolds in Composition Space.* Combustion and Flame, 88:239–264, 1992.

[73] Manente V., Johansson B., Tunestal P. and Cannella W.: *Influence of Inlet Pressure, EGR, Combustion Phasing, Speed and Pilot Ratio on High Load Gasoline Partially Premixed Combustion.* SAE Technical Paper 2010-01-1471, 2010.

[74] Milovanovic N., Chen R. and Turner J.: *Influence of the Variable Valve Timing Strategy on the Control of a Homogeneous Charge Compression (HCCI) Engine.* SAE Technical Paper 2004-01-1899, 2004.

[75] Milovanovic N., Chen R. and Turner J.: *Influence of variable valve timings on the gas exchange process in a controlled auto-ignition engine.* Proceedings of the Institution of Mechanical Engineers, Part D: Journal of Automobile Engineering, 218:567–583, 2004.

[76] Misdariis A., Vermorel O. and Poinsot T.: *A methodology based on reduced schemes to compute autoignition and propagation in internal combustion engines.* Proceedings of the Combustion Institute, 35:3001–3008, 2015.

[77] Mosbach S., Kraft M., Bhave A. and Mauss F. et al.: *Simulating a Homogeneous Charge Compression Ignition Engine Fuelled with a DEE/EtOH Blend.* SAE Technical Paper 2006-01-1362, 2006.

[78] N., Peters and Rogg B.: *Reduced Kinetic Mechanisms for Applications in Combustion Systems.* Springer, Berlin, 1993.

[79] Najafabadi, Mohammad Izadi, Bart Somers and Abdul Aziz Nuraini: *Validation of a Reduced Chemical Mechanism Coupled to CFD Model in a 2-Stroke HCCI Engine.* In *SAE Technical Paper.* SAE International, 04 2015.

[80] Nguyen, Phuc-Danh, Luc Vervisch, Vallinayagam Subramanian and Pascale Domingo: *Multidimensional flamelet-generated manifolds for partially premixed combustion.* Combustion and Flame, 157(1):43 – 61, 2010.

[81] Niu, Yi-Shuai, Luc Vervisch and Pham Dinh Tao: *An optimization-based approach to detailed chemistry tabulation: Automated progress variable definition.* Combustion and Flame, 160(4):776–785, 2013.

[82] Ogink R. and Golovitchev V.: *Gasoline HCCI Modeling: An Engine Cycle Simulation Code with a Multi-Zone Combustion Model.* SAE Technical Paper 2002-01-1745, 2002.

[83] Oijen, J A van, F A Lammers and L P H de Goey: *Modeling of complex premixed burner systems by using flamelet-generated manifolds.* Combustion and Flame, 127(3):2124–2134, 2001.

[84] Oijen, JA van and LPH De Goey: *Modelling of premixed laminar flames using flamelet-generated manifolds.* Combustion Science and Technology, 161(1):113–137, 2000.

[85] Oijen, J.A. van, A. Donini, R.J.M. Bastiaans, J.H.M. ten Thije Boonkkamp and L.P.H. de Goey: *State-of-the-art in premixed combustion modeling using flamelet generated manifolds.* Progress in Energy and Combustion Science, 57:30 – 74, 2016.

[86] P., Sagaut: *Large Eddy Simulation for Incompressible Flows.* Springer, 1999.

[87] P. Moin, K. Squires, W. Cabot and S. Lee: *A dynamic subgrid-scale model for compressible turbulence and scalar transport.* Physics of Fluids A: Fluid Dynamics, 3:2746–2757, 1991.

[88] Patankar, S. V.: *Numerical Heat Transfer and Fluid Flow.* Hemisphere, Washington, 1980.

[89] Patankar, S. V. and Spalding, D. B.: *A calculation procedure for heat, mass and momentum transfer in three dimensional parabolic flows.* Int. J. Heat Mass Transfer, 15: 1787–1806, 1972.

[90] Paykani A., Kakaee A.-H., Rahnama P. and Reitz R. D.: *Progress and recent trends in reactivity-controlled compression ignition engines.* International J of Engine Research, 17(5):481–524, 2016.

[91] Peters, N.: *Laminar diffusion flamelet models in non-premixed turbulent combustion.* Progress in Energy and Combustion Science, 10(3):319 – 339, 1984.

[92] Peters, N.: *Laminar flamelet concepts in turbulent combustion.* Fwenty-first Symposium (International) on Combustion/The Combustion Institute, pages 1231–1250, 1986.

[93] Peters, N.: *Multiscale combustion and turbulence.* Proceedings of the Combustion Institute, 32(1):1 – 25, 2009.

[94] Pierce, Charles D. and Parviz Moin: *Progress-variable approach for large-eddy simulation of non-premixed turbulent combustion.* Journal of Fluid Mechanics, 504:73–97, 04 2004.

[95] Pino Martín, M., U. Piomelli and G.V. Candler: *Subgrid-Scale Models for Compressible Large-Eddy Simulations.* Theoretical and Computational Fluid Dynamics, 13(5):361–376, 2000.

[96] Pitsch, Heinz: *LARGE-EDDY SIMULATION OF TURBULENT COMBUSTION.* Annual Review of Fluid Mechanics, 38(1):453–482, 2006.

[97] Plengsaard, Chalearmpol and Christopher Rutland: *Improved Engine Wall Models for Large Eddy Simulation (LES).* In *SAE Technical Paper*. SAE International, 04 2013.

[98] Pope, S. B.: *Turbulent Flows.* Cambridge University Press, 5. edition, 2000.

[99] Pope, S. B. and U. Maas: *Simplified Chemical Kinetics: Trajectory-Generated Low-Dimensional Manifolds.* Cornell Report, (FDA 93-11):1–22, 1993.

[100] Pracht, W. E.: *Calculating Three-dimensional Fluid Flows at all speeds with an Eulerian-Lagrangian Computing Mesh.* Journal of Computational Physics, 17: 132–159, 1975.

[101] Prüfert, Uwe, Sandra Hartl, Franziska Hunger, Danny Messig, Michael Eiermann and Christian Hasse: *A constrained control approach for the automated choice of an optimal progress variable for chemistry tabulation.* Flow, Turbulence and Combustion, 94(3):593–617, 2015.

[102] Ramesh N. and Mallikarjuna J.M.: *Evaluation of in-cylinder mixture homogeneity in a diesel HCCI engine - A CFD analysis.* Engineering Science and Technology, an International Journal, 19:917–925, 2016.

[103] Reitz, Rolf D. and Ganesh Duraisamy: *Review of high efficiency and clean reactivity controlled compression ignition (RCCI) combustion in internal combustion engines.* Progress in Energy and Combustion Science, 46:12 – 71, 2015.

[104] Richardson, L. F.: *Weather Prediction by Numerical Process.* Cambridge University Press, Cambridge, 1922.

[105] S., Imtenan, Varman M., Masjuki HH., Kalam MA., Sajjad H. and Arbab MI. et al.: *Impact of low temperature combustion attaining strategies on diesel engine emissions for diesel and biodiesels: a review.* Energy Conversion and Management, 80:329–356, 2014.

[106] S., Saxena and Bedoya ID.: *Fundamental phenomena affecting low temperature combustion and HCCI engines, high load limits and strategies for extending these limits.* Progress in Energy and Combustion Science, 39:457–488, 2013.

[107] Schäfer, M.: *Computational Engineering - An Introduction to Numerical Methods.* Springer, Berlin, 2006.

[108] Smagorinsky, J.: *GENERAL CIRCULATION EXPERIMENTS WITH THE PRIMITIVE EQUATIONS.* Monthly Weather Review, 91(3):99–164, 1963.

[109] Song-Charng Kong, Rolf D. Reitz, Magnus Christensen and Bengt Johansson: *Modeling the effects of geometry-generated turbulence on HCCI engine combustion.* SAE Technical Paper 2003-01-1088, 2003.

[110] Spurk, J. H. and Aksel, N.: *Strömungslehre: Einführung in die Theorie der Strömungen.* Springer Verlag, Berlin, 6. edition, 2006.

[111] Stull, D. R. and H. Prophet: *JANAF Thermochemical Tables,2nd Edition.* National Bureau of Standards U.S.

[112] T., Hashizume, Miyamoto T., Hisashi A. and Tsujimura K.: *Combustion and emission characteristics of multiple stage diesel combustion.* SAE technical paper 980505, 1998.

[113] T, Yoshinaka and Keiichi N.: *Emission characteristics of premixed lean diesel combustion with extremely early staged fuel injection.* SAE technical paper, 961163, 1996.

[114] Tinham, Brian: *Next generation engines.* online.

[115] Tominaga R., Morimoto S., Kawabata Y. and Matsuo, S. et al: *Effects of Heterogeneous EGR on the Natural Gas Fueled HCCI Engine Using Experiments, CFD and Detailed Kinetics.* SAE Technical Paper 2004-01-0945, 2004.

[116] Torres, David J. and Mario F. Trujillo: *KIVA-4:An unstructured ALE code for compressible gas flow with sprays.* J. Comput. Phys., 219(2):943–975, 2006.

[117] Torres, David J., Li Y. and Kong S.-C.: *Partitioning Strategies for Parallel KIVA-4 Engine Simulations.* Computers and Fluids, 39:301–309, 2010.

[118] Torres D. J., O'Rourke P. J. and Amsden A. A.: *Efficient multicomponent fuel algorithm.* Combustion Theory and Modelling, 7(1):67–86, 2003.

[119] Truffin K. and Colin O.: *Auto-ignition model based on tabulated detailed kinetics and presumed temperature PDF-Application to internal combustion engine controlled by thermal stratifications.* International Journal of Heat and Mass Transfer, 54:4885–4894, 2011.

[120] U., Maas and J. Warnatz: *Ignition Processes in Hydrogen-Oxygen Mixtures.* Combustion and Flame, 74:53–69, 1988.

[121] W., Su, Wang H. and Liu B.: *Injection mode modulation for HCCI diesel combustion.* SAE technical paper 2005-01-0117, 2005.

[122] Wang Z. , Wang F. and Shuai S.-J.: *Study of Engine Knock in HCCI Combustion using Large Eddy Simulation and Complex Chemical Kinetics.* SAE Technical Paper 2014-01-2573, 2014.

[123] Warnatz, J.: *Chemistry of Stationary and Non-Stationary Combustion*, pages 162–188. Springer Berlin Heidelberg, Berlin, Heidelberg, 1981.

[124] Warnatz, J., U. Maas and Robert W. Dibble: *Combustion.* Springer, 2006.

[125] Xu H., Williams A., Fu H. and Wallace S. et al.: *Operating Characteristics of a Homogeneous Charge Compression Ignition Engine with Cam Profile Switching - Simulation Study.* SAE Technical Paper 2003-01-1859, 2003.

[126] Yao M., Zheng Z. and Liu H.: *Progress and recent trends in homogeneous charge compression ignition (HCCI) engines.* Progress in Energy and Combustion Science, 35:398–437, 2009.

[127] Yildar, Esra, Guido Kuenne, Chao He, Robert Schiessl, Marc Sebastian Benzinger, Neurohr Marius, Francesca di Mare, Amsinsi Sadiki and Johannes Janicka: *Understanding the influences of thermal and mixture inhomogeneities on the auto-ignition process in a Controlled Auto-Ignition (CAI) engine using LES.* Oil and Gas Science and Technology Rev. IFP Energies nouvelles, submitted, 2016.

[128] Yildar, Esra, Benzinger M.S., Guido Kuenne, He, Chao, di Mare, Francesca, Amsini Sadiki, Schiessl, Robert and Johannes Janicka: *Implementation of a multi-dimensional tabulated chemistry approach into an LES engine-code for simulation of CAI engines.* Combustion Science and Technology, submitted, 2016.

[129] Yu R., Bai X. S., Lehtiniemi H., Ahmed S. S., Mauss F., Richter M., Alden M., Hildingsson L., Johansson B. and Hultqvist A.: *Effect of Turbulence and Initial Temperature Inhomogeneity on Homogeneous Charge Compression Ignition Combustion.* SAE Technical Paper 2006-01-3318, 2006.

[130] Yu R., Bai X. S., Vressner A., Hultqvist A., Johansson B., Olofsson J., Seyfried H., Sjoholm J., Richter M. and Alden M.: *Effect of Turbulence on HCCI Combustion.* SAE Technical Paper 2007-01-0183, 2007.

[131] Yu R., Joelsson T., Bai X. S. and Johansson B.: *Effect of Temperature Stratification on the Auto-ignition of Lean Ethanol/Air Mixture in HCCI engine.* SAE Technical Paper 2008-01-1669, 2008.

[132] Zhao, F., T.W. Asmus, D.N. Assanis, J.E. Dec., J.A. Eng and P.M. Najt: *Homogeneous Charge Compression Ignition (HCCI) Engines.* Society of Automotive Engineers (SAE International, 2003.

[133] Zhen X. and Wang Y.: *Numerical analysis of knock during HCCI in a high compression ratio methanol engine based on LES with detailed chemical kinetics*. Energy Conversion and Management, 96:188–196, 2015.

Lebenslauf

Name	Esra Yildar	
Geburtsdatum	24. Oktober 1989	
Geburtsort	Ankara, Türkei	
Studium	06/2006 – 08/2008	**Technische Universität Ankara** Fachrichtung: Chemieingenieurwesen
	08/2008 – 03/2013	**Technische Universität Clausthal** Fachrichtung: Chemieingenieurwesen Abschluss zum Dipl.-Ing.
Beruflicher Werdegang	02/2013 - 02/2017	**Technische Universität Darmstadt** Wissenschaftliche Mitarbeiterin am Fachgebiet für Energie- und Kraftwerkstechnik (EKT)